

CHARACTERIZING THE QUARK GLUON PLASMA USING
SOFT THERMAL FLUCTUATIONS AND HARD PARTON
INTERACTIONS

MAYANK SINGH

Department of Physics
McGill University
Montreal, Quebec

2020

A thesis submitted to McGill University in partial fulfillment of the
requirements for the degree of Doctor of Philosophy

©Mayank Singh, 2020

ABSTRACT

Heavy ion collision experiments at the Large Hadron Collider (LHC) in Europe and at the Relativistic Heavy Ion Collider (RHIC) in the USA create deconfined Quark Gluon Plasma (QGP). QGP is a high density, high temperature, extreme state of strongly interacting matter. Properties of QGP are deduced by matching phenomenological calculations to experimental data. For an accurate extraction of QGP properties, all the relevant physical processes should be accounted for in a phenomenological model. We have investigated the effects of soft thermal fluctuations and hard parton interactions on experimental observables. We develop a new method to study soft thermal fluctuations using low pass noise filters. We also developed a framework to simultaneously evolve the jets and the QGP medium and introduced minijets in QGP simulations. The energy and momentum lost by minijets is introduced via hydrodynamic source terms in QGP. We also evaluated the size of viscous corrections on heavy quark transport coefficients. We observed that these physical processes affect the experimental observables, requiring a likely recalibration of QGP transport coefficients.

RÉSUMÉ

Les collisions d'ions lourds effectuées au Grand Collisionneur de Hadrons (LHC) en Europe et au Collisionneur d'Ions Lourds Relativistes (RHIC) aux USA ont pu créer un plasma de quarks et de gluons (QGP). Le QGP est une phase exotique de la matière en interaction forte, où la densité et la température adoptent des valeurs extrêmes. Les propriétés du plasma sont déduites à la suite de comparaisons entre théorie et mesures expérimentales. Les modèles phénoménologiques utilisés pour cette comparaison doivent donc être les plus complets possible. Nous avons étudié les effets de fluctuations thermodynamiques et des interactions de partons énergétiques sur les variables expérimentales. Nous avons développé une nouvelle approche pour étudier les fluctuations en appliquant des filtres passe-bas. Nous avons également mis au point une approche qui traite simultanément les jets énergétiques, les jets de plus basses énergies (« minijets ») et le milieu hydrodynamique. L'énergie et l'impulsion perdues par ces minijets apparaissent dans des termes qui agissent comme une source pour le milieu hydrodynamique, Nous quantifions l'effet des corrections visqueuses sur les propriétés de transport des quarks lourds. L'inclusion de tous ces effets nécessitera une réévaluation des termes de viscosité de volume et de cisaillement déduits des analyses faites jusqu'à maintenant.

ACKNOWLEDGEMENTS

First and foremost, I am deeply indebted to my supervisor Charles Gale for all his help and support through the years. His guidance, encouragement and incredible patience helped me navigate the ups and downs of life in academia.

I would also like to thank Sangyong Jeon, who was always available for help and guidance. He has effectively been my second mentor who also provided computation resources which was crucial for completion of this thesis.

I am grateful to Chun Shen who has helped me through countless discussions, quick email replies and gracefully hosting me on multiple occasions when in person help was necessary.

This work has benefited greatly from discussions with and advice from Sigtryggur Hauksson, Manu Kurian, Scott McDonald, Daniel Pablos, Chanwook Park, Bjoern Schenke, Shuzhe Shi, Misha Stephanov, Derek Teaney, Li Yan and Clint Young. My heartfelt thanks to all of them.

I greatly appreciate help from Matthew Heffernan who went through parts of this thesis and provided helpful feedback.

I acknowledge Fonds de recherche du Québec – Nature et technologies (FRQNT) for providing funding through the Bourses d'excellence pour étudiants étrangers (PBEEE) for part of this work. I am also thankful to the Beam Energy Scan Theory (BEST) collaboration for funding my travel multiple times, allowing me to and benefit from interactions with some of the leading experts in the field.

This work would not be completed without computation resources provided by Compute Canada and Calcul Québec.

I owe a debt of gratitude to all the members of nuclear theory group during my time here at McGill for teaching me a great deal and making my time here fun.

Last but not the least, my heartfelt thanks to my friends and family, specially my mother and my brother for their love and support.

STATEMENT OF ORIGINALITY

The original contribution by the author to this work is as follows

- **Chapters 1 - 3:** These chapters give a general introduction to QCD matter in extreme conditions and heavy ion collisions.
- **Chapter 4:** This is the outline of the remainder of thesis.
- **Chapter 5:** This chapter is a general introduction to thermal fluctuations and a comprehensive literature review of thermal fluctuation studies in the context of heavy ion collisions.
- **Chapter 6:** I build on the work done in [1] to do my own calculations. Perturbative fluctuation framework was developed and the initial code for the same was written by Clint Young. The evaluation of eccentricities and hadronic and photonic observables was done by me. This included evaluating fluctuation corrections to photon rates.
- **Chapter 7:** I developed the low pass filter method to study thermal fluctuations, coded it in the hydrodynamic package MUSIC, tested the effects of noise cutoff parameter on fluctuation modes in static fluid and Bjorken flow and evaluated the experimental observables.
- **Chapter 8:** I used the low pass filter method developed in last chapter to study bulk fluctuations. I encoded bulk fluctuations in MUSIC and evaluated experimental observables. The work on effects of negative kinematic pressure was done in collaboration with Scott McDonald. I did the literature review and ran half the hydrodynamic simulations for this work.
- **Chapter 9:** This work was done in collaboration with Daniel Pablos. The Mach cone analysis was done by me. I encoded an artificial jet energy source in MUSIC

and calculated the energy enhancement at the freezeout surface. Daniel encoded the hybrid model in MUSIC and did the energy conservation testing. The second pass framework was developed by me. I also developed the workflow to introduce PYTHIA hadrons in UrQMD. I did the standardization of the concurrent framework.

- **Chapter 10:** This work was done in collaboration with Manu Kurian. Manu did the analytical calculations to get the expressions for viscous corrections to charm transport coefficients. I did the numerical integration of these expressions. I performed the entire hydrodynamic simulation and wrote a wrapper code to simulate propagation of charm quark through QGP.

CONTENTS

Abstract	iii
Résumé	iv
Acknowledgements	v
Statement of Originality	vi
List of Figures	xi
I QCD MATTER IN HEAVY-ION COLLISIONS	1
1 QUANTUM CHROMODYNAMICS AND HEAVY-ION COLLISIONS	3
1.1 QCD Lagrangian	4
1.2 Lattice QCD	6
1.3 Phase diagram of QCD	7
1.4 Heavy-ion collision experiments	8
2 PHENOMENOLOGY OF HEAVY-ION COLLISIONS	11
2.1 Modelling collective dynamics	11
2.2 Modelling jet physics	23
2.3 Modelling heavy-flavor dynamics	25
2.4 Modelling photon emission	27
2.5 Summary	28
3 OBSERVABLES IN HIC EXPERIMENTS	30
3.1 Rapidity and pseudorapidity	30
3.2 Multiplicity and centrality	30
3.3 Soft hadronic observables	32
3.4 Jet observables	37
3.5 Heavy quarks in QGP	39
3.6 Electromagnetic observables	40
3.7 Summary	40
4 OUTLINE OF THE REST OF THIS THESIS	41

II	THERMAL HYDRODYNAMIC FLUCTUATIONS	43
5	HYDRODYNAMIC FLUCTUATIONS IN HIC	44
5.1	Linear response theory	44
5.2	Fluctuation-dissipation theorem	46
5.3	Deterministic treatment of thermal fluctuations	48
5.4	Stochastic treatment of thermal fluctuations	51
5.5	Challenges in stochastic treatment of fluctuations	53
5.6	Summary	56
6	FLUCTUATIONS AS PERTURBATION	57
6.1	Perturbative stochastic hydrodynamics	57
6.2	Hydrodynamic simulations	58
6.3	Momentum eccentricities	60
6.4	Hadronic observables	61
6.5	Photonic observables	63
6.6	Summary	65
7	NON-PERTURBATIVE TREATMENT OF NOISE	67
7.1	Noise filter	67
7.2	Tests in simple systems	70
7.3	Model details	77
7.4	Mid-rapidity observables	77
7.5	Summary	86
8	BULK VISCOSITY AND FLUCTUATIONS	87
8.1	Bulk viscosity profile and noise filter for bulk viscous fluctuations	87
8.2	Effects of bulk viscous fluctuations	90
8.3	Negative kinematic pressure	95
8.4	Summary	101
III	HARD PARTONS IN QGP	102
9	JET MEDIUM RESPONSE	103
9.1	Mach Cones in QGP	104
9.2	Energy enhancement at the freezeout surface	109
9.3	Testing energy conservation	110

9.4	Second pass framework	111
9.5	Standardizing concurrent framework	113
9.6	Summary	115
10	CHARM QUARKS IN QGP	117
10.1	Charm transport coefficients	117
10.2	Shear viscous correction	119
10.3	Bulk viscous corrections	121
10.4	Results	122
10.5	Summary	127
	IV CONCLUSION	129
	BIBLIOGRAPHY	133

LIST OF FIGURES

Figure 1.1	Running of the strong coupling α_s as a function of energy transfer Q . Figure is taken from [13].	5
Figure 1.2	Equation of state from lattice QCD. Pressure (p), energy density (ϵ) and entropy density (s) are shown as a function of temperature. The yellow shaded area is the crossover region. Dark lines denote calculations from a hadron resonance gas model and the lighter broad lines show the result from the lattice QCD calculations. Figure taken from the hotQCD collaboration [15].	6
Figure 1.3	A schematic diagram showing phases of QCD matter. It also illustrates different regions accessed by different experiments. Figure taken from [21]. Note that modern estimates based on lattice QCD place the crossover temperature closer to 155 MeV [22].	8
Figure 2.1	Flowchart of our modelling of HICs. Parts indicated in red are new contributions to the model made in this work.	12
Figure 2.2	$2 \rightarrow 2$ scattering diagrams for HQ interaction with the medium. In the first three diagrams, the quarks are HQ.	27
Figure 3.1	Illustration of the centrality of a collision event. Red and green circles denote projectile and target nuclei respectively. The overlap area in collisions reduces as one goes from central to peripheral collisions.	31
Figure 3.2	Centrality binning for Pb-Pb collisions at $\sqrt{s} = 2.76$ TeV. VZERO amplitude is a proxy for multiplicity in an event. Figure taken from the ALICE collaboration [91].	32

Figure 3.3	Charged particle multiplicities for different centrality bins as a function of pseudorapidity (left) and transverse momentum (right) for Pb-Pb collisions at $\sqrt{s} = 2.76$ TeV. Figures taken from the ALICE collaboration [92, 93].	33
Figure 3.4	Polar plots of $1 + 2v_n \cos(n\phi)$ for small v_n (in blue). They denote elliptic (left), triangular (centre) and quadrangular (right) flow for $n = 2, 3$ and 4 respectively. Black circles show isotropic flow and are drawn for reference.	34
Figure 3.5	Illustration showing the conversion of pressure gradients to momentum anisotropy. Because of collective behaviour, there is larger pressure gradient in x direction than in y direction. This contributes to positive v_2 . v_3 is generated from the fluctuations in nucleon position within the nuclei (and sub-nucleonic fluctuations not shown here). Figure taken from [98].	35
Figure 3.6	Illustration of EP correlators. When the event planes of v_2 and v_3 are perfectly aligned, then $3 \cdot 2 \cdot \Psi_2 - 2 \cdot 3 \cdot \Psi_3 = 0$ and $\cos[6(\Psi_2 - \Psi_3)] = 1$ (left). When they are not perfectly aligned, then the EPs are decorrelated and $\cos[6(\Psi_2 - \Psi_3)] < 1$ (right).	36
Figure 3.7	Nuclear modification factor for inclusive jets with cone size $R = 0.4$ (left) and charged hadrons (right). Data is from the ATLAS and CMS collaborations for $\sqrt{s} = 5.02$ TeV Pb-Pb collisions in the 0 – 10% centrality bin and it is compared to model calculations from the JETSCAPE collaboration. Figure reproduced from [106].	38
Figure 5.1	Illustration of the fluctuation-dissipation theorem for a closed system of gas molecules.	47
Figure 5.2	Typical energy density profiles for hydrodynamic evolution without (left) and with (right) thermal fluctuations.	54
Figure 6.1	Evolution of momentum eccentricity as a function of proper time with and without thermal noise. This is averaged over 600 noisy events for Au-Au collision system at $\sqrt{s} = 200$ GeV with impact parameter 3 fm.	61

Figure 6.2	Differential v_n for zero impact Au-Au collisions at $\sqrt{s} = 200$ GeV. Bands denote statistical error bars.	62
Figure 6.3	Hadronic event plane correlators defined in section 3.3.2 for Au-Au collisions at $\sqrt{s} = 200$ GeV. Bands denote statistical uncertainties.	63
Figure 6.4	Thermal photon v_2 for fluctuating and non-fluctuating events with impact parameters 3 fm (left) and 7 fm (right). Bands denote statistical error bars.	64
Figure 6.5	Distribution of photon v_2 event planes at $p_T = 1.413$ GeV for fluctuating events with impact parameter 3 fm.	65
Figure 7.1	Sampled noise component $\zeta^{1,1}$ at midrapidity. Left: before removing high wavenumber modes. Right: after removing modes larger than $p_{cut} = 0.6/\tau_\pi$	69
Figure 7.2	Snapshots of temperature fluctuations in a 2D slice of static fluid at a fixed time for different values of x	71
Figure 7.3	Ratio of two point correlators of noise terms with their equilibrium values for a static fluid with different x values. The dashed line is at $N/N_0 = 1$	73
Figure 7.4	Temperature and shear relaxation time evolution with proper time in a fluid expanding with Bjorken solution.	74
Figure 7.5	Ratio of two point correlators of noise terms in x-direction with their equilibrium values for fluid undergoing Bjorken expansion with different x values. The dashed line is at $N/N_0 = 1$	75
Figure 7.6	Ratio of two point correlators of noise terms in rapidity-direction with their equilibrium values for a static fluid with different x values.	76
Figure 7.7	Charged hadron multiplicity for Pb-Pb collisions at $\sqrt{s} = 2.76$ TeV with and without thermal fluctuations. Data points are taken from the ALICE collaboration [91].	78
Figure 7.8	Identified particles' mean transverse momentum for Pb-Pb collisions at $\sqrt{s} = 2.76$ TeV with and without thermal fluctuations. Data points are taken from the ALICE collaboration [161].	78

Figure 7.9	Charged hadron integrated v_n for Pb-Pb collisions at $\sqrt{s} = 2.76$ TeV with and without thermal fluctuations. Data points are taken from the ALICE collaboration [162].	79
Figure 7.10	p_{cut} dependence of charged hadron integrated v_n for 0-5% centrality Pb-Pb collisions at $\sqrt{s} = 2.76$ TeV with thermal fluctuations. . .	79
Figure 7.11	p_{cut} dependence of charged hadron differential v_n for 0-5% centrality Pb-Pb collisions at $\sqrt{s} = 2.76$ TeV with thermal fluctuations.	81
Figure 7.12	Charged hadron differential v_n for 0 – 5% centrality Pb-Pb collisions at $\sqrt{s} = 2.76$ TeV with and without thermal fluctuations. Data points are taken from the ALICE collaboration [162].	82
Figure 7.13	Charged hadron differential v_n for 30 – 40% centrality Pb-Pb collisions at $\sqrt{s} = 2.76$ TeV with and without thermal fluctuations. Data points are taken from the ALICE collaboration [162].	82
Figure 7.14	Charged hadron event-plane correlators for Pb-Pb collisions at $\sqrt{s} = 2.76$ TeV with and without thermal fluctuations. Data points are taken from the ATLAS collaboration [163]. Centrality to N_{part} conversion was based on MC-Glauber model based table in [163]. .	83
Figure 7.15	Linear part of charged hadron v_n for Pb-Pb collisions at $\sqrt{s} = 2.76$ TeV with and without thermal fluctuations. Data taken from the ALICE collaboration [164].	84
Figure 7.16	Non-linear response coefficients of charged hadron v_n for Pb-Pb collisions at $\sqrt{s} = 2.76$ TeV with and without thermal fluctuations. Data taken from the ALICE collaboration [164].	85
Figure 7.17	p_{cut} dependence of selected linear contributions and non-linear response coefficients of charged hadron v_n for Pb-Pb collisions at $\sqrt{s} = 2.76$ TeV.	85
Figure 8.1	Bulk viscosity over entropy density profile given in eq. (8.1).	88
Figure 8.2	Shear and bulk relaxation times and the coefficients in the fluctuation-dissipation theorem for the fluctuations for our simulations.	89

Figure 8.3	This represents one 40-50% centrality Pb-Pb collision event at $\sqrt{s} = 2.76$ TeV without thermal fluctuations. (a) shows the probability density of a fluid cells to have a certain Π/P_0 value throughout the lifetime of the fluid state, while (c) shows the probability density of fluid cells to have a certain temperature. (b) is the scatter plot of fluid cells on the temperature- Π/P_0 axis where each point denotes one spatio-temporal fluid cell.	90
Figure 8.4	Same as fig. 8.3 but with shear and bulk hydrodynamic fluctuations.	91
Figure 8.5	Charged hadron multiplicity for Pb-Pb collisions at $\sqrt{s} = 2.76$ TeV with bulk fluctuations. Data points are taken from the ALICE collaboration [91].	92
Figure 8.6	Identified particles' mean transverse momentum for Pb-Pb collisions at $\sqrt{s} = 2.76$ TeV with bulk fluctuations. Data points are taken from the ALICE collaboration [161].	93
Figure 8.7	Charged hadron integrated v_n for Pb-Pb collisions at $\sqrt{s} = 2.76$ TeV with bulk fluctuations. Data points are taken from the ALICE collaboration [162].	94
Figure 8.8	Charged hadron event-plane correlators for Pb-Pb collisions at $\sqrt{s} = 2.76$ TeV with bulk fluctuations. Data points are taken from the ATLAS collaboration [163] Centrality to N_{part} conversion was based on MC-Glauber model based table in [163].	94
Figure 8.9	Plots showing temperature(top), Π/P_0 (middle) and expansion rate θ (bottom) at different proper times (τ) at midrapidity for a 40-50% centrality Pb-Pb collision at $\sqrt{2.76}$ TeV.	97
Figure 8.10	Same as fig. 8.9 except ζ/s is 10 times the value reported in eq. (8.1).	98
Figure 8.11	Same as fig. 8.3 but with condition $ \Pi < P_0$ imposed.	99
Figure 8.12	Identified particles' mean transverse momentum for Pb-Pb collisions at $\sqrt{s} = 2.76$ TeV with constrained Π . Data points are taken from the ALICE collaboration [161].	100

Figure 9.1	Top panel shows the energy density profile with white arrows showing the direction of jet-propagation. Bottom three panels show difference in energy density with and without jets 3 fm/c after the beginning of hydrodynamic evolution for different values of η/s . Black lines indicate the expected wavefront in a static fluid.	105
Figure 9.2	Same as fig. 9.1 but 6 fm/c after the beginning of hydrodynamic evolution	106
Figure 9.3	Same as fig. 9.1 but 9 fm/c after the beginning of hydrodynamic evolution	107
Figure 9.4	Difference in energy flux through the freezeout surface of events with and without jets. Inset denotes the orientation of the jet with respect to the underlying fireball.	109
Figure 9.5	Same as fig. 9.4 for a different jet orientation.	110
Figure 9.6	Energy density (left panels) and difference in energy density because of jets (right panels) in a Pb-Pb collision at $\sqrt{s} = 2.76$ TeV. Jet energy loss is modelled by the hybrid model [76]. White dots denote the location of energy deposition.	112
Figure 9.7	Charged hadron multiplicity for Pb-Pb collisions at $\sqrt{s} = 2.76$ TeV with different value of p_{min} . Data points are taken from the ALICE collaboration [91]. Both the parameter sets have different energy normalizations.	114
Figure 9.8	Charged hadron integrated v_n for Pb-Pb collisions at $\sqrt{s} = 2.76$ TeV with different value of p_{min} . Data points are taken from the ALICE collaboration [162].	115
Figure 10.1	Temperature evolution along $y = 0$ axis at mid-rapidity. White arrows indicate local flow.	123
Figure 10.2	Drag coefficients of a charm with $p = (\sqrt{m_c^2 + p^2}, p, 0, 0)$ in lab frame at each space-time point. Curves indicate constant value contours.	124

- Figure 10.3 Diffusion coefficients B_0 (left) and $B_1 - B_0$ (right) of a charm with $p = (\sqrt{m_c^2 + p^2}, p, 0, 0)$ in lab frame at each space-time point. Curves indicate constant value contours. 124
- Figure 10.4 Ratio of shear (left) and bulk (right) viscous corrections to the equilibrium values for A (top), B_0 (middle) and $(B_1 - B_0)$ (bottom). Charm properties are same as in figs. 10.2 and 10.3. 125
- Figure 10.5 Spatial diffusion coefficient calculated in present work compared with estimations from LO pQCD [198], lattice QCD [199] and quasi-particle model (QPM) [200]. 126
- Figure 10.6 Trajectory of charm quarks with different initial momentum (left). Momentum lost by charm as a function of temperature along the trajectory (middle). Percentage momentum lost as a function of proper time (right). Numbers denote the initial momentum in the x -direction. Momentum in y and longitudinal directions is zero. . . 127
- Figure 10.7 Momentum loss in a quark starting 128

Part I

QCD MATTER IN HEAVY-ION COLLISIONS

In this thesis, our aim is to improve upon our understanding of the quark-gluon plasma by studying physical processes that have mostly been overlooked in phenomenological calculations to date. We begin by introducing the basics of quantum chromodynamics and the role that heavy ion collision experiments play in studying it in chapter 1. A description of phenomenological tools used to study heavy-ion collisions is given in chapter 2. Observables measured in these experiments and the physical insights drawn from them are explained in chapter 3.

Thermal hydrodynamic fluctuations are studied in part II, hard partonic interactions are studied in part III and our results are summarized in part IV. A detailed outline of these parts is given in chapter 4.

QUANTUM CHROMODYNAMICS AND HEAVY-ION COLLISIONS

By the 1960s, physics had reached the sub-nucleon scale. The quark model of hadrons was proposed to explain the large number of then-recently discovered particles [2, 3]. The quark model hypothesized that many of these new particles, called hadrons, were not fundamental themselves, but rather formed by pairs or triplets of postulated spin-1/2 fundamental particles called quarks.

The quark model ran afoul of the Pauli exclusion principle. If the proposed quarks were indeed spin-1/2, they should obey Fermi statistics. That meant that two quarks could not have existed in an identical quantum state inside a composite particle. But this was not the case. For example, in Δ^{++} baryon, three identical quarks were understood to have their spins aligned and have a vanishing net orbital angular momentum. In violation of Pauli's exclusion principle, the net wavefunction was symmetric under the exchange of any two quarks. A novel color charge was proposed to reconcile this violation [4]. This color charge created a new quantum number under which the wavefunctions of individual quarks could be anti-symmetric. This color charge was a consequence of a newly postulated $SU(3)$ gauge degree of freedom [5].

Deep inelastic scattering experiments performed at the Stanford Linear Accelerator Center (SLAC) [6] suggested that the constituent particles of protons, i.e. quarks, are point sized. On one hand, these quarks behaved almost like free particles at high momentum transfers (or equivalently at short length scales) while on the other hand, these quarks seemed always confined in hadrons. As a result, the interaction between quarks had to be mediated by a force that is strong at long distances but weak at very short distances. This behaviour is now famously known as asymptotic freedom. Gross and Wilczek [7] and Politzer [8] demonstrated that a unique class of quantum field theories

called non-abelian gauge theories had this property. These theories had interactions mediated by vector bosons. These theories based on the generalized non-abelian $SU(N)$ gauge symmetry were previously discovered by Yang and Mills [9]. This led to the development of the theory of strong forces, quantum chromodynamics (QCD).

1.1 QCD LAGRANGIAN

QCD is a $SU(3)$ gauge symmetric, fundamental theory of strong interactions. Quarks are in the fundamental representation of this gauge group. Interactions are mediated by vector gauge bosons called gluons, which are in the adjoint representation of $SU(3)$. Quarks and gluons are together referred to as partons. The QCD Lagrangian is given as¹

$$\mathcal{L} = \bar{\psi}_i(i(\gamma^\mu D_\mu)_{ij} - m\delta_{ij})\psi_j - \frac{1}{4}F_a^{\mu\nu}F_{\mu\nu}^a. \quad (1.1)$$

The $SU(3)$ gauge group is indexed as i, j that run from 1 to 3. ψ_i is a quark field, γ^μ are Dirac matrices and $D_\mu = \partial_\mu - igA_\mu^a$ is a gauge covariant derivative. $F_{\mu\nu}^a$ are field strength tensors with the color index a running from 1 to 8. The field strength tensor is given as

$$F_{\mu\nu}^a = \partial_\mu A_\nu^a - \partial_\nu A_\mu^a + gf^{abc}A_\mu^b A_\nu^c. \quad (1.2)$$

A_μ^a are gluon fields, f^{abc} are the structure constants of the $SU(3)$ group, m denotes quark masses and g is the coupling strength.

As mentioned above, QCD delivers on the requirement of asymptotic freedom and confinement. This comes from the dependence of coupling strength g on the energy scale, called the running of coupling. This could be understood in terms of renormalization.

Renormalizing the coupling strength in QCD demonstrates how interaction strength varies with energy. Let us look at the Callan-Symanzik beta-function [10, 11]

$$\beta(g) = \frac{\partial}{\partial \log(Q/M)}g. \quad (1.3)$$

Here, Q is the energy scale and M is some specific scale at which the coupling $g(M)$ is known. The β -function can be calculated from the loop-diagrams of QCD. For QCD with

¹ Einstein notation of summing over repeated indices is used in this thesis. We use the mostly negative metric (see section 2.1.2) and $\hbar = c = 1$ is assumed in the rest of this thesis.

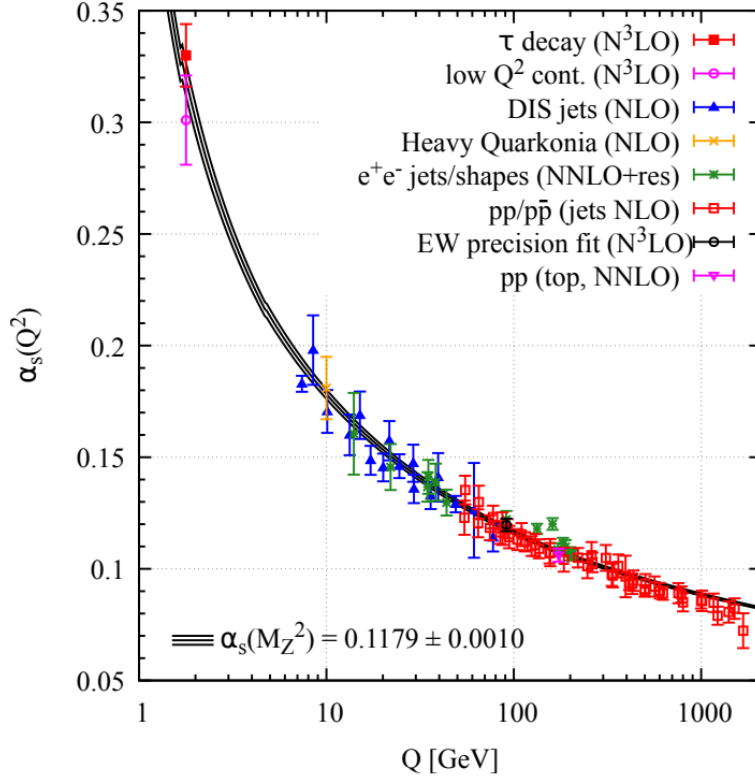


Figure 1.1: Running of the strong coupling α_s as a function of energy transfer Q . Figure is taken from [13].

three colors and n_f flavors of almost massless quarks, up to leading order we have [7, 8] (for details, see [12])

$$\beta(g) = -\frac{b_0 g^3}{(4\pi)^2}, \quad (1.4)$$

with

$$b_0 = 11 - \frac{2}{3}n_f. \quad (1.5)$$

Solving eq. (1.3) for coupling strength $\alpha_s = g/4\pi$, we get

$$\alpha_s(Q^2) = \frac{4\pi}{b_0 \log(Q^2/\Lambda_{QCD}^2)}. \quad (1.6)$$

Λ_{QCD} is the scale at which the QCD coupling diverges, $\Lambda_{QCD} \approx 300$ MeV [14]. Eq. (1.6) shows that the coupling strength α_s decreases as energy scale Q increases and reaches zero asymptotically. Also, α_s diverges at Λ_{QCD} and as a result, one cannot separate a quark-antiquark pair farther than $1/\Lambda_{QCD}$ thus achieving confinement. The running value of α_s is shown in fig. 1.1.

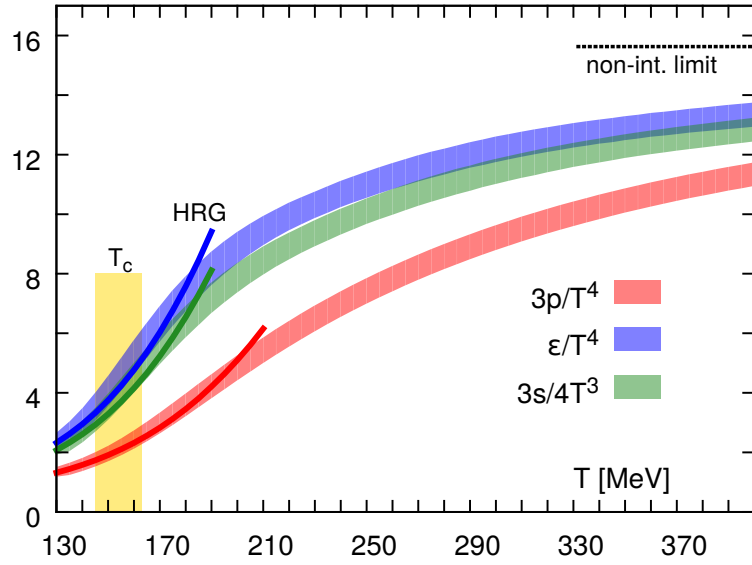


Figure 1.2: Equation of state from lattice QCD. Pressure (p), energy density (ϵ) and entropy density (s) are shown as a function of temperature. The yellow shaded area is the crossover region. Dark lines denote calculations from a hadron resonance gas model and the lighter broad lines show the result from the lattice QCD calculations. Figure taken from the hotQCD collaboration [15].

1.2 LATTICE QCD

Field theories are typically studied by expanding the action, using the coupling constant as a small parameter. This is the technique of using Feynman diagrams [16]. Perturbative QCD is such an application of this method. Interaction cross-sections between various particles can be calculated this way, but only when α_s is much smaller than one. This is true only for very high energies.

Another approach, first developed by Wilson [17], is known as lattice QCD. Partition function of QCD can be evaluated in the Feynman path integral formalism [18] numerically, using Monte-Carlo integration techniques on a lattice. This is a head-on approach to obtain expectation values of various observables by numerical integration, but this method only works for a system at equilibrium. In other words, a dynamically evolving system of QCD matter cannot be described by lattice QCD. Also, lattice QCD is currently restricted to situations with vanishing baryon chemical potential (μ_B). At finite μ_B , the integrands are complex [19] and hence highly oscillating. There is no known method to

constrain the highly oscillating integrand. This is known as the sign-problem. As highly oscillating integrands are almost impossible to integrate numerically, it is very difficult to extend lattice QCD to non-zero μ_B .

Despite these caveats, lattice QCD provides immense insight into the world of QCD matter. Crucially, it is a direct first principles calculation. Lattice QCD suggests that the quarks and gluons are confined in hadrons at low energies, a consequence of strong coupling. At high energies, they are liberated from hadrons forming a hot plasma of color-charged particles: the quark-gluon plasma (QGP). This is a direct consequence of the running coupling.

Lattice QCD also shows that this transition from a gas of hadrons to QGP is a smooth crossover and not a sudden phase-transition [20]. Fig. 1.2 shows the equation of state from lattice QCD. At low temperatures, the lattice QCD results are in good agreement with the hadron resonance gas (HRG) model calculations. This suggests that quarks and gluons are confined in hadrons in this region. The two calculations start diverging around the crossover temperature T_c . This is a result of a rapid increase in the degrees of freedom. In this region, the QCD matter enters the QGP phase. This transformation, though rapid, is smooth: there is no discontinuity in any thermodynamic quantities or their derivatives.

1.3 PHASE DIAGRAM OF QCD

Even though the sign-problem effectively restricts direct application of lattice QCD to zero baryon chemical potential, we have some idea as to how the entire phase diagram of QCD looks like.

Fig. 1.3 shows the conjectured QCD phase diagram. Normal nuclear matter (nucleons) sits at high μ_B and very small temperature. At very high densities and low temperatures, up and down quarks are expected to form Cooper pairs and form a color superconductor [23–25]. On the other extreme, the early universe is known to be very hot and have very small μ_B .

Model calculations suggest that at high baryon densities, the hadron gas changes to QGP via a first-order phase transition [26]. As we already know that the change is a

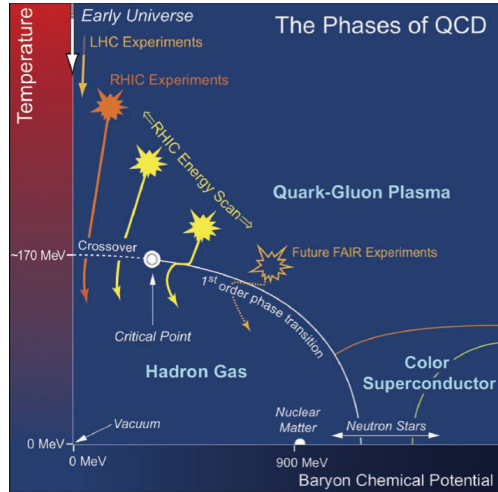


Figure 1.3: A schematic diagram showing phases of QCD matter. It also illustrates different regions accessed by different experiments. Figure taken from [21]. Note that modern estimates based on lattice QCD place the crossover temperature closer to 155 MeV [22].

smooth crossover at zero μ_B [20], this implies that the first-order phase transition line ends in a critical point where the transition is second-order.

Different regions of the diagram can be accessed by different experimental approaches. Neutron star observations through multi-messenger astronomy can help us understand the large μ_B region of the diagram. Neutron stars can be observed using the various bands of electromagnetic signals, neutrinos and gravitational waves. These observations help us constrain the equation of state of neutron stars. For a recent review, see [27]. Low and intermediate μ_B regions are accessible through the heavy-ion collision experiments.

While various regions of the phase diagram are schematically known, the exact location of the different features such as the critical point and the phase transition line have not been quantified. Quantitatively locating and understanding the dynamics of the critical point is one of the goals of many recent heavy-ion collision (HIC) experiments.

1.4 HEAVY-ION COLLISION EXPERIMENTS

Heavy-ion collision experiments have been performed at the Large Hadron Collider (LHC) in Europe and at the Relativistic Heavy-Ion Collider (RHIC) in the USA. LHC and

high-energy RHIC experiments collide heavy nuclei at very high energy at relativistic speeds to achieve the high temperatures required for QGP formation. The QGP droplet created is small (a few fm in length) and short lived (of the order of 5-20 fm/c) [28, 29].

A lot happens during the short lifetime of QGP droplets. The droplet keeps expanding and cools rapidly. There are some very energetic or massive partons created by initial hard scattering that traverse through the droplet. As they have very high energies, they effectively interact perturbatively. All these partons, heavy or light, with high or low energies, recombine to form hadrons when the temperature drops below T_c . Both QGP and hadron gas also emit photons and lepton pairs. These varied processes create a wide range of experimental observables that need a gamut of theoretical tools for deducing the physics.

QGP properties are deduced from the measurements of hadronic and electromagnetic particles. Unfortunately, we do not yet have a mechanism with which to study dynamical QGP out of equilibrium from first principles. We use phenomenological models to understand these experiments and draw physical inference. A standard model of heavy-ion collisions is described in chapter 2. Experimental observables that are measured in these experiments are described in chapter 3.

These experiments collide heavy nuclei at such high energies (e.g. Pb-Pb collisions at LHC at centre of mass energies 2.76 TeV and 5.02 TeV and Au-Au collisions at RHIC at centre of mass energy 200 GeV) that the amount of baryons and anti-baryons created is almost equal. This means that the matter created is close to the $\mu_B = 0$ axis in the phase diagram and input from lattice QCD can be used to model these experiments. Recently, RHIC has started a beam energy scan program that collides nuclei at lower energies. The goal is to access the intermediate μ_B range and hopefully probe the critical point. Future experiments planned at the Facility for Anti-proton and Ion Research (FAIR) in Germany and at Nuclotron based Ion Collider Facility (NICA) in Russia plan to explore the even higher μ_B region by conducting even lower energy collisions. The regions explored by these experimental programs can be seen in the schematic in fig. 1.3.

In this work, we have restricted ourselves to very high energy collisions at vanishing chemical potential. This is because the QGP equation of state is better constrained in

this region by lattice QCD. The tools developed in this work to understand QGP can be applied to lower energy collision systems with an appropriate equation of state.

PHENOMENOLOGY OF HEAVY-ION COLLISIONS

At present, there is no *ab initio* approach to study dynamical evolution of QGP. As a result, we must rely on composite models of heavy-ion collisions to study the physics of QCD matter. In this chapter, we describe the standard model of heavy-ion collisions that has been very successful in explaining features of HIC experiments.

Fig. 2.1 is a flowchart of the hybrid model used in this work. Parts of the flowchart shown in red are original contributions to the field contained in this thesis. We describe the different components of this flowchart in this chapter. We begin by describing the collective dynamics of QGP itself followed by the dynamics of hard light quarks, heavy quarks and photons.

2.1 MODELLING COLLECTIVE DYNAMICS

Nuclei colliding at HIC experiments travel near the speed of light. In the lab frame, they appear as flat 2D surfaces due to Lorentz contraction in the beam direction. Immediately after collision, the QCD matter created rapidly hydrodynamizes at times < 1 fm/c. By hydrodynamization, we mean that the system reaches a state in which hydrodynamics is applicable. This value was obtained from fitting hydrodynamic start time in models to data [30–33]. This was traditionally understood to require the system to be close to local thermal equilibrium, though recently this has come under revision. There is evidence to believe that hydrodynamics applies even if the system is far from local thermal equilibrium [34]. Systems far from equilibrium have hydrodynamic and non-hydrodynamic modes. Non-hydrodynamic modes have been shown to decay rapidly in a wide range of theories and the system approaches the hydrodynamic attractor solutions [35, 36]. The

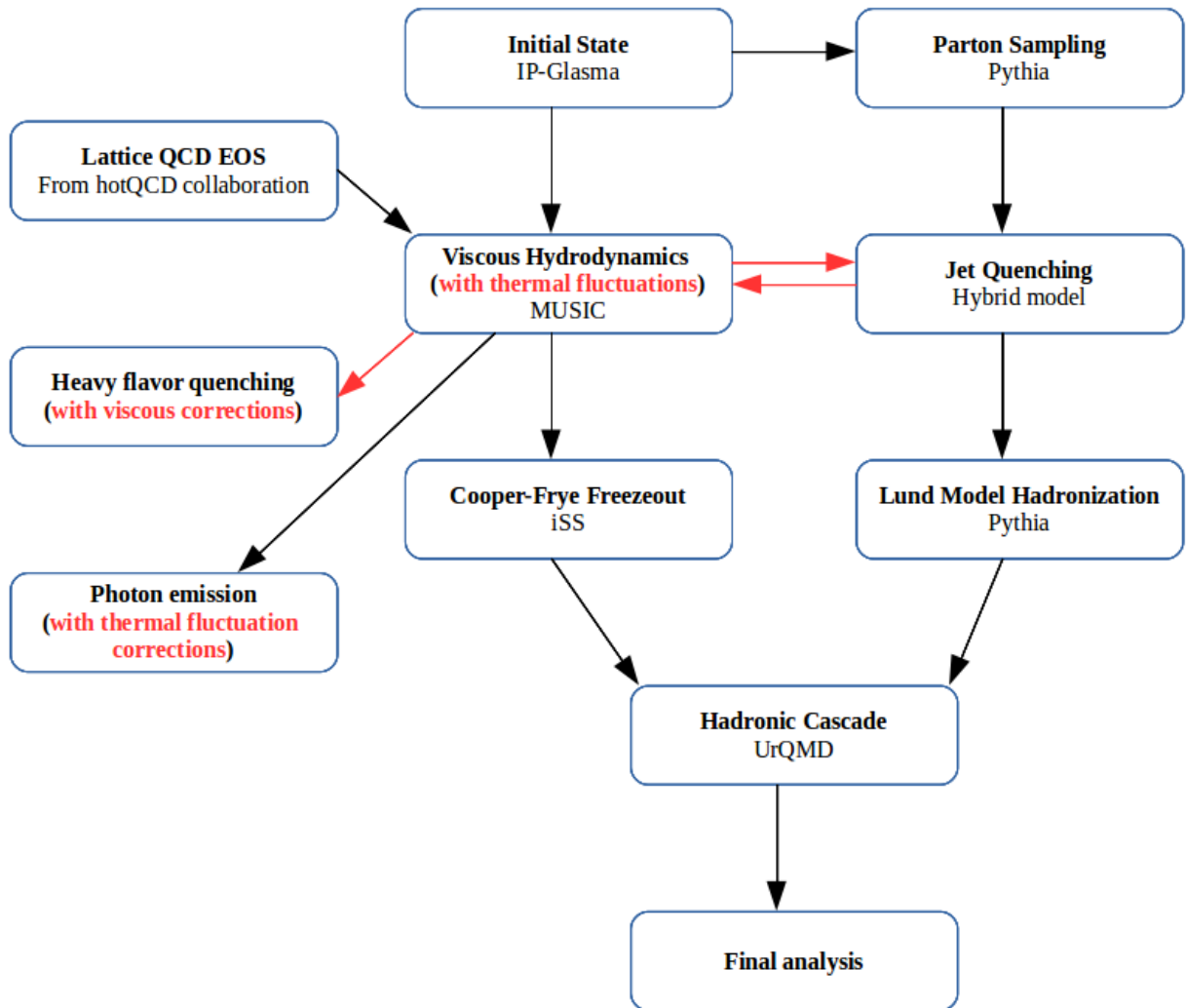


Figure 2.1: Flowchart of our modelling of HICs. Parts indicated in red are new contributions to the model made in this work.

system then expands hydrodynamically for about 5 – 20 fm/c. At this point, the density and temperature of the fluid falls below the deconfinement temperature and QGP fluid transforms to a gas of hadrons. This hadron gas keeps expanding and the hadrons keep interacting with each other and resonances keep decaying. This stage is the hadronic cascade. Eventually the system reaches kinetic freezeout and particles free-stream to detectors.

2.1.1 Initial state

The initial state of the HIC is probably the least understood stage of the collision. It is difficult to accurately model physics of strongly interacting particles too far from equilibrium. Many models attempt to simply recreate the initial geometry of the collision. One of the simplest and earliest models attempting to do this is the Optical Glauber model [37, 38]. The nucleon density inside a nucleus is well approximated by the Woods-Saxon parameterization [39]

$$\rho(r) = \rho_0 \frac{1}{1 + \exp \frac{r - R}{a}}. \quad (2.1)$$

Here ρ_0 is the density at the centre of the nucleus, R is the charge radius of the nucleus and a is the nuclear skin-thickness. One can then define the thickness function in the Glauber model as

$$T_{A/B}(\mathbf{s}) = \int_{-\infty}^{+\infty} \rho_{A/B}(\mathbf{s}, z_{A/B}) dz_{A/B}. \quad (2.2)$$

Here A/B stands for target/projectile, \mathbf{s} is the transverse position while z is the position in the longitudinal direction. The energy density at \mathbf{s} is then proportional to $\sigma_{NN} T_A(\mathbf{s}) T_B(\mathbf{s} - \mathbf{b})$ where σ_{NN} is the inelastic cross-section of the nucleon-nucleon collision.

The Optical Glauber model can be improved by using Monte Carlo techniques. Instead of using the Woods-Saxon distribution to evaluate the nuclear density at a point, it can be used to sample nucleons. This is the Monte Carlo (MC) Glauber model. Two nucleons are determined to have a binary collision when the distance between them (d) satisfies

$$d \leq \sqrt{\frac{\sigma_{NN}}{\pi}}. \quad (2.3)$$

In addition to the impact-parameter geometry that is also captured by the Optical Glauber model, the MC-Glauber model also captures the fluctuations of nucleon positions.

Both the Optical and the MC Glauber models incorporate geometric considerations and do not attempt to model initial-state dynamics. The energy density profile from both Glauber models is fed directly to hydrodynamics as the initial conditions some time after the collision (typically 0.4-0.8 fm/c). In general, there are no dynamics before the hydrodynamic start time.

IP-Glasma is a modern initial state model which dynamically evolves initial color fields [40, 41]. It is based on the color glass condensate (CGC) framework initially defined in the McLerran-Venugopalan (MV) model [42]. The idea is that nucleons traveling at high velocities have high soft gluon densities and thus a classical description of gluon fields is possible. Hard gluons and quarks act as color sources of this field and radiate gluons, which further radiate more gluons. As the gluon density keeps increasing, gluon recombination competes with gluon production. The energy scale where gluon radiation and gluon recombination equilibrate is called the gluon saturation scale. Gluon saturation has not yet been observed directly, though saturation based models have been quite successful. We will probe the gluon saturation mechanism more directly in deep inelastic scattering experiments at the upcoming Electron-Ion Collider (EIC) [43].

Like the MC-Glauber model, IP-Glasma begins by sampling nucleon positions using the Woods-Saxon distribution. At each nucleon position color charge is sampled using the MV model. IP-Glasma accounts for sub-nucleonic fluctuations in this sampling. The strength of these fluctuations is determined by the local saturation scale which in turn is determined by the IP-Sat model [44] which uses deep inelastic experiment data.

Field strength can be obtained from the sampled color charge densities. These fields are then evolved using the classical Yang-Mills equations

$$[D_\mu, F_a^{\mu\nu}] = J_a^\nu. \quad (2.4)$$

Here, D_μ is the gauge covariant derivative, $F_a^{\mu\nu}$ is the field strength tensor (see discussion after eq. (1.1) for definition), J_a^ν is the color source current, μ, ν are Lorentz indices running from 0 to 3 and a is the color index running from 1 to 8. At the end of the evolution, the energy-momentum tensor can be generated from the field strength tensor that can in turn be matched to the hydrodynamic energy-momentum tensor.

Recently, there has been increased interest in using QCD based kinetic theory approaches to evolve the dynamics after the initial state for some time before feeding it to hydrodynamic models [45]. The idea is to allow for thermalization, after which hydrodynamics is applicable. We have not used this approach in this work. Such an intermediate stage could be easily added to our framework in the future.

Both the Glauber model and the IP-Glasma model have been used in different parts of this work. Other initial state models like MC-KLN [46] and AMPT [47] are also in popular use, however we have restricted ourselves to using Glauber and IP-Glasma model in this work.

2.1.2 Hydrodynamic evolution

Hydrodynamics is the macroscopic theory concerned with the evolution of average thermodynamic quantities such as energy density and pressure. The relativistic hydrodynamic equation is basically just the energy-momentum conservation equation and can be written as

$$\partial_\nu T^{\mu\nu} = 0, \quad (2.5)$$

where $T^{\mu\nu}$ is the energy-momentum tensor, T^{00} is the energy density, T^{0i} is the energy flux in i^{th} direction, T^{i0} is the i^{th} component of momentum density and T^{ij} is the flux of i^{th} component of momentum in the j^{th} direction. Indices i and j run from 1 to 3.

When the fluid is in local thermal equilibrium, the fluid is dubbed ideal and $T^{\mu\nu}$ is given by

$$T^{\mu\nu} = T_{\text{id}}^{\mu\nu} = (\varepsilon + P)u^\mu u^\nu - P g^{\mu\nu}. \quad (2.6)$$

ε is the energy density, P is the pressure and u^μ is four-velocity satisfying the relation $u^\mu u_\mu = 1$, $g^{\mu\nu} = \text{diag.}(1, -1, -1, -1)$ is the metric tensor.

As u^μ is a unit four-vector, it has only three independent components. Along with ε and P , $T^{\mu\nu}$ has five independent components. We have four equations in eq. (2.5). To close the system we need an additional equation of state (EOS) relating ε and P . For QCD matter at vanishing baryon densities, the EOS can be obtained from lattice QCD [15, 48]. A lattice QCD EOS is shown in fig. 1.2.

When the system is away from local thermal equilibrium, it dissipates energy to maximize the entropy. In this state, the energy momentum tensor gains an additional dissipative, i.e., viscous, component $T_{\text{vis.}}^{\mu\nu}$.

$$T^{\mu\nu} = T_{\text{id.}}^{\mu\nu} + T_{\text{vis.}}^{\mu\nu}. \quad (2.7)$$

$T_{\text{vis.}}^{\mu\nu}$ can be further divided into shear and bulk viscous components as

$$T_{\text{vis.}}^{\mu\nu} = \pi^{\mu\nu} + \Delta^{\mu\nu} \Pi. \quad (2.8)$$

Here, $\pi^{\mu\nu}$ is the traceless shear viscous tensor, Π is the bulk pressure and $\Delta^{\mu\nu} = g^{\mu\nu} - u^\mu u^\nu$ is the projection tensor. There is a choice in how u^μ is defined (see [49]). We choose the definition by enforcing the eigenvalue equation

$$u_\mu T^{\mu\nu} = \varepsilon u^\nu. \quad (2.9)$$

This choice is known as working in the Landau frame [50]. It also leads to the relation $u_\mu \pi^{\mu\nu} = 0$. This constrains 3 components of $\pi^{\mu\nu}$. Another is constrained by eq. (2.9). Also, $\pi^{\mu\nu}$ is symmetric and traceless and so has 5 independent components. Π is another independent variable. We need 6 additional equations to close the system. In principle, one can write additional equations for currents of conserved quantities such as charge, baryon number etc. Each such addition will add 4 more independent components.

The non-relativistic version of the dissipative fluid dynamics is given by the famous Navier-Stokes theorem. Analogously, one can write the relativistic Navier-Stokes theorem. However, Navier-Stokes theory allows for infinite propagation speeds. This is a problem for a relativistic theory as it leads to causality violation [51], though recently a class of causal Navier-Stokes theories have been discovered [52]. These Navier-Stokes theories are causal for only certain definitions of out of equilibrium values of thermodynamic variables. Causal Navier-Stokes theories are still an active area of research [53] and their relation to second order theories (discussed below) is being actively investigated [54, 55]. In this thesis, we have not used these causal Navier-Stokes theories but used second order hydrodynamics.

Muller, Israel and Stewart first developed causal relativistic viscous hydrodynamics by including terms up to second order in the gradient expansion [56, 57]. The Muller-Israel-Stewart hydrodynamic equations are given by

$$\tau_\pi \dot{\pi}^{\langle\mu\nu\rangle} + \pi^{\mu\nu} = 2\eta\sigma^{\mu\nu} - \frac{4}{3}\tau_\pi\pi^{\mu\nu}\theta, \quad (2.10)$$

$$\tau_\Pi \dot{\Pi} + \Pi = -\zeta\theta - \frac{2}{3}\tau_\Pi\Pi\theta. \quad (2.11)$$

Here, η is the shear viscosity, ζ is the bulk viscosity, $\theta = \partial_\mu u^\mu$ is the expansion rate, $\sigma^{\mu\nu} = \partial^{\langle\mu} u^{\nu\rangle}$ is the Navier-Stokes tensor and τ_π and τ_Π are shear and bulk relaxation times, respectively. Angular brackets in the indices indicate the traceless part of the symmetrized tensor as $A^{\langle\mu\nu\rangle} = \frac{1}{2}(A^{\mu\nu} + A^{\nu\mu} - \frac{2}{3}\Delta^{\mu\nu}A^\alpha_\alpha)$. A dot above a variable denotes a proper time derivative such that $\dot{A} = u^\mu\partial_\mu A = dA/d\tau$.

There are various versions of second order hydrodynamics. A kinetic theory based derivation by Denicol, Niemi, Molnar and Rischke (DNMR) [58] uses the relativistic Boltzmann equation

$$k^\mu\partial_\mu f_{\mathbf{k}} = C[f]. \quad (2.12)$$

k^μ is the particle four-momentum, $f_{\mathbf{k}}$ is single particle distribution function and $C[f]$ is the collision kernel. DNMR included $2 \rightarrow 2$ collisions in $C[f]$. $f_{\mathbf{k}}$ is expanded in the complete and orthogonal basis formed by $1, k^\mu, k^{\langle\mu} k^{\nu\rangle}, k^{\langle\mu} k^{\nu} k^{\lambda\rangle} \dots$, where $k^{\langle\mu_1} k^{\mu_2} \dots k^{\mu_n\rangle}$ is defined as the traceless part of the tensor $k^{\mu_1} k^{\mu_2} \dots k^{\mu_n}$ symmetric in μ_1 and μ_n . Terms up to second order in Knudsen and inverse Reynolds numbers are kept. Knudsen number (K_n) is a dimensionless ratio of microscopic and macroscopic scale in a system

$$K_n = \frac{\lambda}{L}. \quad (2.13)$$

Here, λ is the microscopic length scale while L is the macroscopic length scale. Inverse Reynolds numbers give the ratio of viscous forces to equilibrium forces. Shear (R_π^{-1}) and bulk (R_Π^{-1}) inverse Reynolds numbers are given as

$$R_\pi^{-1} = \frac{\sqrt{|\pi^{\mu\nu}\pi_{\mu\nu}|}}{P}, \quad R_\Pi^{-1} = \frac{|\Pi|}{P}. \quad (2.14)$$

The Knudsen number and the inverse Reynolds number serve as appropriate small parameters in expansions. Small Knudsen number ensures the validity of long range effective theories like hydrodynamics and small inverse Reynolds number guarantees that the system is not far from equilibrium.

Along with the coefficients derived in [59, 60], the final DNMR hydrodynamics equations are

$$\tau_\pi \dot{\pi}^{\langle\mu\nu\rangle} + \pi^{\mu\nu} = 2\eta\sigma^{\mu\nu} - \frac{4}{3}\tau_\pi\pi^{\mu\nu}\theta + \frac{9}{70P}\pi_\alpha^{\langle\mu}\pi^{\nu\rangle\alpha} - \frac{10}{7}\tau_\pi\pi_\alpha^{\langle\mu}\sigma^{\nu\rangle\alpha} + \frac{6}{5}\tau_\pi\Pi\sigma^{\mu\nu}. \quad (2.15)$$

$$\tau_\Pi\dot{\Pi} + \Pi = -\zeta\theta - \frac{2}{3}\tau_\Pi\Pi\theta + \frac{8}{5}\left(\frac{1}{3} - c_s^2\right)\tau_\Pi\pi^{\mu\nu}\sigma_{\mu\nu}. \quad (2.16)$$

Relaxation times are obtained from the collision kernel and depend on the underlying interactions. They essentially provide the timescale in which dissipative modes decay. They are derived from the linearized collision term in [60] and are

$$\tau_\pi = \frac{5\eta}{(\varepsilon + P)}. \quad (2.17)$$

$$\tau_\Pi = \frac{\zeta}{(\varepsilon + P)} \frac{1}{14.55(1/3 - c_s^2)^2} \quad (2.18)$$

Relativistic hydrodynamics is a rich and active field. We have only listed two forms of viscous hydrodynamics here. More elaborate discussions of various versions of hydrodynamics equations and their derivations can be found in [49, 61].

2.1.2.1 Bjorken flow

The equations of hydrodynamics do not yield themselves to analytic solutions easily and few are available. The most popular one is the analytic solution given by J. D. Bjorken [62]. Bjorken introduced the idea of boost invariance, which means that in the z -direction, the velocity at a point is given by $v_z = z/t$. One can go to Milne coordinates τ, x, y, η , where x and y are normal Cartesian coordinates. We have proper time $\tau = \sqrt{t^2 - z^2}$ and spacetime rapidity $\eta_s = \tanh^{-1}(z/t)$. In Milne coordinates, Bjorken flow is simply given by $u = (1, 0, 0, 0)$. The solution is invariant under a Lorentz boost. It is important

to note that this does not imply a fluid at rest. Here the metric is $g^{\mu\nu} = (1, -1, -1, -\tau^2)$. So the space itself is expanding in the z -direction. This beautifully captures the rapidly expanding nature of the system in the z -direction. Assuming a simple equation of state where $\varepsilon \propto P$, analytic and semi-analytic solutions can be found for energy density in the ideal and viscous cases respectively.

The Bjorken solution provides us with a simple solution that closely resembles the dynamics of HICs and is used as a testing ground of many new ideas. However, more realistic simulations of HIC require numerical solutions of viscous hydrodynamics. We use our in-house hydrodynamic approach MUSIC to solve these equations [32].

2.1.2.2 MUSIC

MUSIC uses the Kurganov-Tadmor (KT) method [63] coupled with Heun's method for solving hydrodynamic equations in Milne coordinates. Using Milne coordinates ensures that we do not have to use a rapidly expanding grid in the z -direction. We closely follow the discussion in [32] in this section to describe the working of MUSIC.

The KT method is used for evaluating spatial derivatives. It has the advantage that it can accurately propagate discontinuities and shock-waves and has small numerical viscosity. As HICs can have shock waves and QGP has a very small viscosity, the KT algorithm is a good fit for our purpose. To illustrate the KT method, let us take a simple one-dimensional partial differential equation

$$\partial_t \rho = -\partial_x J, \quad (2.19)$$

where ρ is a density and $J = v\rho$ is current with propagation speed v . Discretized coordinates are represented as $t^n = n\Delta t$ and $x_j = j\Delta x$. Here Δt and Δx are step sizes in temporal and spatial directions, respectively.

The KT algorithm uses spatially cell-averaged values around x_j instead of just using the value at $x = x_j$. So, the cell averaged density is

$$\bar{\rho}_j(t) = \frac{1}{\Delta x} \int_{x_{j-1/2}}^{x_{j+1/2}} \rho(x, t) dx. \quad (2.20)$$

The discretized version of eq. (2.19) becomes

$$\frac{d\bar{\rho}_j(t)}{dt} = \frac{J(x_{j-1/2}, t) - J(x_{j+1/2}, t)}{\Delta x} \quad (2.21)$$

This is important for our purposes. When we solve stochastic hydrodynamic equations in part II, we will be sampling the cell-averaged noise.

We present the final KT algorithm here:

$$\frac{d\bar{\rho}_j(t)}{dt} = \frac{H(x_{j-1/2}, t) - H(x_{j+1/2}, t)}{\Delta x}, \quad (2.22)$$

with

$$H(x_{j\pm 1/2}, t) = \frac{J(x_{j\pm 1/2,+}, t) + J(x_{j\pm 1/2,-}, t)}{2} - |v_{j\pm 1/2}(t)| \left(\frac{\bar{\rho}_{j\pm 1/2,+}(t) - \bar{\rho}_{j\pm 1/2,-}(t)}{2} \right), \quad (2.23)$$

and

$$\bar{\rho}_{j+1/2,+} = \bar{\rho}_{j+1} - \frac{\Delta x}{2}(\rho_x)_{j+1}, \quad (2.24)$$

$$\bar{\rho}_{j+1/2,-} = \bar{\rho}_j + \frac{\Delta x}{2}(\rho_x)_j. \quad (2.25)$$

Spatial derivatives $(\rho_x)_j$ are evaluated using a minmod flux limiter as

$$(\rho_x)_j = \text{minmod} \left(\ominus \frac{\bar{\rho}_{j+1} - \bar{\rho}_j}{\Delta x}, \frac{\bar{\rho}_{j+1} - \bar{\rho}_{j-1}}{2\Delta x}, \ominus \frac{\bar{\rho}_j - \bar{\rho}_{j-1}}{\Delta x} \right). \quad (2.26)$$

The minmod limiter is defined as

$$\text{minmod}(x_1, x_2, x_3 \dots) = \begin{cases} \min\{x_j\} & \text{if } x_j > 0 \forall j, \\ \max\{x_j\} & \text{if } x_j < 0 \forall j, \\ 0 & \text{otherwise.} \end{cases} \quad (2.27)$$

Minmod flux limiter constrains the value of flux to realistic values. Second order derivative is normally preferred. If the magnitude of the second order derivative is larger than \ominus times the first order derivative, we switch to the latter. This puts a weight against the first order derivative, while still limiting the flux when second order derivative becomes too large. This preserves the accuracy around sharp edges and shock waves and ensures that no spurious oscillations are introduced. The weighting factor \ominus is the minmod parameter which controls when that switch needs to be made. We have set $\ominus = 1.8$ in all recent analysis of hadronic phenomenology.

Temporal evolution is done using Heun's method, which is a form of second order Runge-Kutta solver. Heun's method solves an ordinary differential equation of the form

$$\frac{d\rho}{dt} = f(t, \rho), \quad (2.28)$$

in the following steps:

1. Evaluate the intermediate variable $\tilde{\rho}^{n+1}$ from ρ^n as

$$\tilde{\rho}^{n+1} = \rho^n + \Delta t f(t, \rho^n). \quad (2.29)$$

2. Finally, evaluate ρ^{n+1} as

$$\rho^{n+1} = \rho^n + \frac{\Delta t}{2} [f(x, \rho^n) + f(t + \Delta t, \tilde{\rho}^{n+1})]. \quad (2.30)$$

Using Heun's method is also important for us as it is consistent with the Stratonovich form of the stochastic integral, which is the physical integration of choice while solving stochastic equations with non-linear multiplicative noise [64], as we do in part II.

2.1.3 Hadronization

We obtain the values of all hydrodynamic variables on an isothermal hypersurface from MUSIC. The exact switching temperature between hydrodynamics and hadrons is a parameter of the theory and is fixed to match the data. We use a switching temperature of 145 MeV as in [41, 65]. We use the Cooper-Frye prescription to switch from a fluid to a particle description on this hypersurface [66]. The particle production rate is given as

$$E \frac{dN}{d^3\mathbf{p}} = \frac{g}{(2\pi)^3} \int_{\sigma} f(x, p) p_{\mu} d\Sigma^{\mu}. \quad (2.31)$$

Here, $d\Sigma^{\mu}$ is the differential surface four-vector, g is particle degeneracy, p_{μ} is the four momentum of the surface patch and $f(x, p)$ is the particle distribution as a function of particle four-position x and particle four-momentum p .

The distribution function has equilibrium and viscous contributions

$$f = f_{\text{eq.}} + \delta f_{\text{shear}} + \delta f_{\text{bulk}}. \quad (2.32)$$

The equilibrium distribution for a Fermi/Bose particle at vanishing chemical potential is

$$f_{\text{eq.}} = \frac{1}{\exp p \cdot u / T \pm 1}. \quad (2.33)$$

The exact form of the viscous corrections to the particle distribution function depend on the approach. They could be derived in the Chapman-Enskog [67] or the Grad's 14 moment [68] approaches. Chapman-Enskog approach expands the distribution function in powers of Knudsen number (see eq. (2.13)) while Grad's approach expands it in the powers of particle momentum. Equations could be further simplified by using the relaxation-time approximation which assumes that the collision kernel in Boltzmann equation is proportional to the out-of-equilibrium correction in the distribution function divided by a relaxation time. We use the forms for shear and bulk corrections as has been used in [41, 65]. The shear corrections were derived using the Grad's approach [69] while the bulk correction was obtained from the Chapman-Enskog approach in the relaxation-time approximation [70, 71]. The expressions for viscous corrections are

$$\delta f_{\text{shear}} = f_{\text{eq.}} (1 \pm f_{\text{eq.}}) \pi_{\mu\nu} \frac{p^\mu p^\nu}{2(\varepsilon + P)T^2}, \quad (2.34)$$

$$\delta f_{\text{bulk}} = f_{\text{eq.}} (1 \pm f_{\text{eq.}}) \left(\frac{-\Pi}{\zeta/\tau_\Pi} \right) \frac{1}{3T} \left(\frac{m^2}{E} - (1 - 3c_s^2)E \right). \quad (2.35)$$

Here m is the particle mass while c_s is the speed of sound. These terms have the property that they ensure the continuity of the non-equilibrium corrections. We use the publicly available particle sampler iSS [72] to sample all the hadrons listed in the hadronic cascade package UrQMD. In the next step, we feed all these hadrons to UrQMD.

From every event in MUSIC, we oversample. From each freezeout hyper-surface, we sample particles of the order of 100 times to accurately reproduce the underlying event and to ensure that random sampling fluctuations do not distort the hydrodynamic signal [73]. Later, while evaluating particle multiplicities, we divide by the oversampling factor.

2.1.4 Hadronic cascade

At this stage of the collisions, the Knudsen number becomes large. The mean free path of particles is large and hydrodynamics is no longer applicable. This is the regime of kinetic theory.

We use the Ultra-relativistic Quantum Molecular Dynamics (UrQMD) code to undertake the hadronic cascade [74, 75]. UrQMD evolves hadrons by solving the Boltzmann equation. Elastic and inelastic collisions are allowed. Measured hadronic cross-sections are used for the collision kernel in the Boltzmann equation and model calculations are substituted when experimental measurements are not available. UrQMD also allows for the decay of hadron resonances.

UrQMD stops when particle density falls so low that no further interaction is possible and all resonances have decayed. It gives a list of final particles from which all the observables described in section 3.3 are evaluated.

We will extend this soft-hadronic framework to include thermal fluctuations in part II

2.2 MODELLING JET PHYSICS

While collective dynamics is governed by the strong coupling, hard jets are in the weakly-coupled limit because of their high energy. We now use the framework shown in the rightmost column in fig. 2.1.

We use the hybrid model to evolve the jets in medium [76]. This model is a “hybrid” between the strongly coupled and weakly coupled physics. The jet interaction with the plasma is assumed to happen by exchanging soft modes in the strongly coupled limit while the jet splittings happen in the weakly coupled limit.

In our model, we begin by using the PYTHIA event generator [77] to generate parton showers. Parton showers are created by hard partons that gain large momentum by hard scattering at the moment of collision. PYTHIA uses the DGLAP formalism [78–80] to evolve partons to generate a shower. PYTHIA is applicable for $p - p$ collisions in vacuum. Here, we work under the assumption that the initial showering is unaffected by initial dynamics of the collision. This is justified because all the hard partons created at

the collision have very high virtuality, i.e. they are very off-shell. In fact, the virtuality is much higher than any scale of the medium. We embed these showers at the location of binary collisions described in section 2.1.1.

We further assume that jet splittings in medium is also governed by the DGLAP formalism. This is approximately true for energetic partons with high virtuality. This assumption becomes questionable at later stages of the collision, though we can expect the jets to have left the medium by that stage. We are neglecting the jet splittings caused by medium interactions.

In our framework, these showers free-stream until the hydrodynamic initialization time, at which point shower partons start interacting with the medium. In the hybrid model, energy loss is evaluated in the approximation of a light quark jet propagating through a strongly coupled $N = 4$ Supersymmetric Yang Mills plasma by holography [81, 82]. The quark-jet stopping in a medium could be mapped to a 1-D string falling into a black hole in 5-D gravity; which could be solved analytically. In this approach, the energy loss is given as

$$\frac{dE}{dx} = -\frac{4}{\pi} E_0 \frac{x^2}{x_{\text{stop}}^2} \frac{1}{\sqrt{x_{\text{stop}}^2 - x^2}}. \quad (2.36)$$

Here, E_0 is the initial parton energy, x is the distance covered by the parton in the medium, and x_{stop} is the distance a parton will cover before losing all its energy if it were travelling in a medium with constant temperature. Clearly, x_{stop} must be a function of temperature. It is given as

$$x_{\text{stop}} = \frac{1}{2\kappa_{\text{sc}}} \frac{E_0^{1/3}}{T^{4/3}}. \quad (2.37)$$

$\kappa_{\text{sc}} = 1.05\lambda^{1/6}$ where λ is the 't Hooft coupling. In this model, κ_{sc} is a tunable parameter which can be fit to data.

Traditionally, hard parton energy loss models take temperature information from a hydrodynamic model such as MUSIC. Hydrodynamics provides the temperature at each space-time point, allowing one to simulate jet propagation in medium. In part III we will simultaneously evolve MUSIC with the hybrid model allowing for the feedback from jet energy loss to hydrodynamics. Energy lost by jets should be added to the soft medium for total energy-momentum conservation.

Once the hard partons leave the medium, they could be hadronized using the Lund string model [83] encoded in PYTHIA. The Lund string model approximates confinement dynamics by taking a linear potential between a quark anti-quark pair. The string oscillates and fragments, forming more hadrons.

A recent development in the Lund string model allows us to obtain spatial positions of fragmented hadrons along with the traditional momentum information [84]. This is already available with PYTHIA. Complete spatial and momentum information allows us to feed these hadrons together with the soft hadrons from the Cooper-Frye prescription to hadronic cascade models such as UrQMD. As before, a final particle list from UrQMD can be used to evaluate observables described in section 3.4.

The direct PYTHIA shower can be used to provide the p-p collision baseline for evaluating the nuclear modification factor (see section 3.4).

We want to point out that there are alternate approaches which treat the jet-medium interaction in the weakly coupled limit (for example, see [85, 86]). In this work we have chosen the hybrid model for its simplicity. In our concurrent framework developed in chapter 9, hybrid model can be easily replaced by any other jet energy-loss model. Comparing the predictions of our concurrent framework with data with different energy-loss mechanisms will potentially help us constrain the models.

2.3 MODELLING HEAVY-FLAVOR DYNAMICS

Similar to hard light quark jets, heavy quark (HQ) dynamics in QGP can be modelled by sampling and propagating HQs through the medium. But instead of using event by event simulations, we explore a different approach here. We model HQ dynamics using Fokker-Planck equations and evaluate fundamental HQ dissipation coefficients such as drag and diffusion coefficients in QGP. Crucially, the HQ-medium interaction is treated here in the weakly-coupled limit.

We use the formalism developed in [87]. HQ dynamics can be described by the Boltzmann equation

$$p^\mu \partial_\mu f_{HQ} = \left(\frac{\partial f_{HQ}}{\partial t} \right)_c, \quad (2.38)$$

where f_{HQ} is the HQ distribution function and the right hand side is the collision kernel. In the limit of soft momentum transfer, the Boltzmann equation reduces to the Fokker-Planck equation

$$\frac{\partial f_{HQ}}{\partial t} = \frac{\partial}{\partial p_i} \left[A_i(\mathbf{p}) f_{HQ} + \frac{\partial}{\partial p_j} [B_{ij}(\mathbf{p}) f_{HQ}] \right], \quad (2.39)$$

Here, $A_i(\mathbf{p})$ and $B_{ij}(\mathbf{p})$ denote drag force and momentum diffusion, respectively. For an HQ interacting with a light quark l by $HQ(p) + l(q) \rightarrow HQ(p') + l(q')$, A_i and B_{ij} can be written as

$$\begin{aligned} A_i &= \frac{1}{\gamma_c} \frac{1}{2P^0} \int \frac{d^3 \mathbf{q}}{(2\pi)^3 2Q^0} \int \frac{d^3 \mathbf{p}'}{(2\pi)^3 2P'^0} \int \frac{d^3 \mathbf{q}'}{(2\pi)^3 2Q'^0} \\ &\quad \times (2\pi)^4 \delta^4(P + Q - P' - Q') \sum | \mathcal{M}_{HQ,g/q} |^2 \\ &\quad \times f_{g/q}(Q) \left(1 \pm f_{g/q}(Q') \right) (\mathbf{p} - \mathbf{p}')_i \\ &\equiv \langle \langle (\mathbf{p} - \mathbf{p}')_i \rangle \rangle, \end{aligned} \quad (2.40)$$

and

$$\begin{aligned} B_{ij} &= \frac{1}{2\gamma_c} \frac{1}{2P^0} \int \frac{d^3 \mathbf{q}}{(2\pi)^3 2Q^0} \int \frac{d^3 \mathbf{p}'}{(2\pi)^3 2P'^0} \int \frac{d^3 \mathbf{q}'}{(2\pi)^3 2Q'^0} \\ &\quad \times (2\pi)^4 \delta^4(P + Q - P' - Q') \sum | \mathcal{M}_{HQ,g/q} |^2 \\ &\quad \times f_{g/q}(Q) \left(1 \pm f_{g/q}(Q') \right) (\mathbf{p} - \mathbf{p}')_i (\mathbf{p} - \mathbf{p}')_j \\ &\equiv \langle \langle \frac{1}{2} (\mathbf{p} - \mathbf{p}')_i (\mathbf{p} - \mathbf{p}')_j \rangle \rangle. \end{aligned} \quad (2.41)$$

Here, γ_c are HQ degeneracy and $| \mathcal{M}_{HQ,g/q} |$ are $2 \rightarrow 2$ scattering matrix elements evaluated in [87]. Fig. 2.2 shows the evaluated diagrams. We are including only $2 \rightarrow 2$ scattering between a HQ and a light quark/gluon. There will be additional comparable contributions to HQ energy loss from radiative loss [88], which has not been considered in this analysis. This is because our immediate goal here is not to predict experimental observables but to evaluate the out-of-equilibrium effects on HQ-medium scatterings. This has been done in chapter 10. A complete calculation including the scattering and radiative energy loss has been left for future work.

$A_i(\mathbf{p})$ and $B_{ij}(\mathbf{p})$ can be decomposed as

$$A_i = p_i A(p^2, T), \quad (2.42)$$

$$B_{ij} = \left(\delta_{ij} - \frac{p_i p_j}{p^2} \right) B_0(p^2, T) + \frac{p_i p_j}{p^2} B_1(p^2, T), \quad (2.43)$$

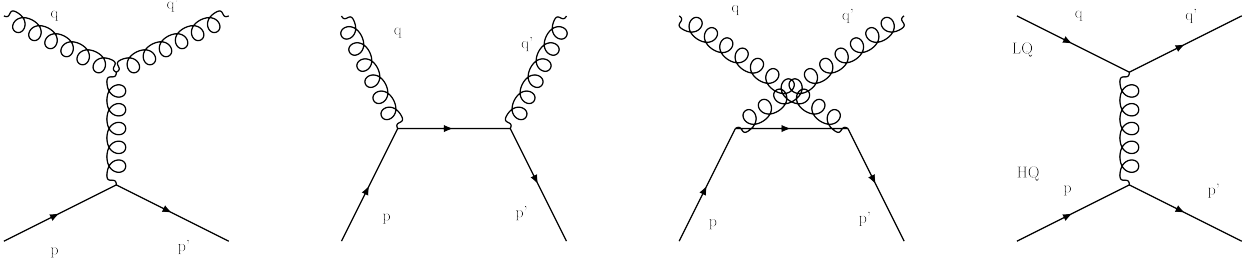


Figure 2.2: $2 \rightarrow 2$ scattering diagrams for HQ interaction with the medium. In the first three diagrams, the quarks are HQ.

Here $p^2 = |\mathbf{p}|^2$. A is the drag coefficient, B_0 and B_1 are transverse and longitudinal diffusion coefficients, respectively. The coefficients can be written as

$$A = \langle\langle 1 \rangle\rangle - \langle\langle \mathbf{p} \cdot \mathbf{p}' \rangle\rangle / p^2, \quad (2.44)$$

$$B_0 = \frac{1}{4} \left[\langle\langle p'^2 \rangle\rangle - \langle\langle (\mathbf{p} \cdot \mathbf{p}')^2 \rangle\rangle / p^2 \right], \quad (2.45)$$

$$B_1 = \frac{1}{2} \left[\langle\langle (\mathbf{p} \cdot \mathbf{p}')^2 \rangle\rangle / p^2 - 2 \langle\langle \mathbf{p} \cdot \mathbf{p}' \rangle\rangle + p^2 \langle\langle 1 \rangle\rangle \right]. \quad (2.46)$$

In part III we will extend this framework to include viscous corrections in light quark distribution functions.

2.4 MODELLING PHOTON EMISSION

Finally, we discuss photon emission in QGP. We will restrict our attention to thermal photons emitted by $2 \rightarrow 2$ scattering in QGP and meson gas.

For a $2 \rightarrow 2$ process $1 + 2 \rightarrow 3 + \gamma$ generating photons, the emission rate for photons of energy E_p and momentum \mathbf{p} is given as

$$E_p \frac{dN}{d^3\mathbf{p}} = \frac{1}{2} \int_{\mathbf{p}_1, \mathbf{p}_2, \mathbf{p}_3} |\mathcal{M}|^2 2\pi \delta^4(p_1 + p_2 - p_3 - p) f(p_1) f(p_2) (1 \pm f(p_3)). \quad (2.47)$$

$\int_{\mathbf{q}} \equiv \frac{1}{(2\pi)^3} \int \frac{d^3q}{E_q}$. f are the parton/meson distribution functions. For a meson gas, the matrix elements and shear viscous correction were evaluated in [89].

For $2 \rightarrow 2$ Compton scattering and annihilation in QGP, the situation simplifies even further under the forward scattering approximation. Assuming that the momentum ex-

change is soft, we can write the photon emission rate for photons of energy E_p and momentum \mathbf{p} [90]

$$E_p \frac{dN}{d^3\mathbf{p}} = \frac{5}{9} \frac{\alpha_e \alpha_s}{2\pi^2} f_a(p) T^2 \log \left[\frac{3.7388E}{g^2 T} \right]. \quad (2.48)$$

Here, f_a is a medium quark's distribution function.

In part II we extend these rates to include perturbative thermal fluctuation corrections and evaluate photon spectra and v_2 .

2.5 SUMMARY

In this chapter we have presented the composite model used to describe the HIC in this thesis. In section 2.1 we discussed the hydrodynamic framework used to describe the collective dynamics of QGP. Hydrodynamics is complemented by the initial-state models and a hadronic cascade framework to simulate the HICs. In part II, we will introduce the soft thermal hydrodynamic fluctuations in this model.

In section 2.2, we present the hybrid model of jets. This model treats the jet splittings in the weakly coupled limit and the jet medium interactions in the strongly coupled limit. We will include the feedback from the medium in this approach by concurrently evolving the jet and the QGP in chapter 9 in part III. The goal is to evaluate the effects of medium feedback and see how that helps us extract the properties of QGP. In future, the hybrid model can be easily replaced by any other jet-medium interaction model.

The HQ-medium interaction is discussed in the Fokker-Planck approach in section 2.3. Here the HQ-medium interaction is treated in the weakly coupled limit. We will evaluate the out-of-equilibrium corrections to this approach in chapter 10 in part III.

Finally, an approach to evaluate the photon spectra is discussed in section 2.4. In chapter 6 in part II we will estimate the effects of thermal fluctuations on photon observables.

These different approaches are necessary to study different aspects of HICs. As stated earlier, the goal of this thesis is to complete upon the existing models to include physical processes that have largely been neglected until now. For this purpose, our choice of models has been a mix of realistic and simplistic models. Many studies on thermal fluctuations have been done using simple flows (see chapter 5). These studies do not

lend themselves to obvious generalizations in a realistic simulation, which encounters technical difficulties described in section 5.5. For this reason we have undertaken the state-of-the-art model of collective dynamics to resolve these difficulties and do realistic simulations including thermal fluctuations.

So far, the effects of thermal fluctuations on electromagnetic observables have not been evaluated. Hence we undertake an exploratory study to assess these effects using the simplifying approximations made in section 2.4. A more realistic calculation using all the photon-production channels described in [71] will be done in future.

Similarly, we chose the hybrid model of jet-medium interaction for its simplicity. This helps us develop our new concurrent jet-medium evolution framework. In future, the hybrid model can be replaced by any other jet-medium interaction model allowing us to do a comparative study between different models.

Finally a Fokker-Planck approach is undertaken to study the HQ-medium interaction. This is a deterministic approach which is not computationally demanding and could be used for doing estimations of the size of out-of-equilibrium effects. The viscous corrections evaluated in this work can be used in more realistic (though also more computationally demanding) event by event simulations in the future.

OBSERVABLES IN HIC EXPERIMENTS

In this chapter, we discuss some of the observables measured in heavy-ion collisions and the physical insights derived from them.

3.1 RAPIDITY AND PSEUDORAPIDITY

We begin by describing the coordinate system used to report experimental observables. The beam axis is used as a reference and defined as the z axis. The plane perpendicular to the beam axis is identified as the “transverse plane”. Experimental observables are reported in terms of the azimuthal angle on the transverse plane. Along the beam axis, quantities are reported in terms of rapidity (y) or pseudorapidity (η). Pseudorapidity is defined in terms of the angle between the particle momentum (\mathbf{p}) and the z axis (θ)

$$\eta = -\log \left[\tan \left(\frac{\theta}{2} \right) \right] = \frac{1}{2} \log \left(\frac{|\mathbf{p}| + p_z}{|\mathbf{p}| - p_z} \right). \quad (3.1)$$

In the limit of massless particles, pseudorapidity is similar to another commonly used coordinate rapidity, which is defined as

$$y = \frac{1}{2} \log \left(\frac{E + p_z}{E - p_z} \right). \quad (3.2)$$

Observables at $\eta = y = 0$ are said to be at midrapidity. Particle rapidities and pseudorapidities are related to, but not the same as, spacetime rapidity described in section [2.1.2.1](#).

3.2 MULTIPLICITY AND CENTRALITY

Next, we describe centrality, which is another parameter whose dependence is reported in experiments. It is useful as it is a measure of the size of fireball created in the collision

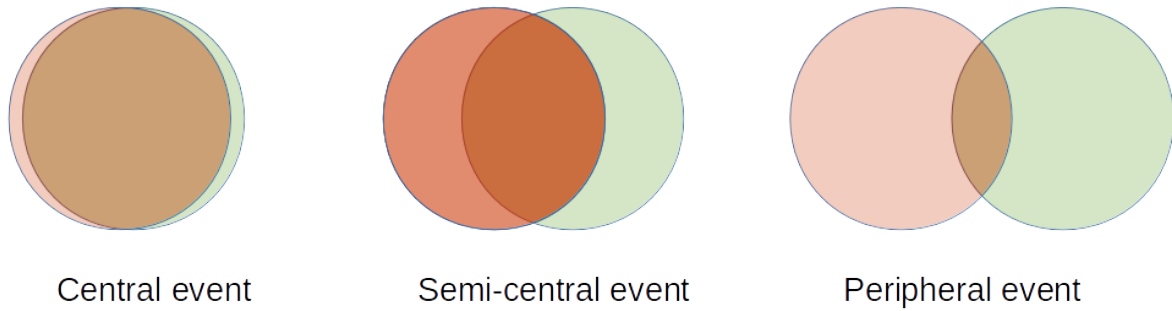


Figure 3.1: Illustration of the centrality of a collision event. Red and green circles denote projectile and target nuclei respectively. The overlap area in collisions reduces as one goes from central to peripheral collisions.

and is thus related to the magnitude of the interaction. Collision events in heavy-ion experiments are binned in terms of centralities, which have an intuitive meaning in HIC. Collisions with smaller impact parameter have larger overlap area between the colliding nuclei leading to more binary collisions between nucleons and are called more central. Collisions with larger impact parameters have smaller overlap regions and fewer binary collisions. Fig. 3.1 illustrates centralities. Central collisions have more energy and entropy going into QGP. They also tend to have a more circular shape in comparison to peripheral events, which have an increasingly elliptical overlap region.

In experiments, it is impossible to determine the impact parameter. Centrality is connected to entropy in QGP, which directly translates to the number of final particles. Thus, the final particle multiplicities are used to classify the centrality of an event. Essentially all the events in a collision are ordered by decreasing multiplicities. This total set of all events is called a minimum bias set. The top 5% of events by multiplicity are said to be in the 0 – 5% centrality bin, the next 5% are said to be in the 5 – 10% centrality bin and so on. Fig. 3.2 shows this binning process.

With centrality classes determined, average particle multiplicities are reported as a function of centrality. Within a centrality class, particle multiplicities can be reported as a function of pseudorapidity or transverse momentum (p_T). Fig. 3.3 shows the charged hadron multiplicities as functions of pseudorapidity and p_T as measured in experiment.

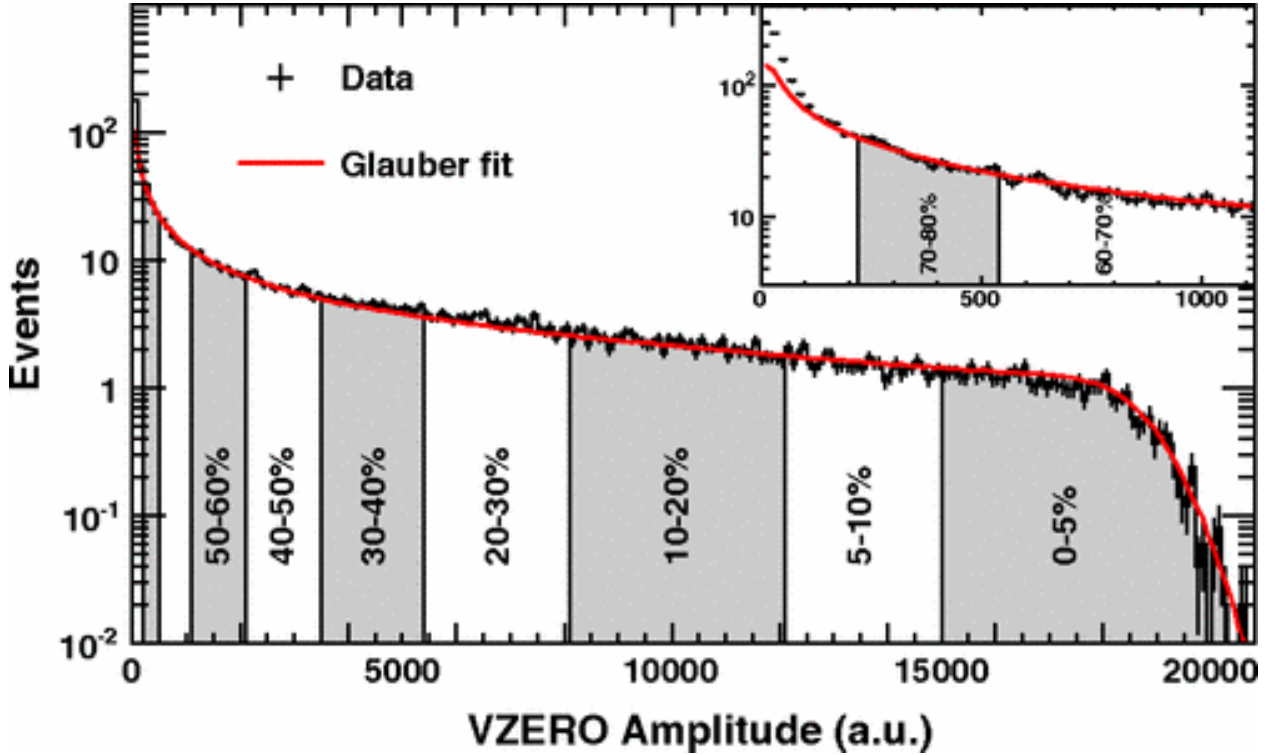


Figure 3.2: Centrality binning for Pb-Pb collisions at $\sqrt{s} = 2.76$ TeV. VZERO amplitude is a proxy for multiplicity in an event. Figure taken from the ALICE collaboration [91].

3.3 SOFT HADRONIC OBSERVABLES

In this thesis, hadronic observables are broadly divided into “soft” and “hard”, according to the p_T of the measured particles. The range of soft observables is typically $p_T < 2$ GeV while hard observables usually denote $p_T > 10$ GeV. These two ranges are governed by different physics; the soft region is dominated by the collective behaviour of the QGP described in section 2.1, while the hard region is dominated by hard partons traversing the QGP medium as described in section 2.2. Perturbative techniques can be used for hard physics but they are not applicable for the soft regions. Intermediate p_T ranges between 2 and 10 GeV and is more difficult to capture as it contains both soft and hard features [94]. We have made some progress in modelling the intermediate p_T region, which is reported in chapter 9.

We now describe some important soft observables evaluated in this work in some detail.

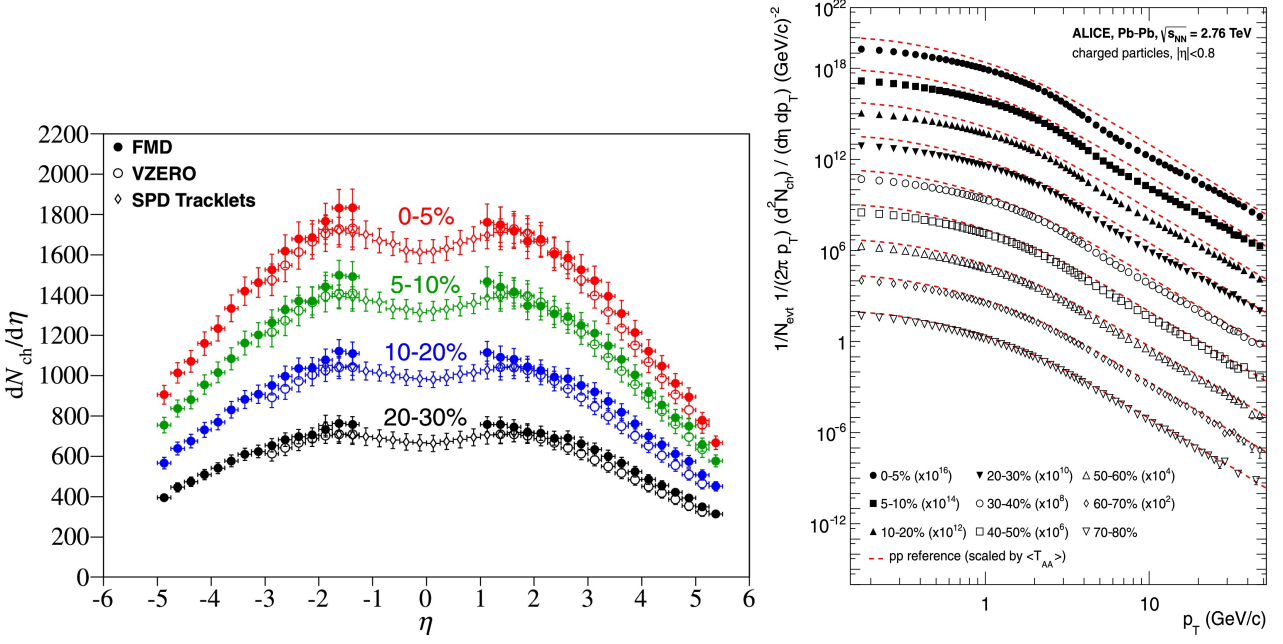


Figure 3.3: Charged particle multiplicities for different centrality bins as a function of pseudorapidity (left) and transverse momentum (right) for Pb-Pb collisions at $\sqrt{s} = 2.76$ TeV. Figures taken from the ALICE collaboration [92, 93].

3.3.1 Harmonic coefficients of anisotropic flow

The particle distribution can be decomposed in terms of its Fourier coefficients as

$$\frac{d^3N}{p_T dp_T d\phi d\eta} = \frac{d^2N}{2\pi p_T dp_T d\eta} \left[1 + \sum_1^{\infty} 2v_n(p_T) \cos(n\phi - n\Psi_n(p_T)) \right]. \quad (3.3)$$

Here, v_n are the harmonic response coefficients of the n^{th} order, ϕ is the azimuthal angle and Ψ_n s are the event plane angles. The true reaction plane angle cannot be determined experimentally and event plane angles work as proxies. Event plane angles can be determined as [95]

$$\Psi_n = \left(\tan^{-1} \frac{\sum_i \sin(n\phi_i)}{\sum_i \cos(n\phi_i)} \right) / N. \quad (3.4)$$

Here, the summation index i runs over all N particles and ϕ_i are the azimuthal angles of individual particles.

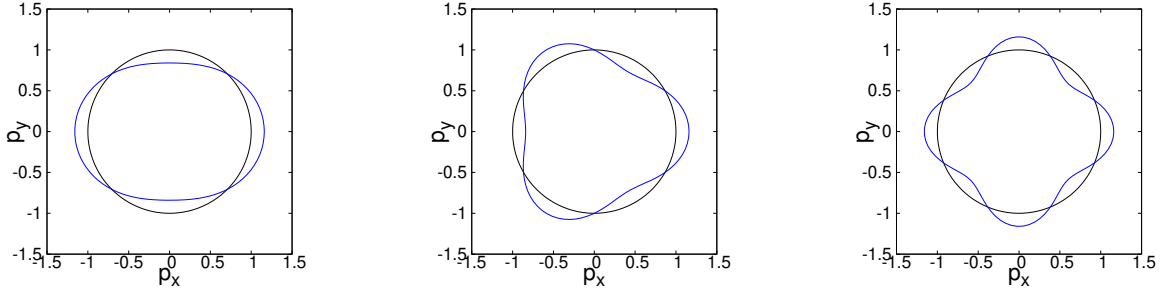


Figure 3.4: Polar plots of $1 + 2v_n \cos(n\phi)$ for small v_n (in blue). They denote elliptic (left), triangular (centre) and quadrangular (right) flow for $n = 2, 3$ and 4 respectively. Black circles show isotropic flow and are drawn for reference.

In a similar vein, 2D flow vectors \mathbf{Q}_n can be defined as

$$Q_{n,x} = \sum_i \cos(n\phi_i) / N, \quad (3.5)$$

$$Q_{n,y} = \sum_i \sin(n\phi_i) / N. \quad (3.6)$$

In complex notation,

$$\mathbf{Q}_n = \frac{1}{N} \sum_{j=1}^N e^{in\phi_j}. \quad (3.7)$$

Note that v_n are measured in momentum space. Fig. 3.4 illustrates the momentum anisotropy quantified by v_n s. In fact, large v_n s are strong signal of collective behaviour and are evidence of the existence of QGP after the collisions [96]. In the absence of QGP formation, hadrons formed in collisions will still interact with each other to generate v_n s, though their magnitude will be much smaller than what is observed in experiments [97]. Fig. 3.5 illustrates momentum anisotropy from collective behaviour.

Harmonic response coefficients are typically measured by correlations between different particles. Since all particles are correlated with the reaction plane, it stands to reason that they are correlated amongst themselves. There are many different methods to extract v_n from experiments and they can be described in terms of the flow vectors for an event. Two popular methods to measure v_n s are described here.

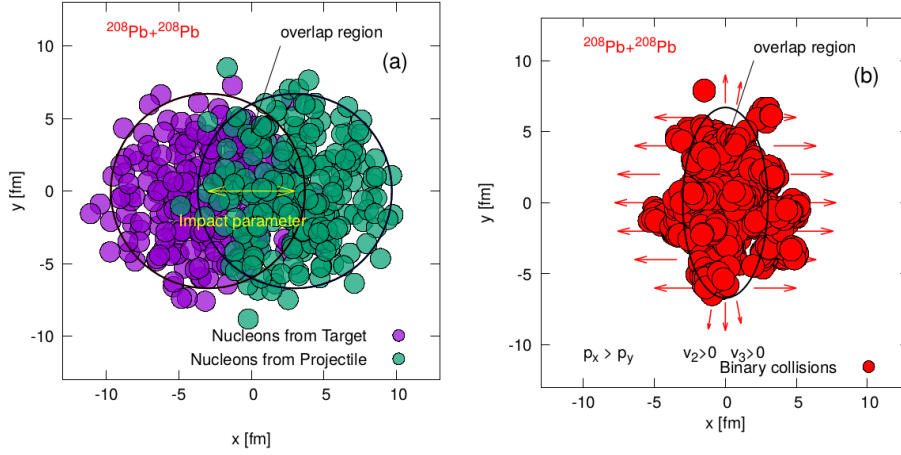


Figure 3.5: Illustration showing the conversion of pressure gradients to momentum anisotropy. Because of collective behaviour, there is larger pressure gradient in x direction than in y direction. This contributes to positive v_2 . v_3 is generated from the fluctuations in nucleon position within the nuclei (and sub-nucleonic fluctuations not shown here). Figure taken from [98].

3.3.1.1 Scalar product method

The scalar product (SP) method uses correlations between particles of interest (for example particles around some p_T at mid-rapidity) with reference particles (for example particles in a broader p_T range in some different rapidity bin). $v_n\{SP\}$ is defined as [99]

$$v_n\{SP\}(p_T) = \frac{\langle \text{Re}[\mathbf{Q}_n(p_T)(\mathbf{Q}_n^{\text{ref.}})^*] \rangle}{\sqrt{\langle \mathbf{Q}_n^{\text{ref.}}(\mathbf{Q}_n^{\text{ref.}})^* \rangle}}, \quad (3.8)$$

where angular brackets denote an average over events.

3.3.1.2 Two particle cumulant method

Another commonly used method directly calculates two-point correlations between the reference particles [100, 101]. The 2-particle correlator $\langle 2 \rangle_n$ is defined as

$$\langle 2 \rangle_n = \frac{1}{N(N-1)} \sum_{i,j;i \neq j}^N e^{in(\phi_i - \phi_j)} = \frac{N|\mathbf{Q}_n|^2 - 1}{N-1}. \quad (3.9)$$

The 2-particle correlator is then averaged over all events with the weight $N(N-1)$ to give $\langle \langle 2 \rangle \rangle_n$. Two particle cumulant is then given by

$$v_n\{2\} = \sqrt{\langle \langle 2 \rangle \rangle_n}. \quad (3.10)$$

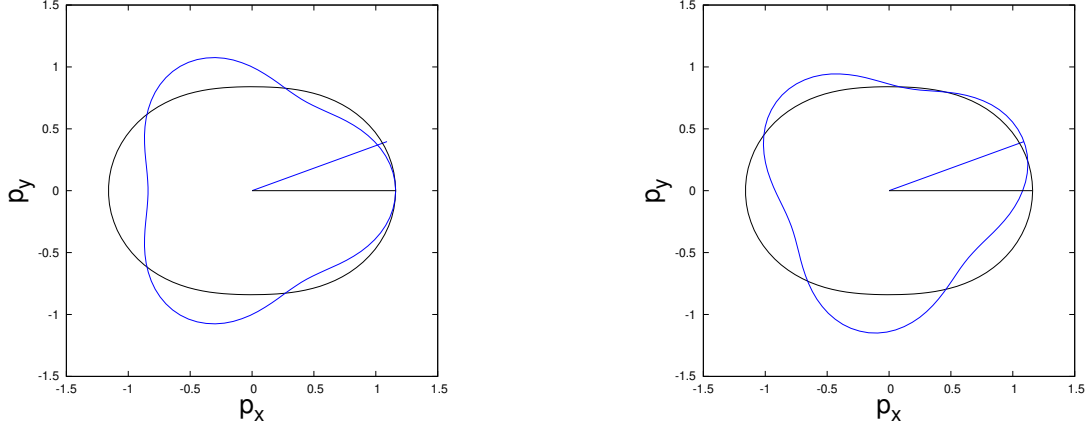


Figure 3.6: Illustration of EP correlators. When the event planes of v_2 and v_3 are perfectly aligned, then $3 \cdot 2 \cdot \Psi_2 - 2 \cdot 3 \cdot \Psi_3 = 0$ and $\cos[6(\Psi_2 - \Psi_3)] = 1$ (left). When they are not perfectly aligned, then the EPs are decorrelated and $\cos[6(\Psi_2 - \Psi_3)] < 1$ (right).

The procedure can be extended to measure p_T dependent differential v_n . Instead of 2-particle correlators, one can also use any $2k$ -particle correlator to obtain $v_n\{2k\}$, where k is an integer [101].

3.3.2 Event-plane (EP) correlators

Correlators between the event-plane angles (Ψ_n) defined in eq. (3.4) can be measured. These correlators will play an important role later in this work. These provide information about the fluctuations and their correlations in the QGP. Two and three plane EP correlators are given in terms of the flow vector as [102, 103]

$$\cos[c_1 n_1 \Psi_{n_1} - c_2 n_2 \Psi_{n_2}] = \frac{\text{Re}[\langle \mathbf{Q}_{n_1}^{c_1} (\mathbf{Q}_{n_2}^{c_2})^* \rangle]}{\sqrt{\langle \mathbf{Q}_{n_1}^{c_1} (\mathbf{Q}_{n_1}^{c_1})^* \rangle} \sqrt{\langle \mathbf{Q}_{n_2}^{c_2} (\mathbf{Q}_{n_2}^{c_2})^* \rangle}}, \quad (3.11)$$

$$\cos[c_1 n_1 \Psi_{n_1} + c_2 n_2 \Psi_{n_2} - c_3 n_3 \Psi_{n_3}] = \frac{\text{Re}[\langle \mathbf{Q}_{n_1}^{c_1} \mathbf{Q}_{n_2}^{c_2} (\mathbf{Q}_{n_3}^{c_3})^* \rangle]}{\sqrt{\langle \mathbf{Q}_{n_1}^{c_1} (\mathbf{Q}_{n_1}^{c_1})^* \rangle} \sqrt{\langle \mathbf{Q}_{n_2}^{c_2} (\mathbf{Q}_{n_2}^{c_2})^* \rangle} \sqrt{\langle \mathbf{Q}_{n_3}^{c_3} (\mathbf{Q}_{n_3}^{c_3})^* \rangle}} \quad (3.12)$$

For 2-plane EP correlators $c_1 n_1 - c_2 n_2 = 0$ and for 3-plane EP correlators $c_1 n_1 + c_2 n_2 - c_3 n_3 = 0$.

EP correlators measure the decorrelation between different event planes as shown in fig. 3.6, which is caused by event-by-event fluctuations in the collision events. EP correlators are crucial in quantifying and understanding these fluctuations.

3.3.3 Linear and non-linear response

Higher harmonic coefficients (v_4, v_5, v_6) can be understood as a sum of linear response to the initial state spatial anisotropy of the same order and a non-linear hydrodynamic response to smaller order harmonics. If we denote the magnitude and phase of v_n as

$$V_n = v_n e^{in\Psi_n}, \quad (3.13)$$

the linear (V_n^L) and the non-linear (χ_{npq}) response coefficients can be defined as

$$V_n = V_n^L + \sum_{n=p+q} \chi_{npq} V_p V_q. \quad (3.14)$$

Specifically, we have [104]

$$V_4 = V_4^L + \chi_{422} (V_2)^2, \quad (3.15)$$

$$V_5 = V_5^L + \chi_{523} V_2 V_3, \quad (3.16)$$

$$V_6 = V_6^L + \chi_{6222} (V_2)^3 + \chi_{633} (V_3)^2, \quad (3.17)$$

with

$$\chi_{422} = \frac{\langle V_4 (V_2^*)^2 \rangle}{\langle |V_2|^4 \rangle}, \chi_{523} = \frac{\langle V_5 V_2^* V_3^* \rangle}{\langle |V_2|^2 |V_3|^2 \rangle}, \chi_{6222} = \frac{\langle V_6 (V_2^*)^3 \rangle}{\langle |V_2|^6 \rangle}, \chi_{633} = \frac{\langle V_6 (V_3^*)^2 \rangle}{\langle |V_3|^4 \rangle}. \quad (3.18)$$

3.4 JET OBSERVABLES

Energetic parton jets open up another probe into QGP. Usually formed in pairs by an initial hard scattering, parton jets travel near the speed of light and lose energy by interacting with the medium. While both the jets in a dijet pair are created back-to-back with the same momentum at the initial collision time, they may lose different amounts of energy depending on the path-length travelled through the QGP medium. Parton jets hadronize once they leave the QGP and stream as energetic hadrons to the detector. The more energetic jet of the pair is called the leading jet while the other one is called the subleading jet. Our model for jet propagation through QGP is described in section 2.2. Two popular hard observables that we will focus on are described here.

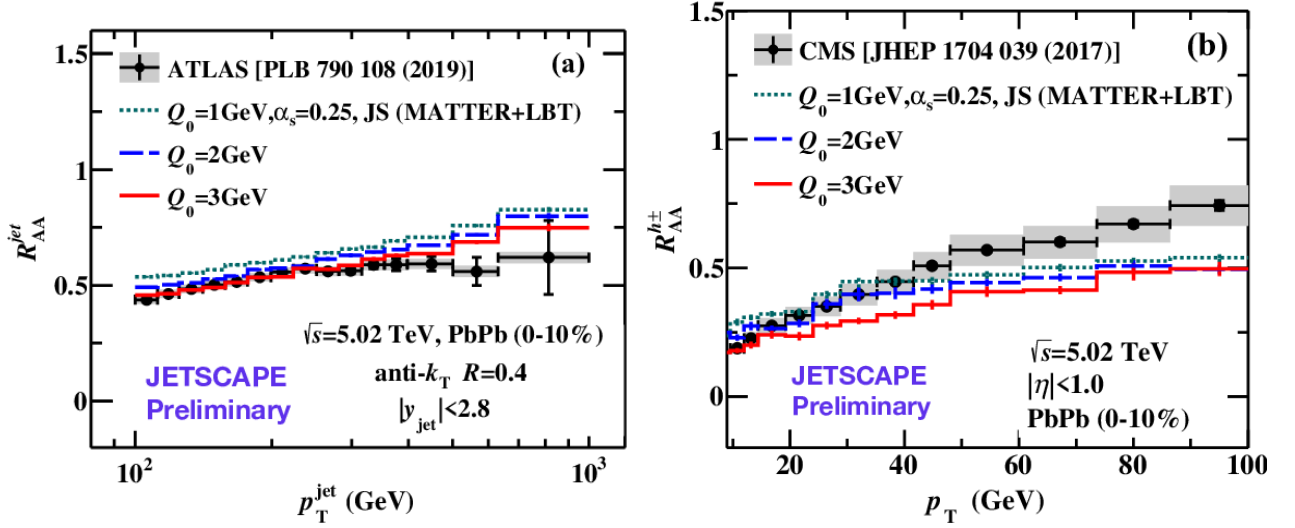


Figure 3.7: Nuclear modification factor for inclusive jets with cone size $R = 0.4$ (left) and charged hadrons (right). Data is from the ATLAS and CMS collaborations for $\sqrt{s} = 5.02$ TeV Pb-Pb collisions in the 0 – 10% centrality bin and it is compared to model calculations from the JETSCAPE collaboration. Figure reproduced from [106].

3.4.1 Nuclear modification factor (R_{AA})

The nuclear modification factor is the clearest signal of jet energy loss in a medium. It is defined as [105]

$$R_{AA}(p_T, y, \phi) = \frac{1}{\langle N_{coll.} \rangle} \frac{\frac{dN_{AA}}{dp_T dy d\phi}}{\frac{dN_{pp}}{dp_T dy d\phi}}. \quad (3.19)$$

R_{AA} is the ratio of multiplicity at nuclei-nuclei (A-A) collision to proton-proton (p-p) collision. $\langle N_{coll.} \rangle$ is the average number of binary collisions in a particular centrality class which can be estimated based on a model. The ratio can be taken for charged hadrons as a whole or specifically for identified jets inside a jet-cone of specified radius R . Radial distance in the jet-cone r is defined as

$$r = \sqrt{(\eta - \eta_{jet})^2 + (\phi - \phi_{jet})^2}. \quad (3.20)$$

Here, η_{jet} and ϕ_{jet} are the pseudorapidity and azimuthal angle of the jet-cone axis. Jet cone size R implies $r < R$.

Fig. 3.7 shows the R_{AA} as a function of p_T for both charged hadrons and inclusive jets. Notice that the value of R_{AA} is always less than 1, which is a consequence of quenching. Jets in the QGP are suppressed as compared to vacuum jets.

3.4.2 Jet shape function

Along with total energy loss, we can also measure the distribution of energy inside the jet cone. The jet shape function (ρ) is defined as [107]

$$\rho(r) = \frac{1}{\Delta r N_{jet}} \sum_{jet} \frac{p_T^{jet}(r - \Delta r/2, r + \Delta r/2)}{p_T^{jet}(0, R)}. \quad (3.21)$$

$p_T^{jet}(x, y)$ is the sum of all particle tracks in the jet cone with radial distance $x < r < y$. The averaging is over all the jets.

Those are the two ways of analyzing jets that are current, but we will focus on something different in this work. We will do the Mach cone analysis for jets which is related to these observables.

3.5 HEAVY QUARKS IN QGP

Heavy quark (charm and bottom) production in QGP is highly suppressed because of their large masses. As a result, most heavy quarks are produced at the early stages of the collision and propagate through the medium. Their typical decay times are usually larger than the lifetime of QGP. Consequentially, heavy flavor hadrons provide an additional probe into the QGP.

Similar to eq. (3.19), R_{AA} can be defined for D and B mesons. Comparative analysis of R_{AA} from heavy and light flavor hadrons can help us understand the flavor dependence of quenching in the QGP.

3.6 ELECTROMAGNETIC OBSERVABLES

Electromagnetic (EM) probes (photons and dileptons) provide a unique window into all stages of heavy-ion collisions. Once produced, EM probes only interact electromagnetically. Since α_{EM} is much smaller than the strong coupling α_s , EM probes escape to detectors without further interactions.

There are multiple sources of photon and dilepton emissions that cannot be differentiated in an experiment. Photons can be produced through hard parton interactions at the moment of collision (prompt photons), radiated from QGP and hadron gas or formed by parton or hadron scatterings (thermal photons), or formed from the decay of hadrons in the final stages of collisions (decay photons). Similar mechanisms exist for dilepton production as well. Photon and dilepton multiplicity and v_2 can be measured in experiments. They help constrain physics of all stages of HIC. We have described the mechanism of thermal photon production in section 2.4 and we will focus on just this mechanism in this work in part II.

3.7 SUMMARY

In this chapter we have described some of the observables measured in the HIC experiments, along the physical motivation in measuring them. Comparison between these measurements with the phenomenological calculations helps us characterize the properties of the QGP and constrain the QCD physics. These observables will be calculated in the framework described in chapter 2 in the remainder of this thesis.

OUTLINE OF THE REST OF THIS THESIS

In previous chapters, we have described the heavy-ion collision program, some of the important experimental observables that are measured in these experiments and phenomenological models that can be used to explain HIC data and extract physical insight.

Our goal in this thesis is to complete upon these models by adding real physical processes that have so far been largely overlooked. In the soft sector, we study thermal hydrodynamic fluctuations. In the hard sector, we study the medium response of parton jets. We also explore the effects of out of equilibrium QGP on heavy quark dynamics.

In part II of this thesis, we explore the phenomenological implications of thermal hydrodynamic fluctuations. Chapter 5 describes and motivates the study of thermal fluctuations and outlines the progress made so far. We also explain the challenges that have limited the development of a realistic hydrodynamic simulation with thermal fluctuations. In chapter 6 we build on a previously developed perturbative approach [1] to evaluate observables and ascertain whether a more realistic stochastic hydrodynamic simulation is warranted. We even extended this model to calculate the photon spectrum and anisotropy and obtained an interesting, albeit counterintuitive, result. With exciting and promising results, we move on to chapter 7 and develop the tools for realistic non-perturbative HIC simulation. We test and then use our new model to evaluate observables with shear fluctuations and identify those that are most susceptible to them. In chapter 8, we finally include bulk fluctuations. We also comment on the effects of large bulk viscosities and what it means for the validity of the hydrodynamic picture.

In part III we move on to hard processes that explore the perturbative regime of QGP. Chapter 9 explores the consequence of jet energy loss feedback on the medium. We examine if such a process can be used to independently constrain the viscosity of QGP. We also introduce our new concurrent jet-hydrodynamics framework. This new framework is now ready to explore the difficult intermediate p_T regime of HIC experiments.

Chapter 10 studies heavy-quark dynamics in QGP. We evaluated the viscous corrections to the collisional energy loss of heavy quarks. We also evaluated the drag and diffusion coefficients of heavy quarks in QGP, which is a fundamental transport property of the system.

In part IV we summarise and discuss our results.

Part II

THERMAL HYDRODYNAMIC FLUCTUATIONS

HYDRODYNAMIC FLUCTUATIONS IN HIC

Particle anisotropies measured in HIC are often considered to be signals of initial-state fluctuations (see section 3.3). However, thermal hydrodynamic fluctuations are another source of fluctuation that could lead to similar indistinguishable signatures in final state observables. These have largely been ignored in phenomenological simulations up to now and their effects therefore remain unassessed. One of the purposes of this work is to remedy this. In order to extract QGP properties from observables, all sources of fluctuations need to be accounted for in simulations. We have developed a mechanism to study thermal fluctuations.

5.1 LINEAR RESPONSE THEORY

Linear response theory describes the behaviour of a system perturbed slightly from equilibrium. Thermal fluctuations could be seen as small perturbations from a system's equilibrium and hence could be treated by the linear response theory. A detailed discussion can be found in standard textbooks like [108, 109]. We summarise the theory here.

Suppose a system with Hamiltonian \mathcal{H} at equilibrium feels an external perturbation. In the Heisenberg picture, one can express this as a small perturbation to the time-dependent Hamiltonian

$$\mathcal{H}'(t) = \mathcal{H}(t) + \delta\mathcal{H}(t), \quad (5.1)$$

where \mathcal{H}' is the new Hamiltonian and $\delta\mathcal{H}$ is the small external perturbation. The perturbation was switched on at time t_0 . The change in value of a field operator $\phi(\mathbf{x}, t)$ is governed by the Heisenberg equations of motion

$$\frac{\partial\phi(\mathbf{x}, t)}{\partial t} = i[\mathcal{H}'(t), \phi(\mathbf{x}, t)]. \quad (5.2)$$

If $|j\rangle$ forms a set of eigenstates for \mathcal{H} , we can write

$$\frac{\partial \langle j | \phi(\mathbf{x}, t) | j \rangle}{\partial t} = i \langle j | [\delta \mathcal{H}'(t), \phi(\mathbf{x}, t)] | j \rangle. \quad (5.3)$$

Since $\delta \mathcal{H}$ is only a small perturbation, up to first order we can get

$$\delta \langle j | \phi(\mathbf{x}, t) | j \rangle = i \int_{t_0}^t dt' \langle j | [\delta \mathcal{H}(t'), \phi(\mathbf{x}, t)] | j \rangle. \quad (5.4)$$

For a system in equilibrium, the expectation value of an operator can be given as

$$\langle \phi(\mathbf{x}, t) \rangle = \frac{1}{\mathcal{Z}} \sum_j e^{-\beta \mathcal{H}} \langle j | \phi(\mathbf{x}, t) | j \rangle, \quad (5.5)$$

where $\beta = 1/T$, T is temperature and $\mathcal{Z} = \sum_j e^{-\beta \mathcal{H}}$ is the partition function. So, we get

$$\delta \langle \phi(\mathbf{x}, t) \rangle = i \int_{t_0}^t dt' \text{Tr} \left\{ \frac{e^{-\beta \mathcal{H}}}{\mathcal{Z}} [\delta \mathcal{H}(t'), \phi(\mathbf{x}, t)] \right\}. \quad (5.6)$$

Now, a perturbation to the Hamiltonian could be considered as the coupling of an operator to an external field A . We can then write

$$\delta \mathcal{H}(t) = \int d^3 x \phi(\mathbf{x}, t) A(\mathbf{x}, t). \quad (5.7)$$

From eq. (5.6) and eq. (5.7), we can write

$$\delta \langle \phi(\mathbf{x}, t) \rangle = -i \int_{t_0}^t dt' \int d^3 x' A(\mathbf{x}', t') \text{Tr} \left\{ \frac{e^{-\beta \mathcal{H}}}{\mathcal{Z}} [\phi(\mathbf{x}, t), \phi(\mathbf{x}', t')] \right\}, \quad (5.8)$$

$$= \int_{-\infty}^{\infty} dt' \int d^3 x' A(\mathbf{x}', t') G_R(\mathbf{x}, t; \mathbf{x}', t'). \quad (5.9)$$

Here we have used the retarded Green's function G_R defined as

$$iG_R(\mathbf{x}, t; \mathbf{x}', t') \equiv \text{Tr} \left\{ \frac{e^{-\beta \mathcal{H}}}{\mathcal{Z}} [\phi(\mathbf{x}, t), \phi(\mathbf{x}', t')] \right\} \theta(t - t'). \quad (5.10)$$

$\theta(t - t')$ is the Heaviside step-function ensuring that G_R is non-zero only for $t > t'$. Consequently, we have changed the upper limit of integration to ∞ in eq. (5.9). The lower limit is taken to $-\infty$ as the external field A is turned on only at t_0 .

Since this is for a system in equilibrium, the Green's function depends only on the difference of coordinate values, allowing us to write

$$G^R(\mathbf{x} - \mathbf{x}', t - t') = \int \frac{d\omega d^3 k}{(2\pi)^4} e^{i[\mathbf{k} \cdot (\mathbf{x} - \mathbf{x}') - \omega(t - t')]} G^R(\omega, \mathbf{k}), \quad (5.11)$$

$$A(\mathbf{x}', t') = \int \frac{d\omega d^3 k}{(2\pi)^4} e^{i[\mathbf{k} \cdot \mathbf{x}' - \omega t']} A(\omega, \mathbf{k}). \quad (5.12)$$

This leads to a useful relation of linear response theory in momentum space

$$\delta\langle\phi(\omega, \mathbf{k})\rangle = A(\omega, \mathbf{k})G^R(\omega, \mathbf{k}). \quad (5.13)$$

For $t > t'$, we could also define the other Green's functions describing the system as

$$iG^>(\mathbf{x} - \mathbf{x}', t - t') = \langle\phi(\mathbf{x}, t)\phi(\mathbf{x}', t')\rangle = \text{Tr}\left\{\frac{e^{-\beta\mathcal{H}}}{\mathcal{Z}}\phi(\mathbf{x}, t), \phi(\mathbf{x}', t')\right\}, \quad (5.14)$$

$$iG^<(\mathbf{x} - \mathbf{x}', t - t') = \langle\phi(\mathbf{x}', t')\phi(\mathbf{x}, t)\rangle = \text{Tr}\left\{\frac{e^{-\beta\mathcal{H}}}{\mathcal{Z}}\phi(\mathbf{x}', t'), \phi(\mathbf{x}, t)\right\}. \quad (5.15)$$

In momentum space, the symmetrized Green's function is given as

$$G^S(\omega, \mathbf{k}) = G^>(\omega, \mathbf{k}) + G^<(\omega, \mathbf{k}). \quad (5.16)$$

Here $G^>(\omega, \mathbf{k})$ and $G^<(\omega, \mathbf{k})$ are Fourier transforms of the Green's functions defined in eq. (5.14) and eq. (5.15) respectively.

5.2 FLUCTUATION-DISSIPATION THEOREM

The generalized fluctuation-dissipation theorem can be stated as [110]

$$G^S(\omega, \mathbf{k}) = -2[n_B + 1]\text{Im}G^R(\omega, \mathbf{k}). \quad (5.17)$$

Here $n_B = (e^{\beta\omega} - 1)^{-1}$ is the Bose-Einstein distribution function. In the limit $\omega \rightarrow 0$ and $\mathbf{k} \rightarrow 0$, the fluctuation-dissipation theorems reduce to Kubo relations and are used to give statistical mechanic definitions of the dissipative transport coefficients [111].

The second law of thermodynamics states that a closed system will maximize its entropy. It was soon realized that this law is valid on the level of ensemble averages and individual systems may deviate from the maximal entropy condition. This was discovered for Brownian motion [112] and for electric field fluctuations [113] before being generalized as the fluctuation-dissipation theorem by Callen and Welton [110]. As illustrated in fig. 5.1, fluctuations take the system away from the maximal entropy condition while dissipation brings it back. At equilibrium they balance each other out.

Hydrodynamics is a macroscopic theory that is agnostic to the details of underlying interactions between the constituent particles of the fluid. The scale separation between

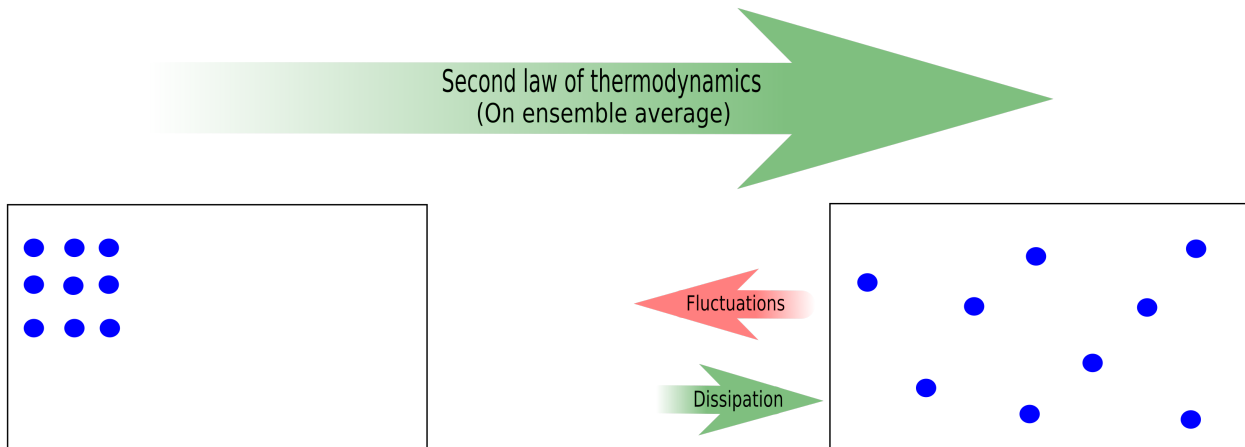


Figure 5.1: Illustration of the fluctuation-dissipation theorem for a closed system of gas molecules.

the microscopic interactions and the macroscopic behaviour of a system is a necessary condition for the applicability of hydrodynamics. This is usually quantified by the dimensionless Knudsen number defined in eq. (2.13). Consequently, hydrodynamics deals with locally averaged thermodynamic quantities like temperature, pressure, etc. These quantities could fluctuate about these average values on a mesoscopic scale. These fluctuations are called thermal hydrodynamic fluctuations and are described by the fluctuation-dissipation theorem.

Hydrodynamic fluctuations can be seen as a consequence of random microscopic fluxes. While hydrodynamics treats fluids as a continuum, they are composed of finite number of particle which interact with each other. Finite particle number effects cause a deviation from the continuum description. These deviations are the thermal fluctuations.

Studies of thermal hydrodynamic fluctuations, which are quantified by the fluctuation-dissipation theorem, use one of the two approaches: the deterministic approach and the stochastic approach. Both of these approaches have their strengths and challenges and they complement each other; this work focuses on the stochastic approach. But we begin by discussing the deterministic approach in the next section for completeness and context.

5.3 DETERMINISTIC TREATMENT OF THERMAL FLUCTUATIONS

Deterministic approaches typically rely on the separation of scales between the microscopic dynamics of the system, the mesoscopic scale of thermal fluctuations and the macroscopic scale of the long wavelength hydrodynamic modes. Off-equilibrium fluctuations are treated as additional slow modes and are evolved by deterministic partial differential equations coupled to the hydrodynamic equations. In the context of heavy-ion collisions, rapid progress has been made in this direction in the last few years. This has been motivated in part by the search for the critical point in the QCD phase diagram. We expect to see an enhancement in fluctuations near the critical point. A recent review of thermal fluctuations in this context is given here [114].

It has been long known that the thermal fluctuations in fluids give rise to fractional powers in the fluid response function at low frequencies (for example, see [115])

$$G^R \sim \omega^{3/2}. \quad (5.18)$$

This is formally more significant than the second order terms in hydrodynamics (order 1.5 vs order 2). As described in section 2.1.2, we use second order hydrodynamics for preserving causality. A consistent treatment of second order hydrodynamics therefore demands that order 1.5 terms coming from thermal fluctuations be included. This 3/2 response also gives rise to the parametrically slow decay of fluctuation modes. This is known as the "long-time tail". This has been shown in the context of relativistic hydrodynamics [116].

Hydro-kinetics is an approach that has recently become popular in the field [117–121]. In hydro-kinetics, a dissipative scale k_* is obtained. For frequency ω , k_* is given as

$$k_* = \left(\frac{\omega}{\gamma} \right)^{1/2}. \quad (5.19)$$

Here γ is the dissipative constant. For example, for shear viscosity, $\gamma = \gamma_\eta = \frac{\eta}{\varepsilon + P}$. Waves with wavenumbers $k \gg k_*$ are damped too fast compared to the timescale $2\pi/\omega$. Consequently, these waves are equilibrated. Waves with $k \sim k_*$ are of interest as they deviate away from equilibrium.

One can define equal-time two-point correlators of hydrodynamic fields $\phi(t, \mathbf{x})$ as

$$N_{ab}(t, \mathbf{x}, \mathbf{y}) = \langle \phi_a(t, \mathbf{x}) \phi_b(t, \mathbf{y}) \rangle. \quad (5.20)$$

The hydrodynamic equations are expanded up to linear order in thermal fluctuations with an added stochastic term. The two point correlator of the stochastic noise term is given by the fluctuation-dissipation theorem. These equations are written in momentum space where the time evolution equation for the Fourier transform of N_{ab} is derived. These evolution equations, coupled with the hydrodynamic equations, can now be evolved in a $3 + 3 + 1$ D space. At any time, we can get the two-point correlation function N_{ab} by solving these equations that gives us all the information about the thermal noise in the system.

Hydro-kinetic equations have been derived for a conformal fluid in static and Bjorken expanding medium [117], for a non-conformal fluid (one with non-zero bulk viscosity) in static and bulk expanding medium [118], for a Bjorken expanding conformal charged fluid [119], for a general flow [120] and for a general relativistic flow [121]. The detailed equations and their derivations can be seen in the appropriate references.

The Hydro+ approach combines the out of equilibrium fluctuations along with parameterically slow modes near the critical point [122]. Recently, numerical simulations of QGP near the critical point have been done, albeit in simplified models which do not capture all the physical effects [123, 124].

An approach analogous to hydro-kinetics is the "diagrammatic approach" that treats hydrodynamics as an effective field theory. In these theories, two-point correlators are represented as propagators. Recent progress in this direction can be found in [116, 125–130].

5.3.1 Renormalization of thermal noise

A universal feature of all deterministic approaches is their treatment of ultraviolet divergences. Hydro-kinetic equations invariably give divergent solutions for high wavenumbers. In the diagrammatic calculations, these could be seen as the effect of divergent loop diagrams. We also see this divergence problem in the stochastic method, where our approach to deal with this issue is explained in the subsequent chapters.

High wavenumber modes, being near equilibrium, have known analytic behaviour. In the analytic approach, a high wavenumber cutoff p_{cut} is introduced. These modes above

p_{cut} are absorbed in the hydrodynamic fields and transport coefficient in the equations such that the final results are cutoff independent.

This effectively brings corrections to the hydrodynamic quantities like energy density and pressure and on transport coefficients, e.g. shear and bulk viscosities. As the corrections to transport coefficients derived are inversely proportional to themselves, thermal fluctuations effectively place a minimum bound on transport coefficients. Lower bounds on the different transport coefficients have been derived for static as well as expanding fluids [116–119, 126].

5.3.2 *Strengths and Challenges*

The deterministic approach is computationally less demanding. As the numerical solution of the equations does not involve sampling random noise terms, a single solution run gives all the information about the fluctuations contained in the equation. On the other hand, the stochastic approach requires large statistics as we need to effectively cover the entire range of the distributions by our sampling of the random terms.

The major challenge of the deterministic approach is that it is very difficult to obtain n -point correlators from it for $n > 2$. In the stochastic method, fluctuations evolve dynamically through the non-linear hydrodynamic equations and, in principle, any n -point correlator can be evaluated. This is crucial for studying critical fluctuations near the QCD critical point as the signals of these fluctuations will arise in the skewness and kurtosis of the particle multiplicities. Skewness and kurtosis are respectively signatures of the three and four point correlators. There is no way of evaluating these in the most current deterministic theories. A recent work gives a theory for deterministic evaluation of the n -point correlators [131]. However, this theory has only been written to tree-diagram level and it is not obvious how to remove divergences from this theory. Though this theory presents an important development towards the solution of a long-standing problem, it remains to be tested if this theory produces cutoff independent results.

Another difficulty of using the deterministic approach is the complication of the equations. This involves solving for many variables in a $3 + 3 + 1$ dimensional space. Because

of the associated difficulties, the numerical simulations using the Hydro+ evolution of only the two-point correlators has been limited to simplified flows [123, 124]

5.4 STOCHASTIC TREATMENT OF THERMAL FLUCTUATIONS

In hydrodynamics, thermal fluctuations can be treated by adding a stochastic component ($S^{\mu\nu}$) to the energy-momentum tensor as given in eq. (2.7) [132].

$$T^{\mu\nu} = T_{\text{id.}}^{\mu\nu} + T_{\text{vis.}}^{\mu\nu} + S^{\mu\nu}. \quad (5.21)$$

$S^{\mu\nu}$ is a random fluctuating term. Consequently, the energy-momentum conservation equation ($\partial_\nu T^{\mu\nu} = 0$) is modified from a partial-differential equation (PDE) to a stochastic partial-differential equation (SPDE). This cannot be simply solved by ordinary Riemann integrals. Unlike ordinary PDEs, SPDEs take distributions as boundary conditions and have distributions as solutions. We need to use the Stratonovich definitions of the integrals [64]. MUSIC uses Heun's method (see section 2.1.2.2) for temporal evolution, which is consistent with Stratonovich integrals. For details on various definitions of stochastic integrals, see [133].

The system of equations are closed by the fluctuation-dissipation theorem. For relativistic fluids following the first order Navier-Stokes hydrodynamics, this can be represented by two-point correlation functions [132]

$$\langle S^{\mu\nu}(x_1) S^{\rho\sigma}(x_2) \rangle = 2T \left[\eta (\Delta^{\mu\rho} \Delta^{\nu\sigma} + \Delta^{\mu\sigma} \Delta^{\nu\rho}) + \left(\zeta - \frac{2}{3} \eta \right) \Delta^{\mu\nu} \Delta^{\rho\sigma} \right] \delta^4(x_1 - x_2). \quad (5.22)$$

Here x_1 and x_2 are space-time four-vectors. The noise correlation, as characterized by a four-delta function, is called white noise. In this form, noise at any point in space-time is uncorrelated to noise at any other point in space-time.

Equation 5.22 can be seen as the hydrodynamic limit of eq. (5.17). Hydrodynamics can be written as an effective field theory where the retarded and the symmetrized Green's functions can be evaluated. The fluctuation-dissipation theorem reduces to eq. (5.22) for Navier-Stokes hydrodynamics. For a pedagogical discussion on this, see [134]. Alternatively, eq. (5.22) can be derived directly by considering the response of hydrodynamic variables to random fluctuations. This can be seen for the non-relativistic fluids in [135] and for relativistic fluids in [132].

In causal hydrodynamics, a fluctuation cannot decay instantaneously, i.e. the noise cannot be white in the temporal direction. For Muller-Israel-Stewart hydrodynamics, the noise term is evolved by a differential equation with a relaxation time built in. The noise term can be further divided into the term associated with the shear dissipation (S_π) and the term associated with bulk dissipation ($S_\Pi^{\mu\nu}$).

$$S^{\mu\nu} = S_\pi^{\mu\nu} + S_\Pi \Delta^{\mu\nu} \quad (5.23)$$

Similar to eqs. (2.10) and (2.11), their evolution equation can be given as

$$\Delta_\alpha^\mu \Delta_\beta^\nu (u \cdot \partial) S_\pi^{\alpha\beta} = -\frac{1}{\tau_\pi} (S_\pi^{\mu\nu} - \zeta^{\mu\nu}) - \frac{4}{3} S_\pi^{\mu\nu} \theta, \quad (5.24)$$

and

$$(u \cdot \partial) S_\Pi = -\frac{1}{\tau_\Pi} (S_\Pi - \Xi) - \frac{2}{3} S_\Pi \theta. \quad (5.25)$$

Here $\zeta^{\mu\nu}$ and Ξ are random stochastic terms determined by the fluctuation-dissipation theorems

$$\langle \zeta^{\mu\nu}(x_1) \zeta^{\rho\sigma}(x_2) \rangle = 2T\eta \left[\Delta^{\mu\rho} \Delta^{\nu\sigma} + \Delta^{\mu\sigma} \Delta^{\nu\rho} + -\frac{2}{3} \Delta^{\mu\nu} \Delta^{\rho\sigma} \right] \delta^4(x_1 - x_2), \quad (5.26)$$

and

$$\langle \Xi(x_1) \Xi(x_2) \rangle = 2T\zeta \delta^4(x_1 - x_2). \quad (5.27)$$

The derivation of stochastic second-order causal hydrodynamics can be found in [64, 136–139]

The stochastic treatment entails numerically solving the set of SPDEs. The equations are typically solved on a grid and the noise terms ($\zeta^{\mu\nu}, \Xi$) are randomly sampled from a distribution with variances given by eqs. (5.26, 5.27). Each possible series of noise term samplings give rise to a possible sample path. To obtain a statistically significant solution of the equations, a large number of sample paths are required. We go into more details of the stochastic treatment in subsequent chapters.

Naively, once we have the energy momentum equations in hand, along with the equations for the stochastic term (eqs. (5.21) and (5.23) to (5.27)), we just need to use a suitable numerical algorithm to solve these equations. However, there are certain challenges that we run into once we get to solving these equations.

5.5 CHALLENGES IN STOCHASTIC TREATMENT OF FLUCTUATIONS

5.5.1 Arbitrarily large gradients

The primary difficulty lies with the nature of the fluctuation term. The fluctuation-dissipation theorem eqs. (5.26) and (5.27) describes what is known as *white noise*. The delta functions in the two point correlation functions dictate that the fluctuation at a point in space is un-correlated to fluctuations at any other point.

In numerical hydrodynamics, the natural choice to replace a continuous delta-function would be the discrete Kronecker-delta divided by the inverse space-time volume of a cell

$$\delta^4(x_1 - x_2) \rightarrow \frac{1}{\Delta V \Delta t} \delta_{1,2}^4. \quad (5.28)$$

ΔV is the spatial volume of a fluid cell and Δt is the size of a time step. In discretized hydrodynamics, the Kronecker-delta ensures that the stochastic-term sampled in a space-time cell is uncorrelated to the stochastic term in any other space-time cell. This essentially means that stochastic terms could be sampled independently in different cells from a given distribution.

While independent samplings are technically easier to do, this method leads to an obvious difficulty. Now, the strength of the stochastic term is inversely proportional to the cell volume. Discretized hydrodynamics approaches continuum hydrodynamics in the limit $\Delta V \rightarrow 0$ and $\Delta t \rightarrow 0$. To incorporate higher and higher wavenumber modes in our calculation, we would need to go to lower and lower cell size. However, in this situation, lower cell sizes imply a larger stochastic term. Also, the stochastic contribution in any one cell is uncorrelated to any other cell. This leads to arbitrarily large gradients.

All PDE solvers assume a smooth slowly varying function to some degree and no algorithm can deal with arbitrarily large gradients, especially when that gradient is between every pair of neighboring cells. Eventually, numerical hydrodynamics breaks down.

These large gradients are illustrated in fig. 5.2. In addition to algorithm failure, large gradients create another issue. As we can notice in fig. 5.2, some cells have negative energy densities. This happens when we use small cell sizes and fluctuations become large.

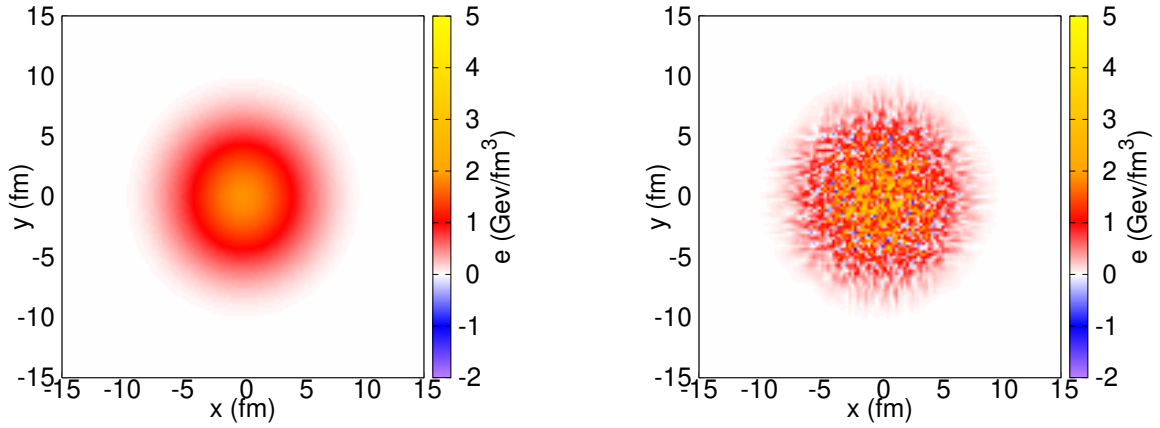


Figure 5.2: Typical energy density profiles for hydrodynamic evolution without (left) and with (right) thermal fluctuations.

Now fluctuations, by their very nature, could be both positive and negative. Sometimes fluctuations in local energy density could be larger than the local energy density itself and also be negative. This leads to net negative energy density, which is obviously unphysical. The equation of state is undefined for these points and the whole calculation breaks down.

As we have discussed above, these technical difficulties are a consequence of the discretization of delta-functions locally at each space-time cell. Delta function source terms appear in many situations in physics in general and in fluid dynamics in particular. The most common method to avoid these problems is by smearing the delta-functions. A delta function can be replaced by some Gaussian function (instead of discrete Kronecker-deltas, as we have done). This technique has been used in later parts of this thesis for dealing with energy depositions from jets. However, what makes this problem unique is that, in this case, these stochastic source terms are present throughout the space-time evolution. Any naive arbitrary smearing procedure may introduce artificial long-range correlations. These correlations will be indistinguishable from the physical long range correlations introduced by the evolution of the fluctuation terms. Consequently, we will not be able to separate the clear signal of thermal fluctuations from spurious smearing effects.

Another way around this quandary may be to use a more realistic theory having *colored fluctuations*. That will surely give us a physical correlation length and get us around this

arbitrary smearing width problem. In the next section, we make the case for white noise and argue why we think that even if there is a theory of colored noise, it may not help our situation.

Stochastic hydrodynamic simulations have been performed for simplified flows [132, 140], for the diffusion equation [141–145] and using a smearing mechanism [146, 147]. Our goal is to develop a consistent method of solving stochastic hydrodynamics in realistic simulations of QGP.

5.5.2 Argument for white noise

In any real physical fluid, local fluctuations at the mesoscopic level arise due to random fluxes at the microscopic level. Consequently, a more sophisticated theory of thermal fluctuations would describe a spatially correlated noise or *colored noise*.

However, a back of the envelope calculation shows that white noise is adequate for our purposes. The relaxation time is a good approximation for the correlation length of thermal fluctuations. A fluctuation would decay in a time on the order of the relaxation time. Because of causality, that is the maximum length it could travel. For heavy-ion collisions, the peak temperatures (where the fluctuations are highest) can be higher than 0.5 GeV. The shear viscosity over entropy density value is of the order 0.1. From eq. (2.17), this will lead to shear relaxation time of $\tau_\pi = \frac{5\eta}{(\varepsilon + P)} = \frac{5\eta}{Ts} \approx 5 * 0.1 / 0.5 \text{ GeV}^{-1} = 1 \text{ GeV}^{-1} \approx 0.2 \text{ fm}$. This is of the order of the cell width used in a typical heavy-ion collision simulation.

Numerical hydrodynamics relies on the choice of cell widths to be much smaller than the scale of physics being explored. Strictly speaking, simulations cannot resolve any mode with wavelength smaller than $2x$ where x is the cell dimension. However, for the reasonable convergence of solutions, the wavelength of the mode being studied should be much larger than $2x$.

This shows that even if we had a good theory of colored fluctuations, we would not be able to resolve it in our simulations, at least not with existing resources. As a rough estimate, it would require us to divide each cell in ten parts to be able to reasonably resolve a theory of colored noise. This is ten parts in each spatial direction which translates to

an increment of order 1000 times in number of grid cells. On top of that convergence requirements dictated by the CFL (Courant-Friedrichs–Lewy) condition [148] would require the time step size to be reduced by a factor of 10. This would amount to an increase in the computational resource requirement by four orders of magnitude.

Even if we were to explore the system at those scales, we would not necessarily gain much insight as most observables that we observe in experiments are not really sensitive to that scale. What we are interested in is the contribution of thermal fluctuations at the scales that we are currently exploring in heavy ion collisions.

For that purpose, the theory of white noise is adequate. The requirement is to properly sum over the very short length scale modes and have a theory of fluctuations at the scale we are interested in.

5.6 SUMMARY

In this chapter we have discussed the theory of thermal fluctuations and how it applies to relativistic fluid dynamics for HIC. In sections 5.1 and 5.2, we described the linear response theory and the general fluctuation-dissipation theorem respectively. The deterministic approach of treating thermal hydrodynamic fluctuations in HIC is summarized in section 5.3 along with its advantages and limitations.

The stochastic approach is introduced in section 5.4. In section 5.5, we explain the challenges that have so far hindered the inclusion of thermal hydrodynamic fluctuations in realistic simulations of HIC. In the rest of the chapters in this part of the thesis, we develop a mechanism to overcome these challenges and do realistic simulations including thermal fluctuations. We will evaluate the experimental observables and estimate the effects of these fluctuations.

FLUCTUATIONS AS PERTURBATION

One way to sidestep some of the challenges of the stochastic method is to treat thermal fluctuations as perturbations on top of the background fluid evolution [1]. This method was extended in this work. In this chapter, we have neglected the contribution of bulk viscosity (and associated fluctuations) and focus on the effects of shear fluctuation-dissipation theorem.

6.1 PERTURBATIVE STOCHASTIC HYDRODYNAMICS

The conventional non-fluctuating hydrodynamics can be treated as an ensemble averaged version of fluctuating hydrodynamics. All independent hydrodynamic variables can be expanded around their ensemble averaged values.

A fluctuating correction is associated with every hydrodynamic variable and all the equations are expanded up to linear order in these fluctuations. In this chapter, we denote the averaged non-fluctuating quantities with a subscript 0 and the fluctuations with a δ . Consequently, we have energy density $\varepsilon = \varepsilon_0 + \delta\varepsilon$, pressure $P = P_0 + \delta P$, flow velocity $u^\mu = u_0^\mu + \delta u_0^\mu$ and shear viscous tensor $\pi^{\mu\nu} = \pi_0^{\mu\nu} + \delta\pi^{\mu\nu}$. Ideal part of the energy-momentum tensor can also be separated into an average and a fluctuating contribution.

$$T_{\text{id.}}^{\mu\nu} = T_{\text{id.}0}^{\mu\nu} + \delta T_{\text{id.}}^{\mu\nu}, \quad (6.1)$$

$$\implies T_{\text{id.}0}^{\mu\nu} + \delta T_{\text{id.}}^{\mu\nu} = [(\varepsilon_0 + \delta\varepsilon + P_0 + \delta P)(u_0^\mu + \delta u_0^\mu)(u_0^\nu + \delta u_0^\nu) - (P_0 + \delta P)g^{\mu\nu}], \quad (6.2)$$

$$\implies \delta T_{\text{id.}}^{\mu\nu} = (\delta\varepsilon + \delta P)u_0^\mu u_0^\nu + (\varepsilon_0 + P_0)(u_0^\mu \delta u_0^\nu + \delta u_0^\mu u_0^\nu) - \delta P g^{\mu\nu}. \quad (6.3)$$

As usual, the full hydrodynamic equations are

$$\partial_\nu T^{\mu\nu} = \partial_\nu (T_{\text{id.}0}^{\mu\nu} + \delta T_{\text{id.}}^{\mu\nu} + \pi_0^{\mu\nu} + \delta\pi^{\mu\nu} + S_\pi^{\mu\nu}) = 0. \quad (6.4)$$

Also, the equations for averaged quantities also hold

$$\partial_\nu (T_{\text{id},0}^{\mu\nu} + \pi_0^{\mu\nu}) = 0, \quad (6.5)$$

which gives us the equations for the fluctuating quantities

$$\partial_\nu (\delta T_{\text{id}}^{\mu\nu} + \delta\pi^{\mu\nu} + S_\pi^{\mu\nu}) = 0 \quad (6.6)$$

Equation for $\delta\pi^{\mu\nu}$ can be derived by starting from the equation for $\pi^{\mu\nu}$ and taking fluctuations to all quantities up to linear order

$$\delta[\Delta_\alpha^\mu \Delta_\beta^\nu (u \cdot \partial) \pi^{\alpha\beta}] = -\frac{1}{\tau_\pi} (\delta\pi^{\mu\nu} - \delta\sigma^{\mu\nu}) - \frac{4}{3} \delta[\pi^{\mu\nu} \theta] \quad (6.7)$$

Further, we need to satisfy the condition of the shear term being transverse to u^μ to all orders. So, using $u_{\mu 0} \pi_0^{\mu\nu} = 0$, up to linear order, we get

$$(u_{\mu 0} + \delta u_\mu) (\pi_0^{\mu\nu} + \delta\pi^{\mu\nu}) = 0, \quad (6.8)$$

$$\implies u_{\mu 0} \delta\pi^{\mu\nu} + \delta u_\mu \pi_0^{\mu\nu} = 0. \quad (6.9)$$

Using eq. (6.7) along with eq. (6.9), we get the evolution equation for $\delta\pi^{\mu\nu}$. The details of the derivation can be seen in [1]. Here we quote the final equation

$$\begin{aligned} (u_0 \cdot \partial) \delta\pi'^{\mu\nu} = & -\frac{1}{\tau_\pi} [\delta\pi'^{\mu\nu} - \delta\sigma^{\mu\nu} - \xi^{\mu\nu}] - \frac{4}{3} (\partial \cdot \delta u) \pi_0^{\mu\nu} - \frac{4}{3} (\partial \cdot u_{u_0}) \delta\pi'^{\mu\nu} \\ & - \delta u^\mu ((u_0 \cdot \partial) u_{0\alpha}) \pi_0^{\alpha\nu} - u_0^\mu ((\delta u \cdot \partial) u_{0\alpha}) \pi_0^{\alpha\nu} \\ & + u_0^\mu ((u_0 \cdot \partial) \delta u_\alpha) \pi_0^{\alpha\nu} - u_0^\mu ((u_0 \cdot \partial) u_{0\alpha}) \delta\pi'^{\alpha\nu} \\ & - \delta u^\nu ((u_0 \cdot \partial) u_{0\alpha}) \pi_0^{\alpha\mu} - u_0^\nu ((\delta u \cdot \partial) u_{0\alpha}) \pi_0^{\alpha\mu} \\ & + u_0^\nu ((u_0 \cdot \partial) \delta u_\alpha) \pi_0^{\alpha\mu} - u_0^\nu ((u_0 \cdot \partial) u_{0\alpha}) \delta\pi'^{\alpha\mu} \\ & - (\delta u \cdot \partial) \pi_0^{\mu\nu}. \end{aligned} \quad (6.10)$$

Here we have defined $\delta\pi'^{\mu\nu} = \delta\pi^{\mu\nu} + S_\pi^{\mu\nu}$. $\delta\sigma^{\mu\nu}$ is the fluctuation in Navier-Stokes tensor (see section 2.1.2). $\xi^{\mu\nu}$ is a random source term with its autocorrelation given by eq. (5.26).

6.2 HYDRODYNAMIC SIMULATIONS

MUSIC was used to solve the equations for perturbative fluctuations on top of the averaged quantities. MUSIC used the Kurganov-Tadmor method for solving the averaged

quantities. Fluctuating quantities were solved at each time step using the simpler McCormack method [149]. At each time-step, after solving for averaged quantities using MUSIC, fluctuating quantities were solved for as follows

1. We use eq. (5.26) to evaluate the fluctuating source term $\zeta^{\mu\nu}$ at each time step in each cell. $\zeta^{\mu\nu}$ is sampled in the local rest frame and then boosted to the lab frame. In the local rest frame $\zeta^{0\nu} = 0$ and eq. (5.26) reduces to

$$\langle \zeta^{ij}(x_1) \zeta^{kl}(x_2) \rangle = 2T\eta \left[\delta^{ik} \delta^{jl} + \delta^{il} \delta^{jk} + -\frac{2}{3} \delta^{ij} \delta^{kl} \right] \delta^4(x_1 - x_2) \quad (6.11)$$

Independent components of $\zeta^{\mu\nu}$ are sampled from Gaussian random numbers with the width of the distribution given by the root of the two-point correlators given in eq. (6.11). The central limit theorem justifies our use of Gaussian random numbers.

2. We used eq. (6.10) to get $\delta\pi^{\mu\nu} + S_\pi^{\mu\nu}$ at the next time step.
3. $\delta T_{\text{id}}^{\mu 0}$ at the next time step is determined using $\partial_0 \delta T_{\text{id}}^{\mu 0} = -\partial_i \delta T_{\text{id}}^{\mu i} - \partial_\nu \delta\pi^{\mu\nu} - \partial_\nu S_\pi^{\mu\nu}$.
4. δu^μ , $\delta\varepsilon$ and δP are evaluated using a root-finding algorithm and eq. (6.3)

The perturbative stochastic hydrodynamic equations need initial conditions to evolve. For this study, we have used the smooth optical Glauber model [37, 38] to initialize MUSIC. Optical Glauber conditions simulate the energy distribution at the beginning of a heavy-ion collision at a given impact parameter by assuming that the overlap area after the collision contains energy proportional to the amount of nuclear matter passing through it. Distribution of nuclear matter in an uncollided nucleus follows smooth Woods-Saxon distribution. For details, see section 2.1.1.

Optical Glauber model gives simplistic initial conditions which crucially miss the initial state fluctuations. The motivation at this stage of the study is to get an intuition into the effects of thermal fluctuations rather than doing a realistic quantitative estimation of experimental observables. To this effect, the optical Glauber model serves our purpose while avoiding the complications of added sources of fluctuations. This simplistic model also helps us side-step some of the issues described in section 5.5. Hydrodynamic evolution begins at proper time $\tau = 0.4$ fm. This proper time was chosen to match the spectrum and flow data.

Furthermore, we need an equation of state to close the system of equations. We have used the lattice-QCD motivated s95p parameterization of the equation of state [150]. We simulated 600 fluctuating events and shear viscosity to entropy density was set to 0.08. This choice of viscosity is motivated by early phenomenological studies [32, 151, 152] as well as the lower bound of $1/4\pi$ for shear viscosity to entropy density ratio predicted using string theory methods [153].

6.3 MOMENTUM ECCENTRICITIES

As the system evolves in this perturbative approach, all hydrodynamic quantities fluctuate about the average values. We are interested in the effects of fluctuations averaged over a large number of events. Thermal fluctuations could be both positive and negative and cancel over large number of samplings. Consequently, we would not see any effect on the total energy. This is also guaranteed by energy conservation, which the stochastic hydrodynamics respects over ensemble averages.

The effects of fluctuations are visible over quantities which are dependent on the higher order products of the fluctuating quantities. One of the crucial signatures of collective behavior is the eccentricity (v_2) in the observed particles. Momentum eccentricity ϵ_p serves as a good proxy for the particle eccentricity during the hydrodynamic evolution. Like v_2 , ϵ_p is a measure of the difference in momentum between the x and y directions. It is defined as

$$\epsilon_p = \sqrt{\frac{\langle T_{xx} - T_{yy} \rangle^2 + \langle 2T_{xy} \rangle^2}{\langle T_{xx} + T_{yy} \rangle^2}} \quad (6.12)$$

For non-zero impact parameters, even smooth events have non-zero momentum eccentricities. The imbalance in x and y directions come from the almond shape of the initial energy distribution (see fig. 3.5). Adding fluctuations on top of this initial almond shape further changes these eccentricities. Evolution of ϵ_p averaged over 600 Au-Au collision events at $\sqrt{s} = 200$ GeV is shown in fig. 6.1. Here the impact parameter is 3 fm which corresponds to 0 – 5% centrality bin.

Both the averaged fluctuating and non-fluctuating curves in fig. 6.1, start at 0 eccentricity as there is no flow at the beginning. They diverge quickly as the fluctuations build

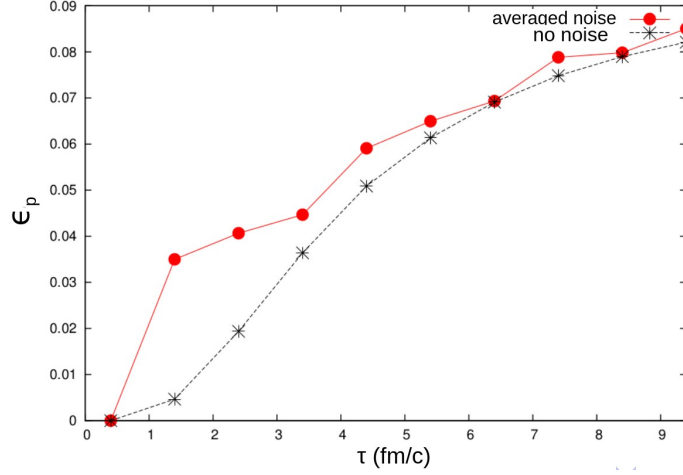


Figure 6.1: Evolution of momentum eccentricity as a function of proper time with and without thermal noise. This is averaged over 600 noisy events for Au-Au collision system at $\sqrt{s} = 200$ GeV with impact parameter 3 fm.

flow pretty rapidly. Fluctuations are large at large temperature, so the fluctuation sizes are also big initially, when the temperatures are higher. This contributes to development of large flow at early times in fluctuating systems. Eventually, flow also develops in the non-fluctuating system and the effect of noise is not as dramatic.

6.4 HADRONIC OBSERVABLES

As described in the first part part of this thesis, hydrodynamic isothermal surfaces can be converted to hadrons using the Cooper-Frye prescriptions. This requires particle distribution functions for the hadrons which ensure the continuity of energy momentum across the surface between hydrodynamics and kinetic theory (see section 2.1.3).

When hydrodynamics deviates from equilibrium, the particle densities used in the Cooper-Frye distribution also need to have proper corrections. Here we have shear-viscous and shear-fluctuation deviations from equilibrium. Consequently, there are viscous and fluctuation corrections to the equilibrium particle distribution functions (f_0) [1]

$$f(p) = f_0 + f_0(1 \pm f_0)\pi_{0\mu\nu}\frac{p^\mu p^\nu}{2(e_0 + P_0)T_0^2} + \delta f. \quad (6.13)$$

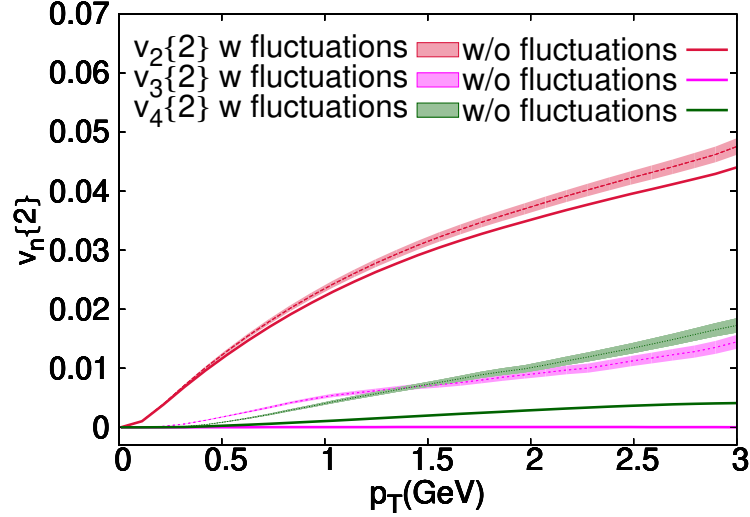


Figure 6.2: Differential v_n for zero impact Au-Au collisions at $\sqrt{s} = 200$ GeV. Bands denote statistical error bars.

Here p is the momentum of the particle. The sign \pm is $+$ for bosons and $-$ for fermions. Second term is the viscous correction derived using Grad's 14 moment method and given in eq. (2.34), while δf denotes the fluctuation correction. We can evaluate δf by Taylor expanding equilibrium and shear terms in eq. (6.13) up to linear order in fluctuations. So we get

$$\begin{aligned} \delta f = & \delta f_0 + \delta f_0(1 \pm 2f_0)\pi_{0\mu\nu}\frac{p^\mu p^\nu}{2(e_0 + P_0)T_0^2} + f_0(1 \pm f_0)\delta\pi'_{\mu\nu}\frac{p^\mu p^\nu}{2(e_0 + P_0)T_0^2} \\ & + f_0(1 \pm f_0)\pi_{0\mu\nu}\frac{p^\mu p^\nu}{2(e_0 + P_0)T_0^2} \left(-\frac{\delta e + \delta P}{e_0 + P_0} - 2\frac{\delta T}{T_0} \right). \end{aligned} \quad (6.14)$$

Here $\delta\pi'^{\mu\nu} = \delta\pi^{\mu\nu} + S_\pi^{\mu\nu}$. δf_0 is the fluctuation correction to the equilibrium term in the eq. (6.13) and is given as

$$\delta f_0 = -\frac{\exp(p \cdot u/T_0)}{[\exp(p \cdot u/T_0) \pm 1]^2} \left(\frac{\delta u \cdot p}{T_0} - (p \cdot u)\frac{\delta T}{T_0^2} \right) \quad (6.15)$$

In the last equation sign \pm is $+$ for fermions and is $-$ for bosons.

We evaluated the hadronic observables described in section 3.3. As total energy is conserved, particle multiplicities are not affected.

Differential v_n is shown in fig. 6.2. One sees that v_2 increases marginally with fluctuations. Naively, the effect looks more pronounced on v_3 and v_4 . However, that is because fluctuations are the only source of triangularity (v_3) and predominant source of quadruplicity (v_4) in heavy-ion collisions. As we have no initial state fluctuations, without

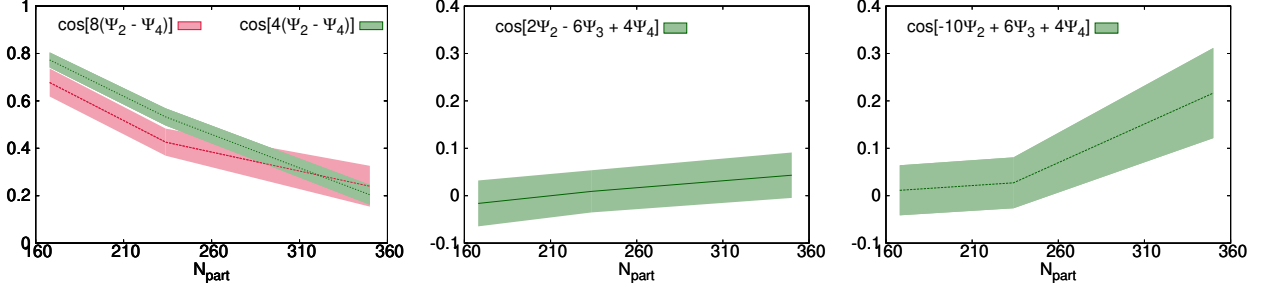


Figure 6.3: Hadronic event plane correlators defined in section 3.3.2 for Au-Au collisions at $\sqrt{s} = 200$ GeV. Bands denote statistical uncertainties.

thermal noise, these quantities are very low. v_2 is primarily contributed by the initial almond shape of energy distribution, hence, it is present even in the absence of thermal noise.

To further get intuition into the possible signals of thermal fluctuations, we looked at other observables. Interestingly, we observe significant effects on the event-plane correlators. As described in section 3.3.2, event-plane correlators measure the correlations between the planes of different v_n . As such, they are very susceptible to fluctuations, thermal or otherwise. We simulated 300 fluctuating events per 10% centrality from 0 – 50% centrality bins using smooth optical Glauber initial conditions. Appropriate impact parameters for different centrality bins were taken from [154]. Fig. 6.3 shows some of the event-plane correlators. In absence of any fluctuations, all event-planes should be perfectly correlated and the value of all these event-plane correlators will be identically 1.0. In presence of thermal fluctuations, both 2-plane and 3-plane correlators deviate significantly from that state. Should there be no other source of fluctuations, a measurement of these correlators deviating from 1 would be a “smoking gun” signal of thermal fluctuations. A more realistic study is performed later in this work.

6.5 PHOTONIC OBSERVABLES

As we observed in fig. 6.1, momentum eccentricities for fluctuating events deviated significantly from the non-fluctuating events early in the evolution. As we discussed in

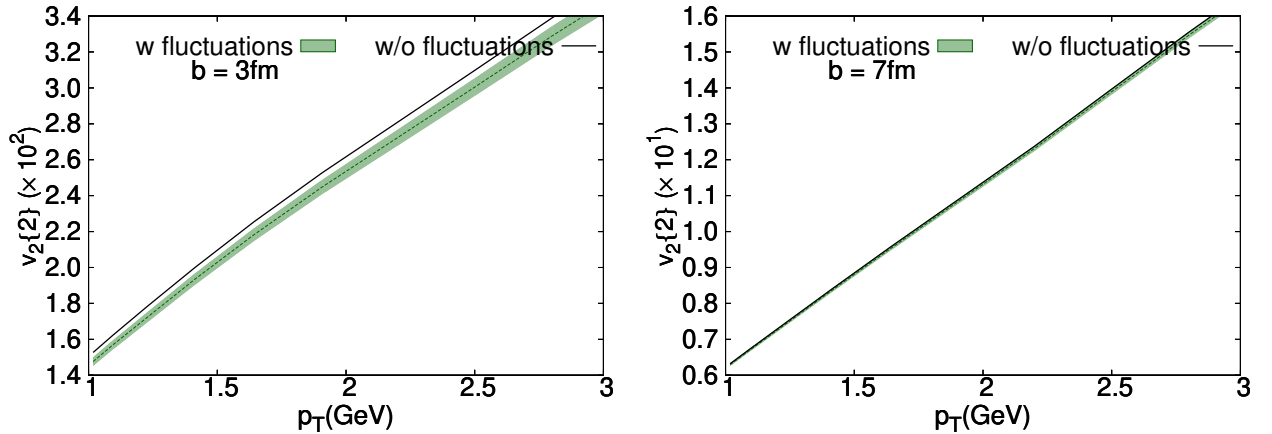


Figure 6.4: Thermal photon v_2 for fluctuating and non-fluctuating events with impact parameters 3 fm (left) and 7 fm (right). Bands denote statistical error bars.

section 3.6, electromagnetic observables provide us a window into all the stages of QGP evolution. As such, we expect that enhanced ϵ_p to leave its impact on photon v_2 .

There is a puzzle in the field known as the photon v_2 puzzle. Photon v_2 evaluated in the theoretical calculations [71] under-predict the values observed at the experiment [155]. Since thermal fluctuations enhance overall hadron v_2 (see fig. 6.2), one might expect it to narrow the difference observed in the photon v_2 puzzle.

With this motivation, we evaluated the photon v_2 for thermally fluctuating events and compared them to non-fluctuating events. We added the fluctuation contributions to $2 \rightarrow 2$ photon production channels in the meson gas and QGP phases [156]. We used the small momentum exchange forward scattering approximation in QGP phase [90] (see section 2.4). The fluctuation correction in the distribution functions of these channels is incorporated using eqs. (6.13) to (6.15). Photon v_2 , once evaluated is correlated with the charged hadron v_2 event-by-event using the scalar product method described in section 3.3.1.1. This is done to mimic experimental procedure.

Fig. 6.4 shows photon v_2 for two different impact parameters. Contrary to naive expectations, thermal fluctuations end up reducing photon v_2 . It is interesting to investigate the reasons for this counterintuitive behaviour. The clue lies in the large event plane decorrelations observed in fig. 6.3.

Even though thermal fluctuations increase ϵ_p and consequently photon v_2 in individual events, this increase is completely uncorrelated to the charged hadron v_2 of the

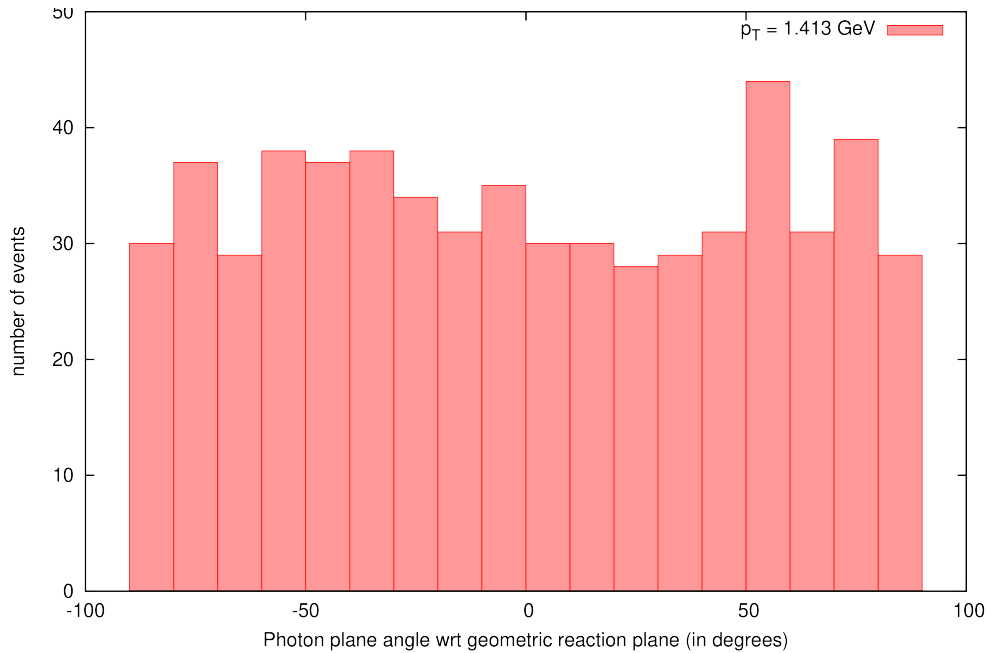


Figure 6.5: Distribution of photon v_2 event planes at $p_T = 1.413$ GeV for fluctuating events with impact parameter 3 fm.

underlying event. Consequently, when we evaluate the projection of photon v_2 on the charged hadron v_2 , we end up reducing the overall v_2 . This procedure is essential as it is done in experiments. Because of low photon statistics in heavy-ion collisions, all photon v_n measurements rely on the correlation with charged hadron v_n [155, 157].

This hypothesis is easy to verify. Fig. 6.5 shows the distribution of photon v_2 event planes between ± 90 degrees for one transverse momentum for fluctuating events with impact parameter 3 fm. Charged hadron event plane is predominantly determined by the initial almond shape energy distribution and lies along the minor-axis of the ellipse. However, as we can see in fig. 6.5, photon event planes are almost evenly distributed across the semi-circle. This ensures a low projection of photon v_2 on the charged hadron v_2 event plane.

6.6 SUMMARY

The motivation of this chapter was to explore the observable space to find if and where can one expect to see the signals of thermal fluctuations. We observed, in simple settings, that event-plane correlators are very sensitive to thermal fluctuations. We also observed

that thermal fluctuations have a small effect of decreasing the photon v_2 because of large anti-correlations between the photon and charged-hadron planes.

This provides us the motivation to do more realistic studies with fluctuating initial conditions and non-perturbative solution of stochastic equations. As noted in the beginning of this chapter, this perturbative method only sidesteps the difficulties described in section 5.5. Some of these difficulties reappear when we try to use small cells or when we use fluctuating initial conditions, even with the perturbative method. We need more robust methods for non-perturbative treatment which is the subject matter for the next chapter.

We focus on hadronic observables from here on. A complete treatment including photons is left for future work.

NON-PERTURBATIVE TREATMENT OF NOISE

In this chapter, we move towards direct self-consistent solutions of stochastic viscous hydrodynamics equations. In section 5.5 we have discussed the challenges associated with direct treatment of thermal noise. We saw that large gradients caused by the fluctuation terms can cause difficulties for numerical algorithm implementations. To overcome these difficulties, we have used a low pass noise filter.

7.1 NOISE FILTER

Hydrodynamics is a long-wavelength theory. The delta-functions in eqs. (5.26) and (5.27) effectively incorporate fluctuations at all wavelengths, including infinitesimally small wavelengths. Replacing the continuous Dirac-delta with discrete Kronecker-delta divided by the cell volume as in eq. (5.28) cuts off all wavelengths below $2\Delta x$ where $\Delta x \sim (\Delta V)^{1/3}$. In momentum space language, this translates to being restricted to small wavenumber modes. The discrete-grid acts as a low pass filter allowing only modes with wavenumber less than $\frac{2\pi}{2\Delta x}$.

Even after the low pass noise filter provided by discretization, we are left with large gradients. Most algorithms for solving partial differential equations assume that the underlying function that we are solving for varies slowly, at least over the length scale of cell width. Clearly, by its very design, thermal fluctuations vary rapidly over this scale. We need to put a lower wavenumber cutoff in the noise filter.

In the small wavenumber limit, the dispersion relation for small fluctuations in linearized hydrodynamics is given as [116]

$$\omega = \pm c_s k - i\gamma_s k^2/2 \tag{7.1}$$

where ω is the circular frequency of the mode, k is its wavenumber, c_s is the speed of sound and γ_s is the dissipative constant which is a function of viscosity. For shear modes, $\gamma_s = \frac{2\eta}{3(\varepsilon_0 + P_0)}$ and for bulk modes, $\gamma_s = \frac{\zeta}{2(\varepsilon_0 + P_0)}$. The imaginary part of the dispersion relation goes as $\omega \propto k^2$. As we see here, modes decay in time-frame proportional to $1/k^2$

In [117], a dissipative scale k_* for thermal fluctuations was determined by comparing the macroscopic frequencies to the dissipation rate. For Bjorken expansion, the macroscopic scale is given by the expansion rate $\frac{1}{\tau}$.

$$\omega = \frac{2\pi}{\tau} \sim \frac{\gamma_s k_*^2}{2} \quad (7.2)$$

$$k_* \sim \sqrt{\frac{4\pi}{\gamma_s \tau}}. \quad (7.3)$$

Very high wavenumber modes decay very rapidly to reach equilibrium and could be absorbed in the equation of state. For our simulation, this cutoff scale is determined by the relaxation time. Shear modes larger than wavenumber of the order $\frac{1}{\tau_\pi}$ and bulk modes larger than the order $\frac{1}{\tau_\Pi}$ decay faster than the relaxation time and are effectively at equilibrium. We would not be able to observe the effects of such fast modes.

We remove these modes by using an explicit noise filter. We locally determine the wavenumber cutoff scale p_{cut} in each spatial grid-cell at each sampling of the noise. p_{cut} is chosen to be of the form

$$p_{cut} = \frac{x}{\tau_\pi} \quad (7.4)$$

for shear modes. Here x is a number of order 1. We will illustrate the effect of explicit choice of x in next sections. But once an x is chosen, we begin the next steps.

The noise source term tensor $\zeta^{\mu\nu}$ is sampled in the local rest frame (LRF) of each cell. This step is similar to the sampling done in the perturbative approach. After sampling our noise in LRF, we boost it to the lab-frame and put it through a wavenumber filter. This filter is decided locally as temperature and energy density varies throughout the system and accordingly the relaxation time is also different. In practice, our procedure is as follows

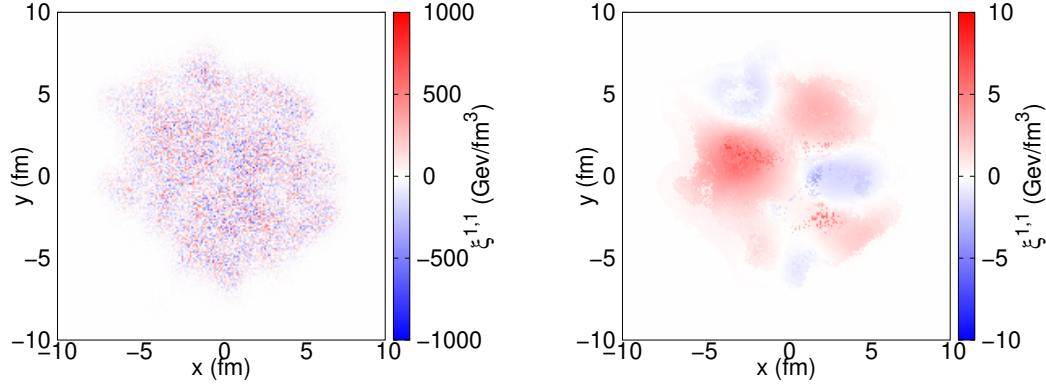


Figure 7.1: Sampled noise component $\xi^{1,1}$ at midrapidity. Left: before removing high wavenumber modes. Right: after removing modes larger than $p_{cut} = 0.6/\tau_\pi$.

1. We numerically take the Fourier transform of all the independent terms of noise source tensor $\tilde{\zeta}^{\mu\nu}$. Now we have noise terms in momentum space with wavenumbers reaching up to $\frac{2\pi}{\Delta V \Delta \tau}$. For numerical Fourier transforms, we use the FFTW library [158].
2. We then do multiple inverse transforms imposing different cutoffs for each of them. For example we have a series of cutoffs $\lambda_1, \lambda_2, \dots, \lambda_n$. For each of these cutoffs we set modes above appropriate λ to zero and then inverse transform to position space. So we end up with a number of realizations of noise, all of which are derived from our original sampling and have been put through different wavenumber filters.
3. Now in each cell (in position space) we determine what the local cutoff should be and we use the appropriate inverse transform for that. For example, if $\lambda_1 < p_{cut} < \lambda_2$, we use the inverse transform with λ_2 for that cell (higher cutoff, fewer modes removed). So all the modes above λ_2 are neglected for that position in space-time.

With this filtered noise source term, we solve the stochastic hydrodynamics equations until freeze-out point and then follow up with particalization using Cooper-Frye mechanism and hadronic cascade and decays using UrQMD model.

7.2 TESTS IN SIMPLE SYSTEMS

We can get some intuition to check our implementation of thermal noise from the deterministic calculations discussed in section 5.3. As we know, the average of thermal noise would be zero. So, we have to go to two or higher point correlators. For simplicity, we use two-point correlators. Specifically, we take inspiration from the two point correlators evaluated in [117].

7.2.1 Two-point correlators in momentum space

To evaluate equal time two-point correlators of fluctuation modes, we evaluate $\langle \delta p^\mu(k_1) \delta p^\nu(k_2) \rangle$ in our simulation and compare it to the equilibrium values. The averaging is over an ensemble. Here δp^μ is the fluctuation in four momentum. For convenience, we choose a direction in momentum space by defining a unit vector (\hat{k}).

As we are using white noise, at equilibrium, the two point correlators take the form [117]

$$\langle \delta p^\mu(\tau, k_1) \delta p^\nu(\tau, k_2) \rangle = N_0 \delta^3(k_1 + k_2). \quad (7.5)$$

Equilibrium value N_0 can be given by the equipartition function

$$N_0 = T(\epsilon_0 + P_0). \quad (7.6)$$

We conveniently choose $k_2 = -k_1$ for our calculations. We evaluate $\langle \delta p^\mu(k) \delta p^\nu(-k) \rangle$ at different distances from the origin in momentum-space in direction \hat{k} . We work in the basis formed by the unit vectors in the radial direction ($\mathbf{1}, \pm \hat{k}$) and two unit vectors pointing to the directions orthogonal to the radial direction.

Components of δp^μ along the radial directions are denoted by δp_+ (for radial outward) and δp_- (for radial inward). Components along two orthogonal directions are denoted

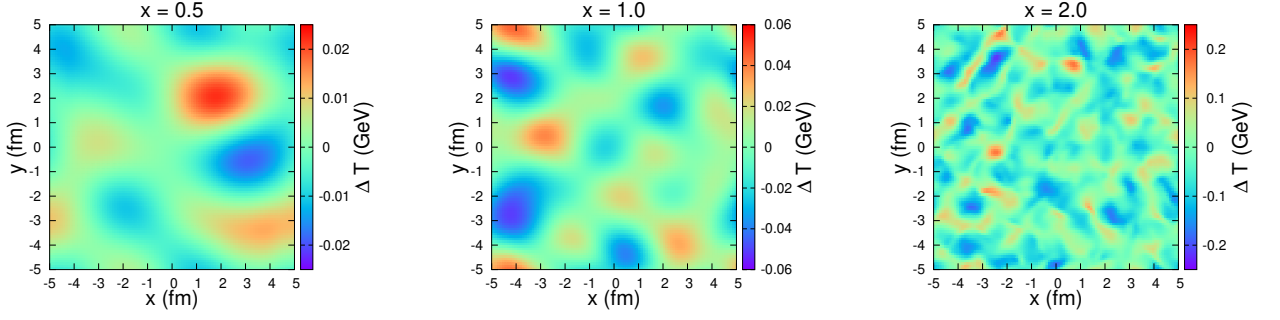


Figure 7.2: Snapshots of temperature fluctuations in a 2D slice of static fluid at a fixed time for different values of x .

by δp_{T_1} and δp_{T_2} . Consequently, we have the following diagonal components of N in this basis.

$$\langle \delta p_{\pm}(k_1) \delta p_{\pm}(k_2) \rangle = N_{++/--} \delta^3(k_1 + k_2) \quad (7.7)$$

$$\langle \delta p_{T_1}(k_1) \delta p_{T_1}(k_2) \rangle = N_{T_1 T_1} \delta^3(k_1 + k_2) \quad (7.8)$$

$$\langle \delta p_{T_2}(k_1) \delta p_{T_2}(k_2) \rangle = N_{T_2 T_2} \delta^3(k_1 + k_2) \quad (7.9)$$

7.2.2 Static tests

Before we choose a particular value of x in eq. (7.4), we would like to examine how the evolution differs for different choices of p_{cut} . We begin by examining a static fluid. A static fluid is normally at global equilibrium. Thermal fluctuations cause deviation from this global equilibrium. We begin with a brick of fluid with energy density $\varepsilon_0 = 250 \text{ GeV}/\text{fm}^3$. Subsequently, we evolve this fluid using the equations of stochastic dynamics using ultraviolet noise filter with x values in eq. (7.4) as 0.5, 1 and 2. We have used periodic boundary conditions. For these tests, the conformal equation of state is used. As we take a conformal fluid, bulk viscosity is set to zero. Shear viscosity/entropy density is fixed at 0.2.

In fig. 7.2, we see that the fluctuation domains are bigger for smaller x values and smaller for larger x . Also, it is noteworthy that the fluctuation magnitude itself is larger for larger x and smaller for smaller x . This of course is the consequence of using a more stringent low pass filter at smaller x . Removal of high wavenumber modes effectively

averages noise over nearby regions in physical space and forms bigger patches with smaller fluctuation sizes.

Fig. 7.3 shows the ratio of two-point correlators in momentum space with their equilibrium values for different times. These values are evaluated by averaging over 100 fluctuating static fluid events. The values are evaluated in the x-direction in momentum space. The x-axis of the plot is written in the terms of a dimensionless quantity $k_x * \tau_\pi$. Since, the cutoff scale is $p_{cut} = x/\tau_\pi$, values 0.5, 1 and 2 on the x-axis of the plot represent p_{cut} for x 0.5, 1 and 2 respectively. We can see that the N/N_0 values in our simulations starts dropping much below the equilibrium values for wavenumbers slightly below the p_{cut} . Further, we see that the N/N_0 ratios hovers around 1 (as expected). Finally, and most crucially, the correlator values for different x values, i.e., correlator values for different wavenumber cutoffs p_{cut} agree with each other for lowest wavenumber values. This supports that if we are only interested in the physics over large spatial scales, we can safely remove large wavenumber modes in our noise sampling by using a low pass filter and still retain the relevant physics.

7.2.3 Bjorken tests

Tests in section 7.2.2 were done for a static fluid at global equilibrium. Obviously, this is not a real representation of the situation in a heavy-ion collision. Fluid created in the heavy-ion collisions is rapidly expanding, particularly in the z-direction.

Bjorken flow captures this feature of the fluid (see section 2.1.2.1). Deterministic calculations evaluating the two-point correlators for Bjorken expanding fluids have been done [117]. We use these results to compare the two-point correlators of fluctuations generated by our stochastic method.

Again, we initialize hydrodynamics with a brick of fluid. But now we evolve this brick in Milne coordinates used by MUSIC (see section 2.1.2.2 for a discussion on Milne coordinates and MUSIC). This essentially means that the system keeps expanding in the z-direction as space expands. Consequently, the energy density and temperature keeps decreasing. As shear relaxation time τ_π is a function of energy-density (see eq. (2.17)),

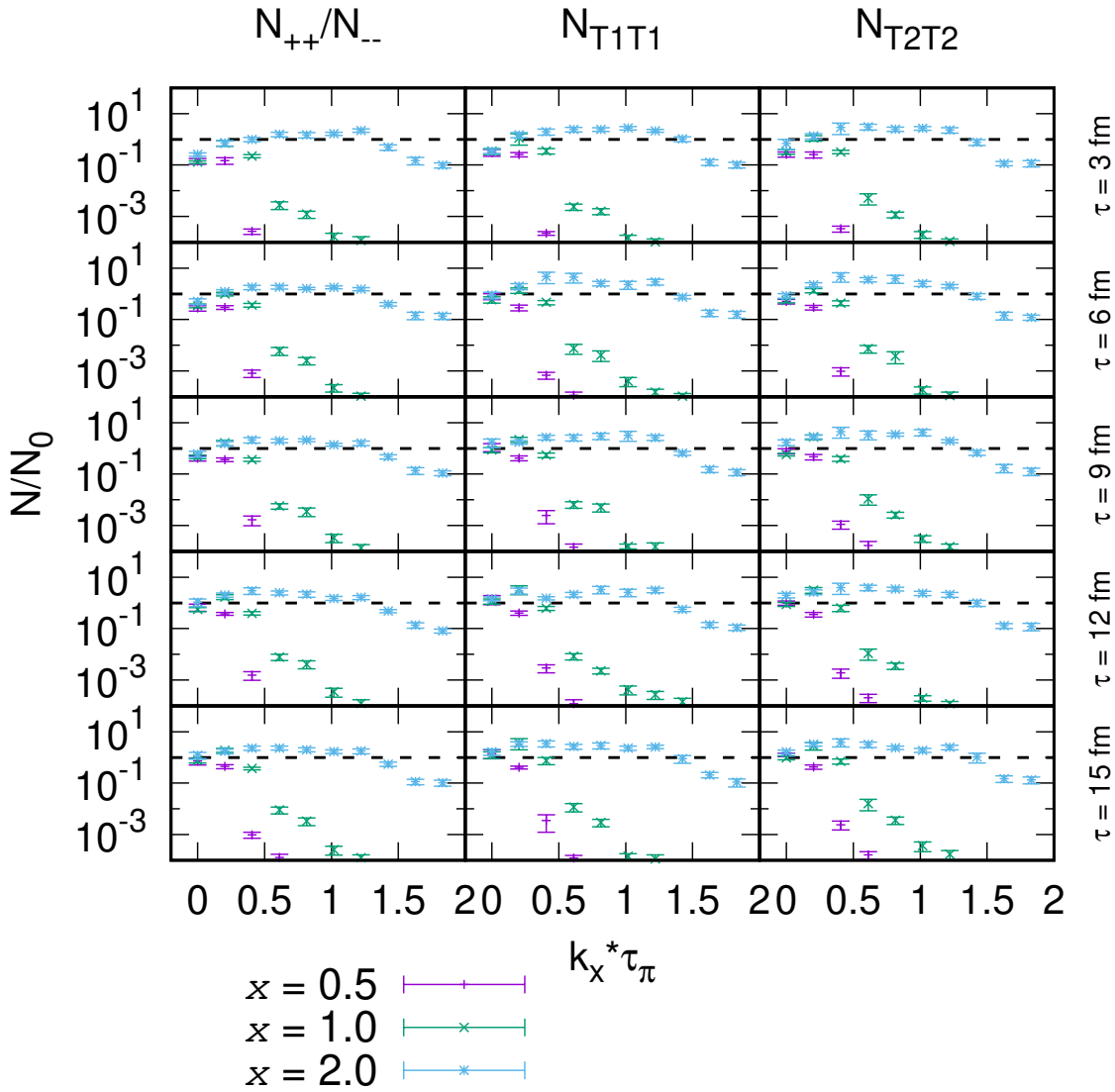


Figure 7.3: Ratio of two point correlators of noise terms with their equilibrium values for a static fluid with different x values. The dashed line is at $N/N_0 = 1$.

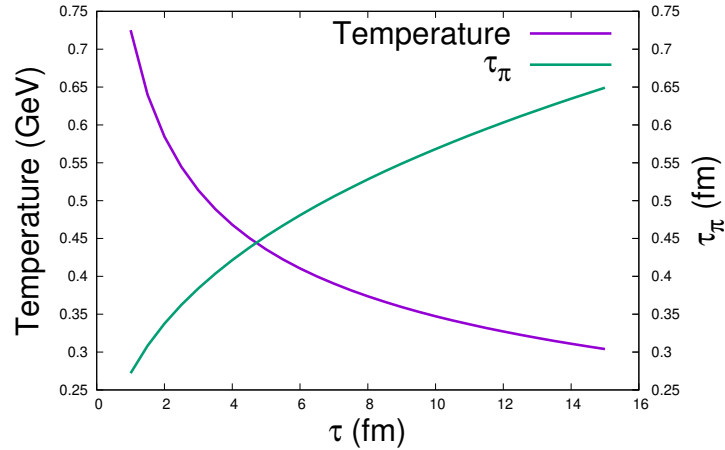


Figure 7.4: Temperature and shear relaxation time evolution with proper time in a fluid expanding with Bjorken solution.

it also changes with time. In fig. 7.4 we can see that the relaxation time increase as the temperature falls with time.

We initialized the brick at $\tau = 1$ fm at energy density $\varepsilon_0 = 500$ GeV/fm³. Again, for these Bjorken tests, we have used a conformal equation of state. Consequently, bulk viscosity is set to zero. Shear viscosity/entropy density is fixed at 0.2. We have used periodic boundary conditions in x and y directions. We used an ensemble of 100 events for these calculations.

As we use $p_{cut} = x/\tau_\pi$ in our low pass filter, p_{cut} decreases with falling temperature. So, to see the effect of low pass filter, we again plot the correlators as function of $k_x * \tau_\pi$ in fig. 7.5. We should keep in mind that τ_π value keeps changing with τ and so the same x -axis values actually correspond to different k_x values at different times. Again, we observe that the N values start to drop below their equilibrium values for k_x slightly below p_{cut} . And again, for low k_x values, N values are same for different x values giving us confidence that low pass filters can be successfully utilized for low wavenumber physics.

In fig. 7.6, we see another illustration of the same effect. We have plotted the ratio of equal time correlators of Fourier transforms of δT^{00} with their equilibrium value. We have calculated these correlators in the rapidity direction. We should note that when using Milne coordinates, the length of a fluid-cell in the rapidity direction keeps changing

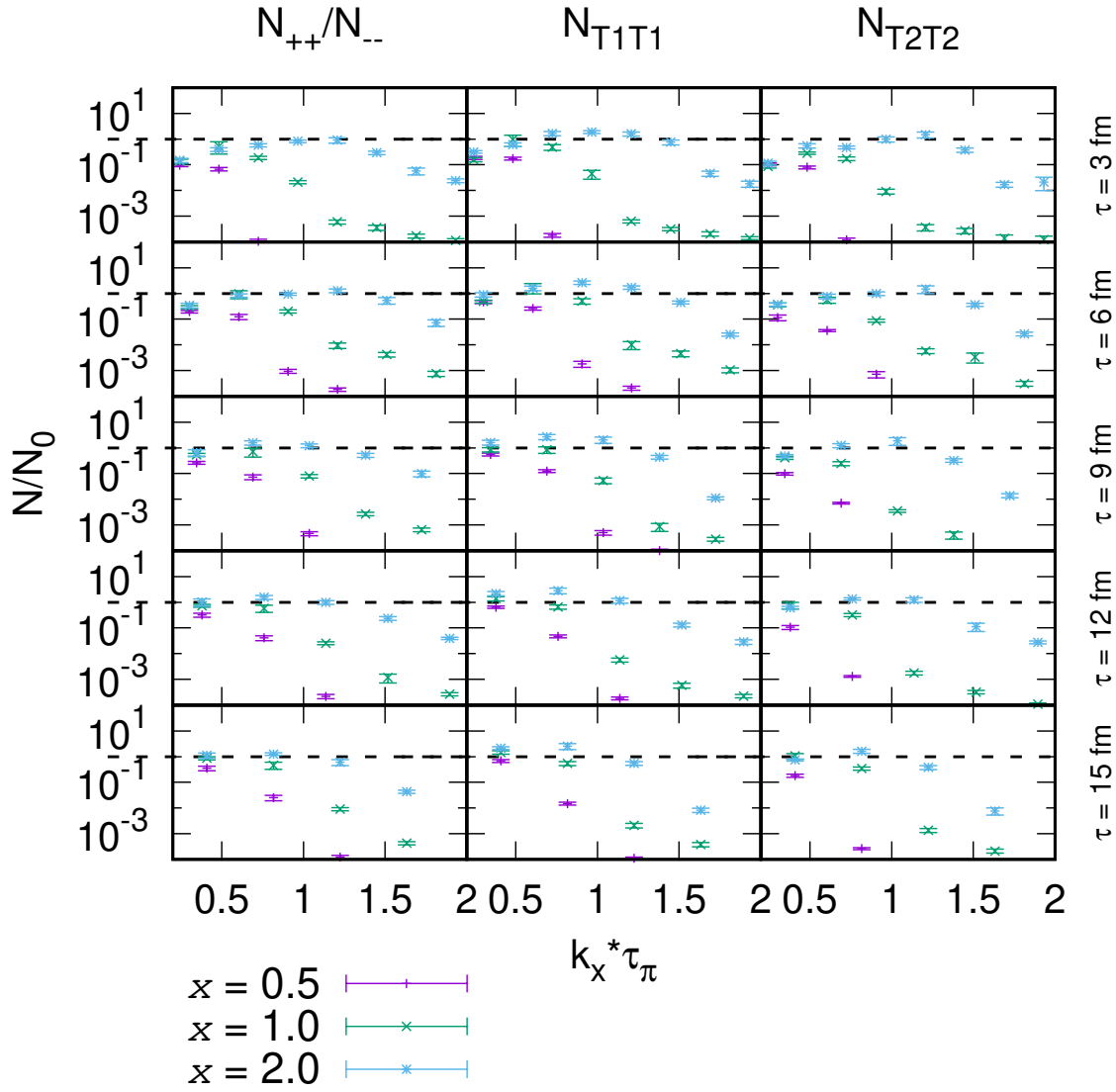


Figure 7.5: Ratio of two point correlators of noise terms in x -direction with their equilibrium values for fluid undergoing Bjorken expansion with different x values. The dashed line is at $N/N_0 = 1$.

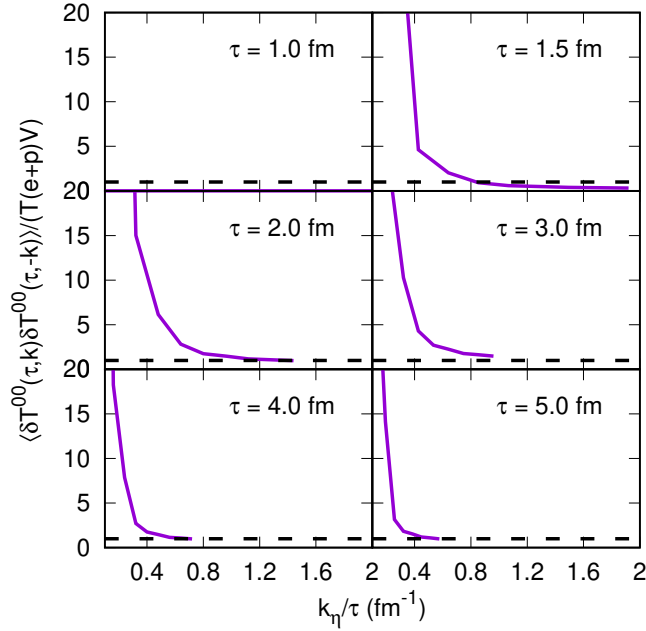


Figure 7.6: Ratio of two point correlators of noise terms in rapidity-direction with their equilibrium values for a static fluid with different x values.

with time as $\tau * d\eta$. Consequently, we can only go so far as $2\pi / (\tau * d\eta)$ wavenumber in the rapidity direction. So, with increasing time, our maximum wavenumber resolved keeps decreasing. So, in most cases, we do not reach the p_{cut} value in rapidity direction.

In fig. 7.6, we see the noise correlator starting at zero value at $\tau = 1$ fm. There are no thermal fluctuations at initialization. Slowly, fluctuations build and as it stabilizes around $\tau = 2$ fm, it quickly goes to its equilibrium value at high wavenumbers.

We did mode analysis of fluctuations in static fluid and in Bjorken flow. We know the equilibrium behaviour of fluctuations in these systems. We see how fluctuation correlators rapidly go to their equilibrium values with increasing wavenumbers. We show how our simulations with different p_{cut} are able to capture the low wavenumber physics of these fluctuations.

7.3 MODEL DETAILS

We now move to evaluate realistic effects of shear thermal fluctuations on experimental observables. We use the IP-Glasma initial conditions [40, 41] (see section 2.1.1) to model the initial state of collisions. We switched from the IP-Glasma to hydrodynamics at proper time $\tau = 0.4$ fm. Equation of state from the hotQCD collaboration [15] matched with the equation of state from hadron resonance gas [159] is used. η/s value is fixed at 0.13. A temperature dependent bulk viscosity profile parameterized in [160] and used in [65] is used.

Please note that while a non-zero bulk viscosity is used, for the results in this chapter, associated bulk thermal fluctuations are not implemented. The purpose of this is to implement one feature at a time to better study its consequences on observables.

The fluid is hadronized using the Cooper-Frye prescription implemented in the iSS implementation [72]. This switch from fluid to hadrons is done at a fixed temperature of 145 MeV. Generated hadrons are passed through the hadronic afterburner UrQMD [74, 75] where it goes through hadronic rescatterings and resonance decays.

The value of x in eq. (7.4) is fixed at 0.5. This parameter choice is justified in the next section alongside the observables we evaluate. We have used 600 events per 10% centrality bins, both for thermally fluctuating and non-fluctuating calculations.

7.4 MID-RAPIDITY OBSERVABLES

7.4.1 Multiplicity

We start by evaluating charged-hadron multiplicity. Normalization of initial energy is done to match the multiplicity for 0-5% centrality bin for the non-fluctuating case as in [41] and is kept same for all centrality bins. It is also kept same for the fluctuating case. In fig. 7.7, we see that the thermal fluctuations hardly affect multiplicity. Naively, one can expect thermal fluctuations to introduce additional gradients in the system and increase the net-entropy and hence increase multiplicity. On the contrary, fluctuations actually

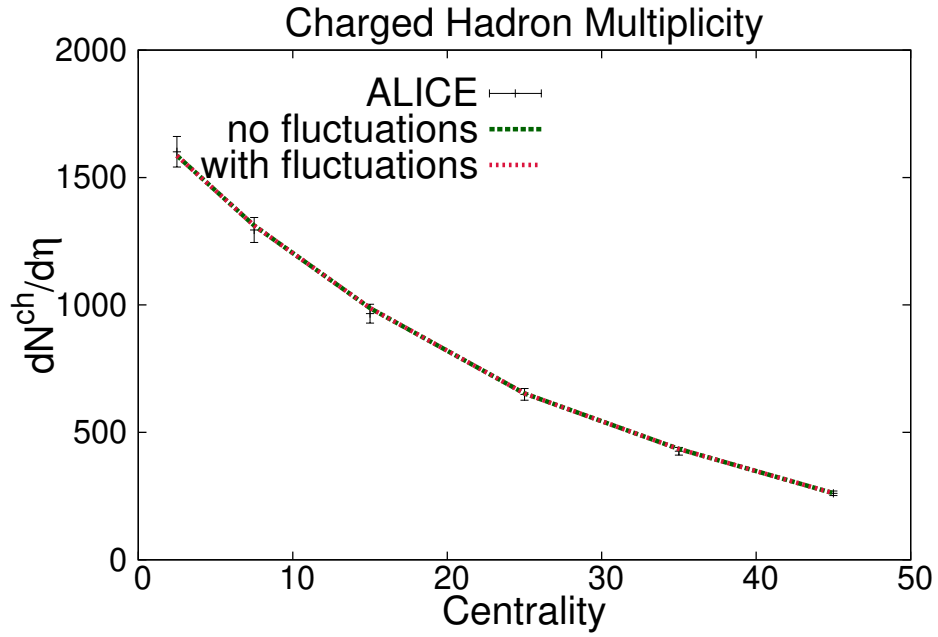


Figure 7.7: Charged hadron multiplicity for Pb-Pb collisions at $\sqrt{s} = 2.76$ TeV with and without thermal fluctuations. Data points are taken from the ALICE collaboration [91].

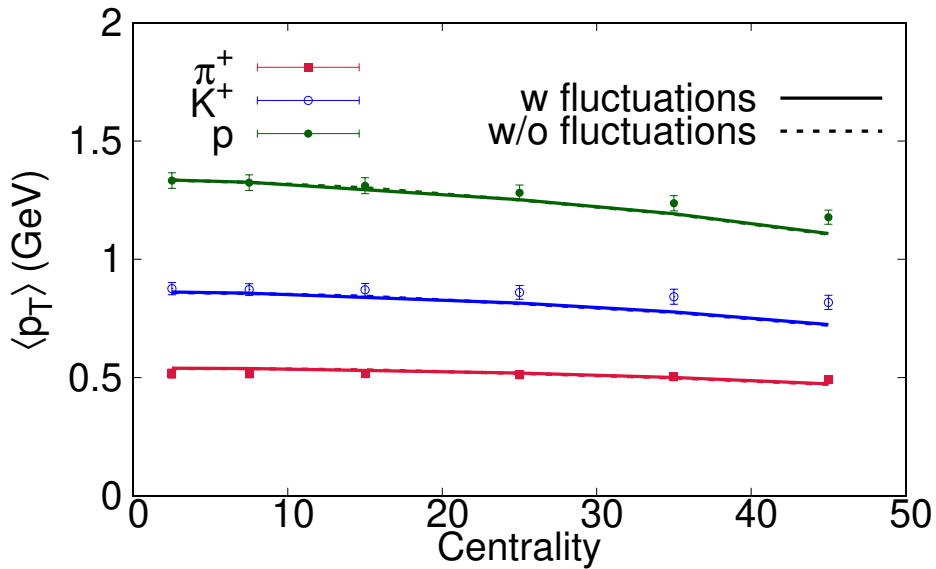


Figure 7.8: Identified particles' mean transverse momentum for Pb-Pb collisions at $\sqrt{s} = 2.76$ TeV with and without thermal fluctuations. Data points are taken from the ALICE collaboration [161].

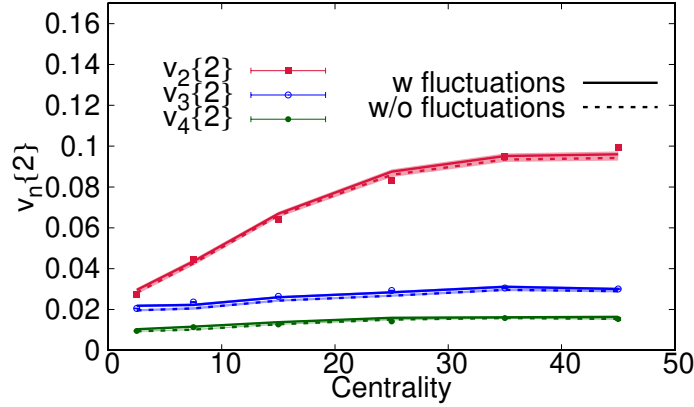


Figure 7.9: Charged hadron integrated v_n for Pb-Pb collisions at $\sqrt{s} = 2.76$ TeV with and without thermal fluctuations. Data points are taken from the ALICE collaboration [162].

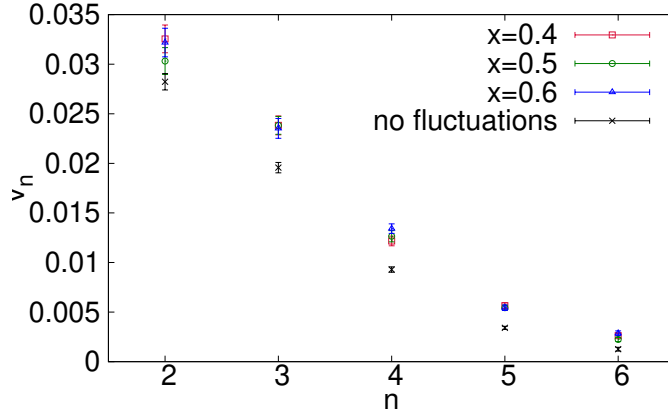


Figure 7.10: p_{cut} dependence of charged hadron integrated v_n for 0-5% centrality Pb-Pb collisions at $\sqrt{s} = 2.76$ TeV with thermal fluctuations.

take the system away from the maximal entropy state while dissipation strives to bring it back to equilibrium. This balance between fluctuations and dissipation as related by the fluctuation-dissipation theorem keeps the entropy fluctuating around the maximal entropy condition. All positive energy contributions by thermal fluctuations are balanced by the equivalent negative energy contributions keeping the energy conservation intact. Consequently, we do not expect particle multiplicities to rise or fall which is what we observe in fig. 7.7.

7.4.2 Mean p_T

Next we look at the mean transverse momentum. These have been measured for identified hadrons like pions, kaons and protons by the ALICE collaboration [161]. The momentum spectrum of a particle, and consequently its mean value, is sensitive to the bulk viscosity and to post hadronization cascade [65]. It is not sensitive to shear viscous tensor, and by extension, the shear viscous fluctuations. This is shown in fig. 7.8.

7.4.3 v_n

Now we look at the charged hadron v_n (see section 3.3.1). Like the initial state fluctuations, thermal fluctuations also contribute to anisotropy in the system and consequently enhance v_n . In fig. 7.9, we see a small enhancement in p_T -integrated v_2 , v_3 and v_4 .

It becomes critical to check the effect of choice of p_{cut} . In fig. 7.10, we see the values of p_T -integrated v_2 , v_3 , v_4 , v_5 and v_6 for different choice of p_{cut} . We see that the v_n s for fluctuating simulations are consistent with each other i.e. they are within each other's error bars and distinct from non-fluctuating simulation. More crucially, there is no definite order for different choice of x there. Naively, one would expect any given v_n to follow the order $v_n(x = 0.4) < v_n(x = 0.5) < v_n(x = 0.6)$. This is because we are including more modes in $x = 0.5$ as compared to $x = 0.4$ and even more modes in $x = 0.6$. The fact that this ordering is not necessarily followed assures us that within our error limits, we have attained the possible accuracy to determine the effects of thermal fluctuations. This suggests, that the modes above $p_{cut} = 0.4/\tau_\pi$ are largely at equilibrium.

We should also note the caveat in v_2 in fig. 7.10. v_2 is largely a consequence of initial elliptical geometry. Fluctuation contributions to v_2 , both initial and thermal, are small. So we cannot really distinguish fluctuating and non-fluctuating v_2 clearly in fig. 7.10. An effort to clearly separate the errorbars there would be computationally prohibitive and is not undertaken at this stage.

Now let us look at the differential v_n s. In fig. 7.11 we see the problem of separation of fluctuating and non-fluctuating quantities is amplified or v_2 There is clearly increasingly enhanced separation of fluctuating and non-fluctuating v_n as n increases. Again, this is to

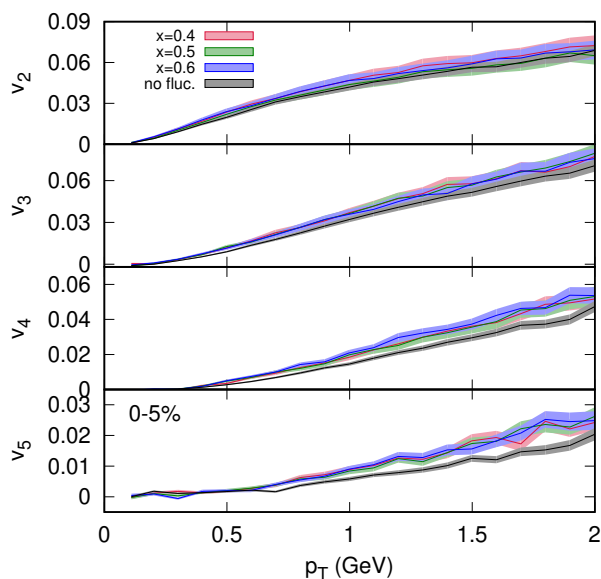


Figure 7.11: p_{cut} dependence of charged hadron differential v_n for 0-5% centrality Pb-Pb collisions at $\sqrt{s} = 2.76$ TeV with thermal fluctuations.

be expected. Small range fluctuations become more and more important as n increases. We notice that there is still no clear hierarchy of v_n values for different p_{cut} , which is consistent with our assumption that modes around p_{cut} are already at equilibrium.

In fig. 7.12 and fig. 7.13, we present the effect of thermal fluctuations on differential v_n . We see that the effect is very small and we are still consistent with data. Effect of thermal fluctuations becomes even smaller for larger centrality as geometric effects take over.

It should be noted that the effect of thermal fluctuations on differential v_n is really small here, which is in contrast with the perturbative calculation shown in fig. 6.2. This is not a contradiction. The perturbative calculation was done in very simple conditions with *no initial-state fluctuations*. Consequently any fluctuation source gave a large relative effect. In this more realistic simulation, we have already included initial state fluctuations using the IP-Glasma model and the **relative** contribution of thermal fluctuations is smaller.

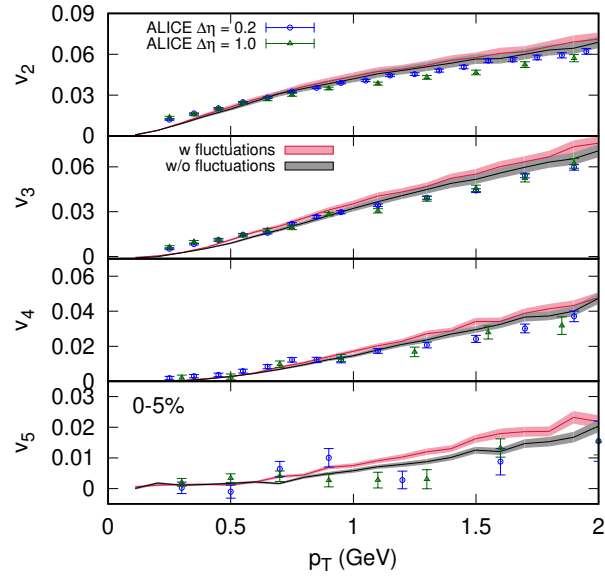


Figure 7.12: Charged hadron differential v_n for 0 – 5% centrality Pb-Pb collisions at $\sqrt{s} = 2.76$ TeV with and without thermal fluctuations. Data points are taken from the ALICE collaboration [162].

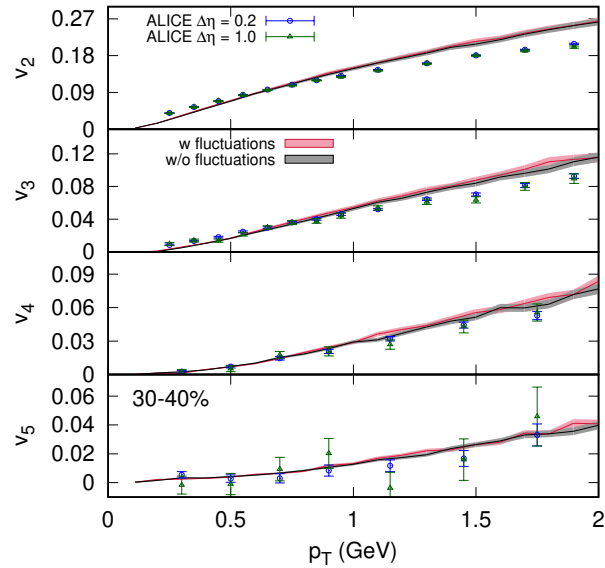


Figure 7.13: Charged hadron differential v_n for 30 – 40% centrality Pb-Pb collisions at $\sqrt{s} = 2.76$ TeV with and without thermal fluctuations. Data points are taken from the ALICE collaboration [162].

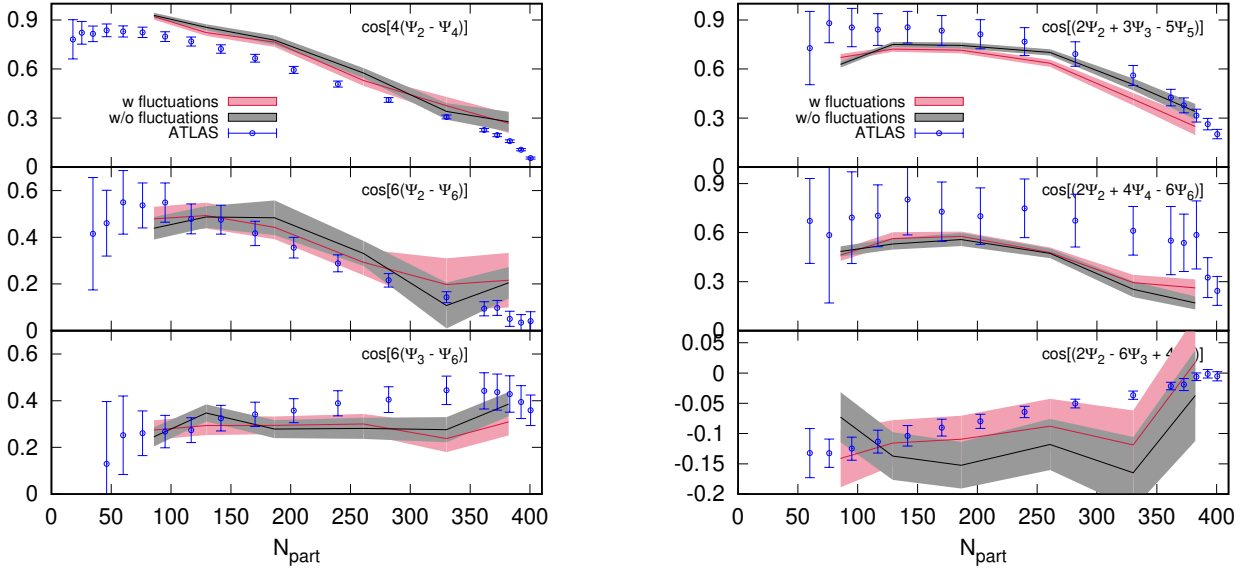


Figure 7.14: Charged hadron event-plane correlators for Pb-Pb collisions at $\sqrt{s} = 2.76$ TeV with and without thermal fluctuations. Data points are taken from the ATLAS collaboration [163]. Centrality to N_{part} conversion was based on MC-Glauber model based table in [163].

7.4.4 Event Plane Correlators

Event plane correlators are shown in fig. 7.14. As described in section 3.3, event-plane correlators measure the decorrelations caused by fluctuations. Again, thermal fluctuations are showing small effects and the calculations, both with and without thermal fluctuations are broadly consistent with data which, however, still carry large uncertainty.

7.4.5 Decomposition of v_n

The v_n can be decomposed into a linear component and non-linear response coefficients. See section 3.3.3 for more details. The key idea of this observable is to disentangle initial-state fluctuation's spatial Fourier decomposition coefficient \mathcal{E}_n and final state momentum Fourier decomposition coefficient v_n . Obviously, \mathcal{E}_n is not accessible to experiments, but the linear contributions v_n^L and the non-linear response coefficients χ can be measured.

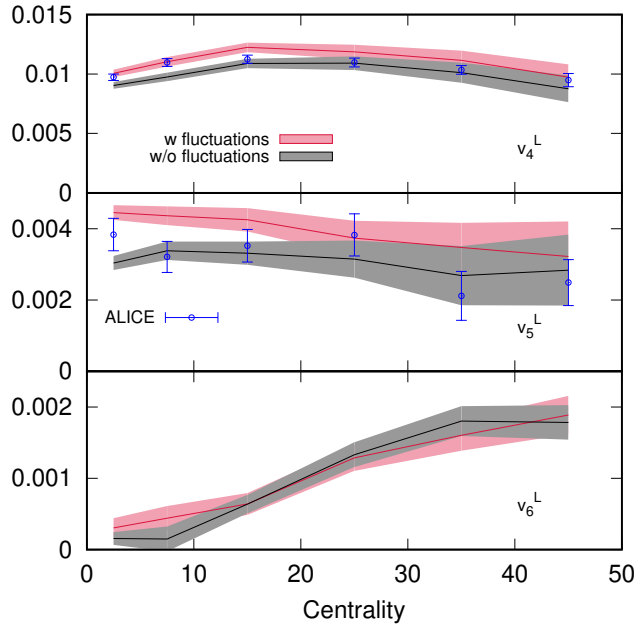


Figure 7.15: Linear part of charged hadron v_n for Pb-Pb collisions at $\sqrt{s} = 2.76$ TeV with and without thermal fluctuations. Data taken from the ALICE collaboration [164].

Thermal fluctuations mimic initial-state fluctuations in the sense that for the purpose of v_n decomposition, they may act like initial state fluctuations. This will be specially true for central collisions where geometric impact-parameter effect is not large and fluctuations are relatively more important.

In fig. 7.15, we see a clear distinction between fluctuating and non-fluctuating calculations of v_4^L and v_5^L for lower centralities. Similarly, in fig. 7.16, a clear signal of shear thermal fluctuations can be seen in χ_{532} . However both seem broadly consistent with data within uncertainties and it is early to confidently say which is preferred. Recently, these quantities have been measured for $\sqrt{s_{NN}} = 5.02$ TeV Pb-Pb collisions [165]. These higher energy collisions have higher luminosity and thus smaller uncertainties. A similar calculation for these higher energy collisions can help us constrain the physics of thermal fluctuations.

To convince ourselves that these signals have little dependence on p_{cut} , we compare these quantities for different p_{cut} values in fig. 7.17. We see that this is so.

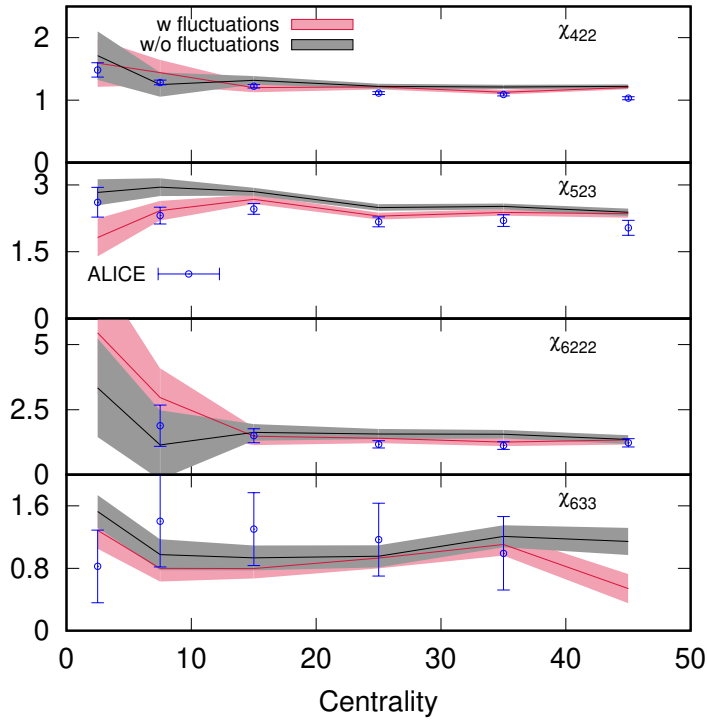


Figure 7.16: Non-linear response coefficients of charged hadron v_n for Pb-Pb collisions at $\sqrt{s} = 2.76$ TeV with and without thermal fluctuations. Data taken from the ALICE collaboration [164].

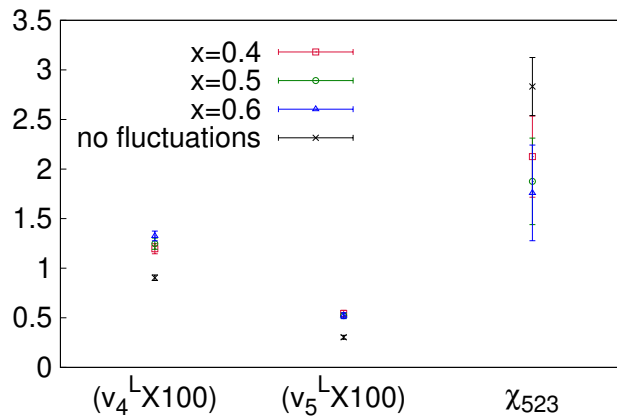


Figure 7.17: p_{cut} dependence of selected linear contributions and non-linear response coefficients of charged hadron v_n for Pb-Pb collisions at $\sqrt{s} = 2.76$ TeV.

7.5 SUMMARY

In this chapter, for the first time, we developed a method to do realistic simulations of heavy-ion collisions including hydrodynamic fluctuations. We used a noise filter to avoid the large gradients present in the relativistic stochastic simulations. This retains all the relevant modes. We extensively tested this noise filter on static and Bjorken fluids. The mode analysis there showed the effects of introducing a wavenumber cutoff. We further used this novel method to do Pb-Pb collision simulations and evaluated the experimental observables. All along the way, we tested the effect of different p_{cut} on experimental observables in a realistic simulation. We have managed to identify observables which show clear signals of hydrodynamic fluctuations. As data resolution improves, so will its discriminating power.

Finally, the techniques developed in this chapter could potentially be used for any other kind of fluctuations in heavy-ion collisions, like the important critical fluctuations which appear when QCD matter traverses close to the critical point in the QCD phase space. These techniques could also be used to simulate different systems which obey stochastic dynamics, do not lend themselves to simple analytic solutions and suffer from the problems of sustained large fluctuation gradients.

BULK VISCOSITY AND FLUCTUATIONS

There is currently not much theoretical guidance on the exact form of bulk viscosity in QGP, though it is known from some phenomenological studies that bulk viscosity is important to explain the particle spectra observed in heavy ion collisions [65]. There are still various forms of bulk viscosity which seem to explain the data [65, 166, 167] and even systematic studies using Bayesian analysis have not been able to narrow down the bulk viscosity profile [168, 169]. Bulk viscosity has also been of interest to the community as it could effectively lead to net negative pressure in the fluid [170], an effect which has come to be known as "cavitation" in the field. Though it is different from how the word cavitation is generally used in fluid dynamics. As a first step, we qualitatively explore the phenomenological effects of bulk viscous hydrodynamic fluctuations. We also examine the effects of net negative pressure. A more extensive study exploring different viscosity profiles with bulk viscous fluctuations to do a better matching with data is left for future studies.

8.1 BULK VISCOSITY PROFILE AND NOISE FILTER FOR BULK VISCOUS FLUCTUATIONS

Much like the shear-viscous fluctuations, the bulk fluctuations are quantified by the fluctuation-dissipation theorem given in eq. (5.27). Naturally, the strength of these fluctuations are proportional to the value of bulk viscosity ζ . Bulk viscous fluctuations have a much simpler structure and can be represented by a scalar.

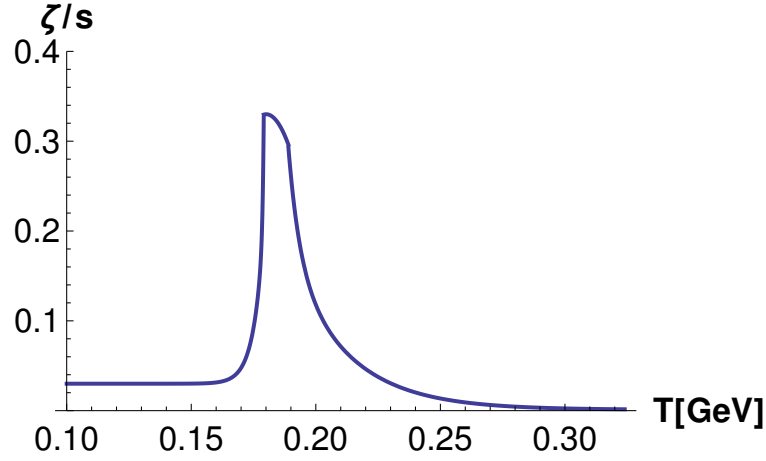


Figure 8.1: Bulk viscosity over entropy density profile given in eq. (8.1).

We have used the bulk viscosity profile used in [65] which was parameterized in [160] fitting data from the lattice QCD [171] and from hadron resonance gas [172]. The bulk viscosity over entropy density is given by

$$\zeta/s = \begin{cases} 0.03 + 0.9e^{(\frac{T}{T_c}-1)/0.002} \\ + 0.22e^{(\frac{T}{T_c}-1)/0.022}, & T < 0.995T_c \\ 0.001 + 0.9e^{-(\frac{T}{T_c}-1)/0.025} \\ + 0.25e^{-(\frac{T}{T_c}-1)/0.13}, & T > 1.05T_c \\ -13.45 + 27.55\frac{T}{T_c} - 13.77\left(\frac{T}{T_c}\right)^2, & \text{otherwise} \end{cases} \quad (8.1)$$

T_c is the crossover temperature taken to be 180 MeV here. This profile is shown in fig. 8.1. For this profile, bulk viscosity is prominent only in a narrow temperature range around T_c .

Like shown in section 7.1 for shear fluctuations, we use a noise filter here are well. Analogous to the shear-relaxation time τ_π , we also have a bulk-relaxation time τ_Π . For our exploratory study here, we have defined the cutoff-wavenumber p_{cut} as

$$p_{cut} = \frac{0.5}{\tau_{max}}, \quad (8.2)$$

where

$$\tau_{max} = \max(\tau_\Pi, \tau_\pi). \quad (8.3)$$

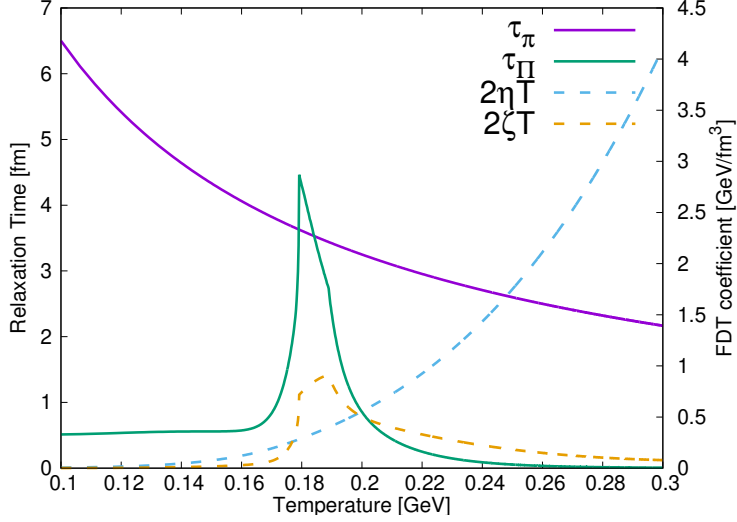


Figure 8.2: Shear and bulk relaxation times and the coefficients in the fluctuation-dissipation theorem for the fluctuations for our simulations.

The choice of cutoff in eqs. (8.2) and (8.3) is a temporary one and needs to be studied further for a more quantitative conclusion. While $p_{cut} = x/\tau_{\Pi}$ is a natural choice for reasons explained in section 7.1, at high temperatures, τ_{Π} fast approaches zero. This causes numerical issues as while non-fluctuating quantity $\Pi \sim \zeta\theta$ is almost zero, the fluctuating component $\propto 2\zeta T$ could be relatively much larger.

Fig. (8.2) presents an accurate picture of our choice of p_{cut} for bulk fluctuations. The yellow line shows the strength of bulk fluctuations which is significant in a narrow temperature range around T_c . Our choice of cutoff in eq. (8.2) removes more bulk modes than bulk relaxation time would allow in all regions except in a very window near T_c , where $\tau_{\Pi} > \tau_{\pi}$. This region coincides with maximum trace anomaly as obtained from the lattice QCD results. Effectively, we are only focused on the effects of the bulk viscosity in a narrow region near T_c .

This calculation including bulk fluctuations is exploratory in nature. A more comprehensive future study will better explore the choice of p_{cut} such that the observables are independent of it. It would also explore different bulk viscosity profiles used in the literature and quantify the effects of bulk fluctuations with those profiles.

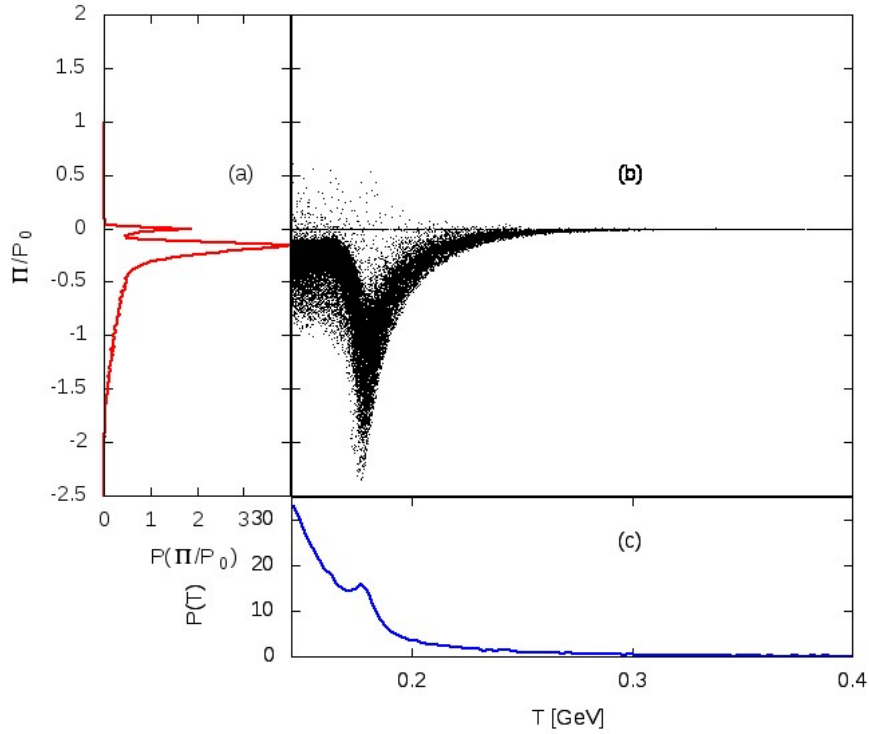


Figure 8.3: This represents one 40-50% centrality Pb-Pb collision event at $\sqrt{s} = 2.76$ TeV without thermal fluctuations. (a) shows the probability density of a fluid cells to have a certain Π/P_0 value throughout the lifetime of the fluid state, while (c) shows the probability density of fluid cells to have a certain temperature. (b) is the scatter plot of fluid cells on the temperature- Π/P_0 axis where each point denotes one spatio-temporal fluid cell.

8.2 EFFECTS OF BULK VISCOUS FLUCTUATIONS

Bulk viscous pressure acts against the direction of expansion of fluid. When the fluid formed in heavy-ion collisions is expanding outwards, bulk viscosity effectively pulls it inwards and slows down the expansion. This delays the cooling down of fluid and enhances the lifetime of the QGP fireball. This also reduces the acceleration of the fluid which results in lower mean transverse momentum ($\langle p_T \rangle$) of particles.

Fig. (8.3) shows the distribution of fluid cells in a 40 – 50% centrality event throughout the lifetime of QGP fluid. This event does not have any thermal fluctuations. We can see that the Π/P_0 distribution is bi-modal. One peak is at $\Pi = 0$, which corresponds to

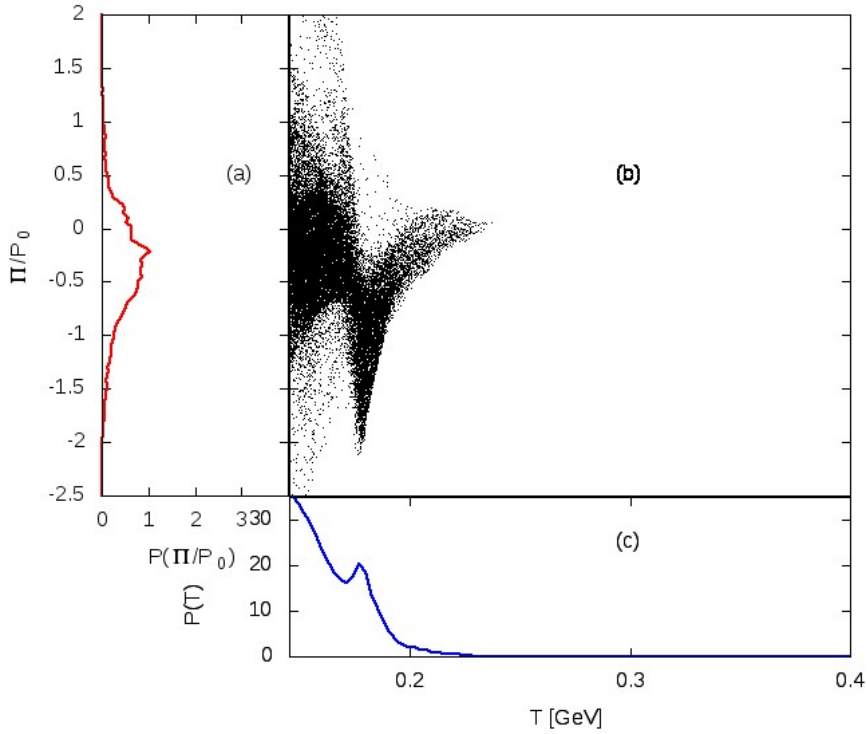


Figure 8.4: Same as fig. 8.3 but with shear and bulk hydrodynamic fluctuations.

large regions of fluid where bulk viscosity is effectively zero. Another, bigger peak is at a small negative value ~ -0.2 . So the net kinematic pressure $P_0 + \Pi$ is reduced. Panel (c) provides further insight. Distribution peaks at the switching temperature 145 MeV, which is understandable as fluid is very dispersed at that temperature and occupies a much larger spatial volume. But there is another peak at 180 MeV, which coincides with the peak in fig. 8.1. This just shows that the fluid there is slowed down because of lower kinematic pressure. Panel (b) is the scatter plot of spatio-temporal fluid cells on the temperature- Π/P_0 axis.

Fig. 8.4 shows a similar plot for a collision event with shear and bulk fluctuations. Events in fig. 8.3 and fig. 8.4 have been initialized with the exact same initial conditions. Only difference in these figures is the presence of thermal fluctuations in the later event. Just this one realization of fluctuating event already provides us with qualitative insight. In panel (a) in fig. 8.4, we see that the Π/P_0 value is distributed over a much wider range. Part of this range also covers positive values of Π/P_0 . This is very significant as fluctuating Π could effectively enhance kinematic pressure. The net effect of bulk

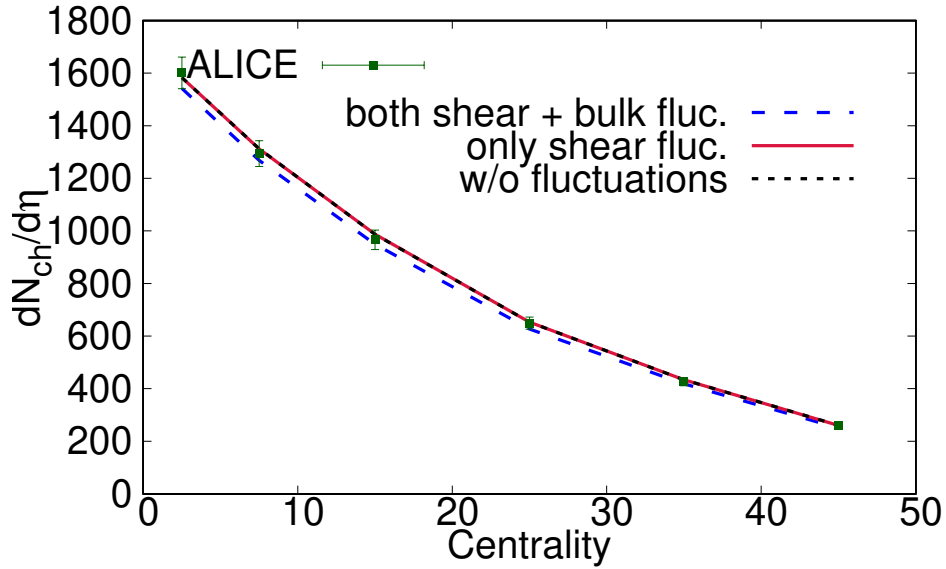


Figure 8.5: Charged hadron multiplicity for Pb-Pb collisions at $\sqrt{s} = 2.76$ TeV with bulk fluctuations. Data points are taken from the ALICE collaboration [91].

fluctuations is to counter the effect of bulk viscosity, which makes theoretical sense (look at our discussion in section 5.2).

There is another subtle issue here which should be addressed. Bulk fluctuations, by their very nature, either increase or decrease kinematic pressure and consequently increase or decrease net acceleration. But this effect is not symmetric. Increased kinematic pressure would rapidly expand the fluid lowering the temperature. Decreased kinematic pressure would just reduce the expansion speed, while not affecting the temperature. Effectively, there is no counter process to rapid cooling in some parts of fluids. There is no analogous rapid heating. So effectively, bulk fluctuations lead to faster expansion and hence faster cooling of the fireball. This effect can also be seen by comparing fig. 8.4 with fig. 8.3. There are very few spatio-temporal cells at higher temperature regions in the event with bulk fluctuations, which is a consequence of rapid cooling. The parallel to this effect can be found in the complementary deterministic hydro-kinetic analysis of bulk noise [118] where a shift in temperature is required to account for the energy in bulk fluctuation modes. This temperature correction is not present in the shear fluctuation analysis [117].

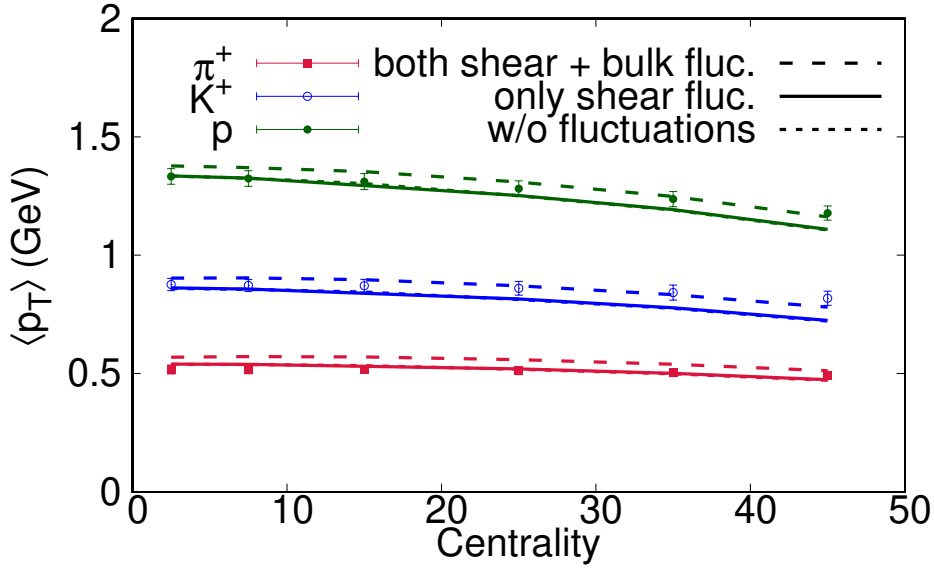


Figure 8.6: Identified particles' mean transverse momentum for Pb-Pb collisions at $\sqrt{s} = 2.76$ TeV with bulk fluctuations. Data points are taken from the ALICE collaboration [161].

Now let us look at some key observables. In fig. 8.5, we observe that the net multiplicity has decreased by about 4%. Just shear fluctuations alone have no such effect. This is an effect of the rapid cooling explained above. Bulk fluctuations asymmetrically reduce net entropy production and thus cause a decrease in particle multiplicities. This is not the case for shear fluctuations.

On a similar note, we see the effects of bulk fluctuations on the mean transverse momentum in fig. 8.6. Rapid cooling caused by bulk fluctuations increases the net $\langle p_T \rangle$.

Fig. 8.7 and 8.8 shows the effect of bulk fluctuations on the integrated v_n and the event-plane correlators. Bulk fluctuations tend to make more difference in these observables than their shear counterpart.

We again wish to emphasize that the calculations shown in figs. 8.5 to 8.8 should be used only to get qualitative insight on the effects of bulk fluctuations. A more comprehensive quantitative study to explore different bulk viscosity profiles and different cutoff wavenumber p_{cut} is left for future work, likely involving Bayesian techniques. However, it is clear that the inclusion of thermal fluctuations will cause a recalibration of transport coefficients in general.

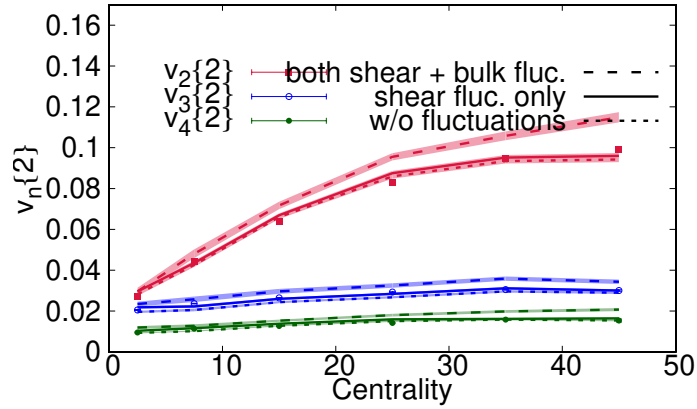


Figure 8.7: Charged hadron integrated v_n for Pb-Pb collisions at $\sqrt{s} = 2.76$ TeV with bulk fluctuations. Data points are taken from the ALICE collaboration [162].

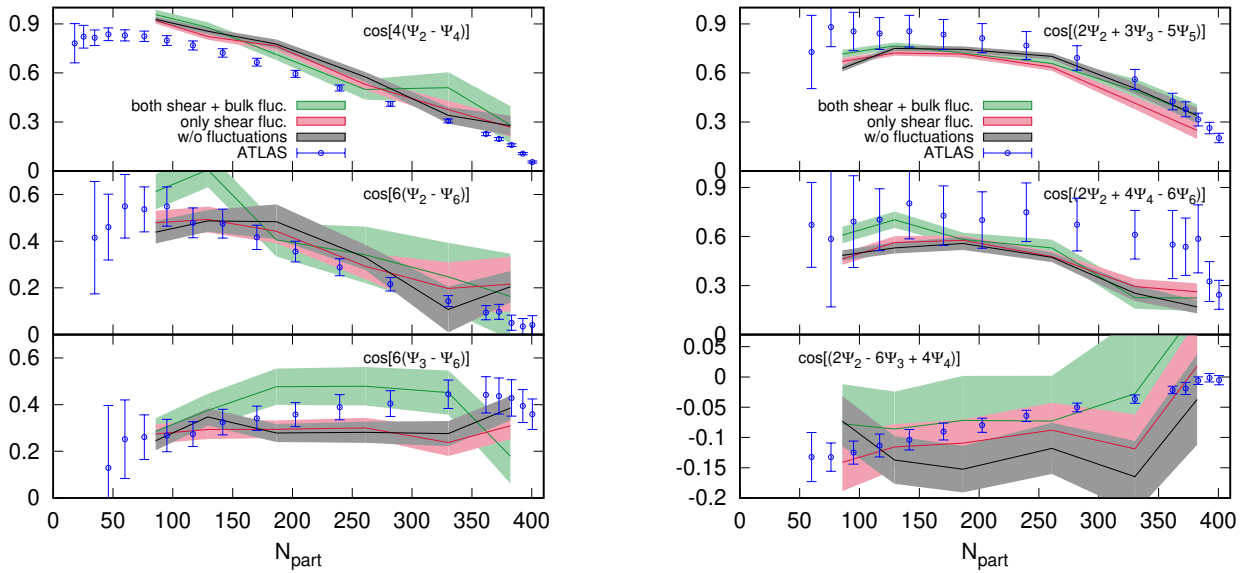


Figure 8.8: Charged hadron event-plane correlators for Pb-Pb collisions at $\sqrt{s} = 2.76$ TeV with bulk fluctuations. Data points are taken from the ATLAS collaboration [163]. Centrality to N_{part} conversion was based on MC-Glauber model based table in [163].

So far, in this chapter, we have avoided discussion on the scenario where $\Pi/P_0 < -1$. This implies that the net kinematic pressure $P_{kin.} = P_0 + \Pi < 0$. What does net negative pressure imply? We undertake this discussion in the next section.

8.3 NEGATIVE KINEMATIC PRESSURE

We know that thermodynamics is the theory of a system at equilibrium. If we relax this condition and demand only local equilibrium, i.e. equilibrium only in the immediate neighborhood of any point in space-time, we can use ideal hydrodynamics. Here the term immediate neighborhood is in the same sense it is typically used in mathematics. Viscous hydrodynamics is the applicable theory when there are small deviations from this local thermodynamic equilibrium. Viscous terms are typically added as corrections to the ideal hydrodynamic terms.

The key assumption in using viscous hydrodynamics is that these corrections are small. Though recent work has shown [173] that hydrodynamic solutions work surprisingly well even far away from equilibrium. As such, the situation where $|\Pi/P_0| > 1$, is troubling from a theoretical consistency viewpoint. However, this situation appears in heavy-ion collision simulations. This can even be seen in a sample event depicted in fig. 8.3.

This condition, when $\Pi/P_0 < -1$, is often termed "cavitation" in strongly coupled plasma literature [170, 174–185]. This nomenclature extends even to literature of neutron stars [186] and cosmology [187]. The idea is that when the kinematic pressure $P_{kin.} = P_0 + \Pi$ turns negative, the fireball starts experiencing an inward pressure and breaks forming "cavities".

In a recent work Habich and Romatschke [182] have argued that when $P_0 + \Pi$ (called effective pressure in their paper) drops below the hadron resonance gas pressure (which is small but positive), hadron gas will be the preferred state of matter. This will form bubbles of hadron gas in the QGP medium, akin to the phenomenon of cavitation. Subsequently Byers et al. [170] have suggested that this will lead to immediate hadronization at higher temperatures and we will get a much different spectra than what we actually observe in experiments.

In this section we show that while large negative Π certainly contributes to fragmentation of the fireball, it is not synonymous with it. We also argue against the use of term cavitation for the condition $P_0 + \Pi < 0$ as it concocts a misleading image.

8.3.1 *Thermodynamic vs kinematic pressure*

First of all, let us discuss the difference between the thermodynamic and the kinematic pressure. Thermodynamic pressure P_0 , by its very definition, is an equilibrium quantity. This is the pressure that appears in the equation of state obtained from lattice QCD.

On the other hand, kinematics in the eqs. (2.15) and (2.16) is determined by the kinematic pressure $P_{kin.} = P_0 + \Pi$. Kinematic pressure determines the acceleration experienced by the fluid.

In most applications of fluid dynamics, $\Pi \ll P_0$ and so $P_0 \equiv P_{kin.}$. However, for our purposes of simulating heavy-ion collisions, there is this unique situation where Π is comparable to P_0 in magnitude. In the former case, it is reasonable to equate the two and infer that when $P_{kin.}$ drops below the vapor pressure, there is a phase change.

For illustration, let us consider water. Water has a well known phase diagram. The density, temperature and thermodynamic pressure of water are related by an equation of state. As such, cavitation usually occurs when local thermodynamic pressure drops below the vapor pressure causing phase transition, often at a fixed temperature.

Now in the case of QCD matter, equation of state relates, energy density, thermodynamic pressure, temperature and chemical potentials related to conserved quantities like the baryon chemical potential. In absence of a conserved current, which is a good approximation for high energy collisions such as those at the LHC and the $\sqrt{s} = 200$ GeV collision at the RHIC. In this situation, there is a one-to-one relation between thermodynamic pressure and energy density and knowing one uniquely defines the other.

So the phase of QCD matter is determined uniquely by the energy density which is determined uniquely by the thermodynamic pressure. Claiming hadronization at high pressure would be claiming existence of hadron gas at QGP densities, which is not possible. Furthermore, there is not even a possibility of some sort of super-heated hadron

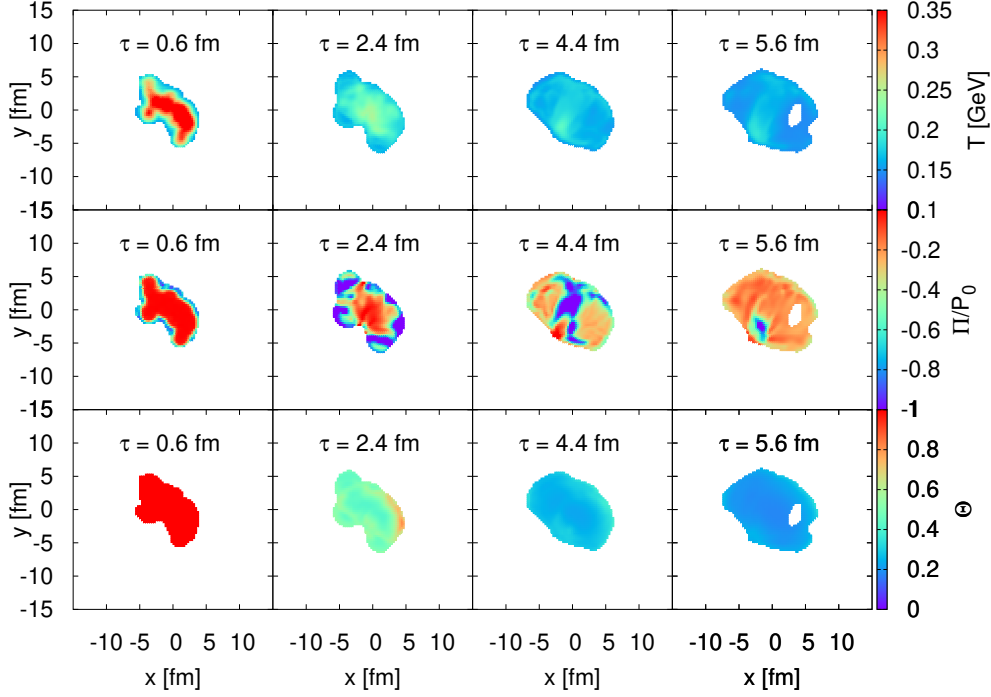


Figure 8.9: Plots showing temperature (top), Π/P_0 (middle) and expansion rate θ (bottom) at different proper times (τ) at midrapidity for a 40-50% centrality Pb-Pb collision at $\sqrt{2.76}$ TeV.

gas as the change between hadron gas and QGP phase at zero chemical potential is a smooth crossover and not a phase transition.

In a nutshell, we should not argue that negative $P_{kin.}$ causes phase change from QGP to hadron gas as phase of QCD material is an equilibrium concept determined by the thermodynamic pressure P_0 . Of course, a negative $P_{kin.}$ is far away from equilibrium, but that in itself cannot determine the phase of the system.

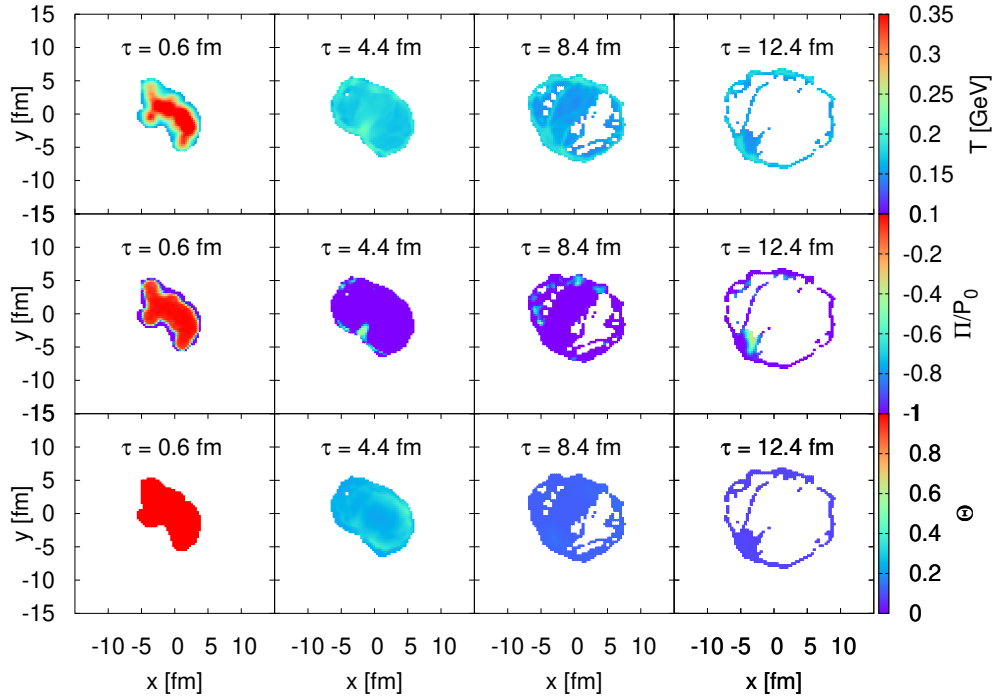


Figure 8.10: Same as fig. 8.9 except ζ/s is 10 times the value reported in eq. (8.1).

8.3.2 Large Π and breaking of the fireball

Then what does large negative Π do? A common notion is that the inward pressure causes the immediate breaking of the fireball. We investigated this scenario.

Fig. (8.9) shows the temperature, Π/P_0 and expansion rate $\theta = \partial_\mu u^\mu$ at different time slices. The regions where $\Pi/P_0 \leq -1$ is depicted in purple color. However, as one notices in the bottom panel, expansion rate never turns negative. Moreover, the hole noticeable in the last panel (at $\tau = 5.6$ fm), is present in regions where magnitude of Π is relatively smaller.

To explore this dynamics further, we simulate an event with an artificially large bulk viscosity. In this case, we take the bulk viscosity to be 10 times the value reported in eq. (8.1). This is done to exaggerate any effect that large negative Π may have. The result

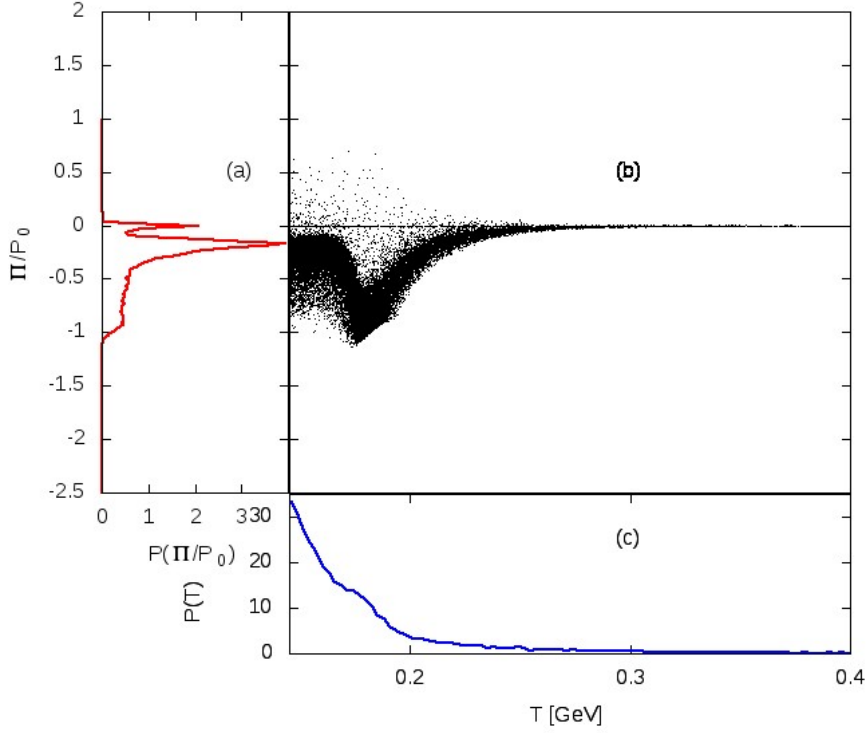


Figure 8.11: Same as fig. 8.3 but with condition $|\Pi| < P_0$ imposed.

is shown in fig. 8.10. Due to exceptionally large bulk viscosity here, much more region in the middle plot is purple denoting more area where $\Pi/P_0 \leq -1$. Here we see that more holes are forming, but still the expansion rate θ never turns negative. It approaches very close to zero, but is still positive definite.

The mechanism of the flow shown in figs. 8.9 and 8.10 can be understood as follows. As Π attains a large negative value, it decelerates the fluid slowing it down. As the fluid slows down, the expansion rate θ drops. As shown in eq. (2.16), Π approaches the value $-\zeta\theta$ with a delay. In Navier-Stokes limit, $\Pi = -\zeta\theta$ is exactly true. So dropping θ implies that Π also drops such that θ never goes negative. In the extreme artificial case shown in fig. 8.10, the fluid cells at temperature close to 180 MeV (where ζ/s is the largest) effectively come to a standstill. At the same time, fluid at lower and higher temperatures keep flowing forming these holes in the liquid.

So the large negative values of Π do cause breakdown of a continuum fluid, though that happens in locations where magnitude of Π is relatively smaller, Also Π/P_0 does not automatically imply phase change from QGP to hadron gas.

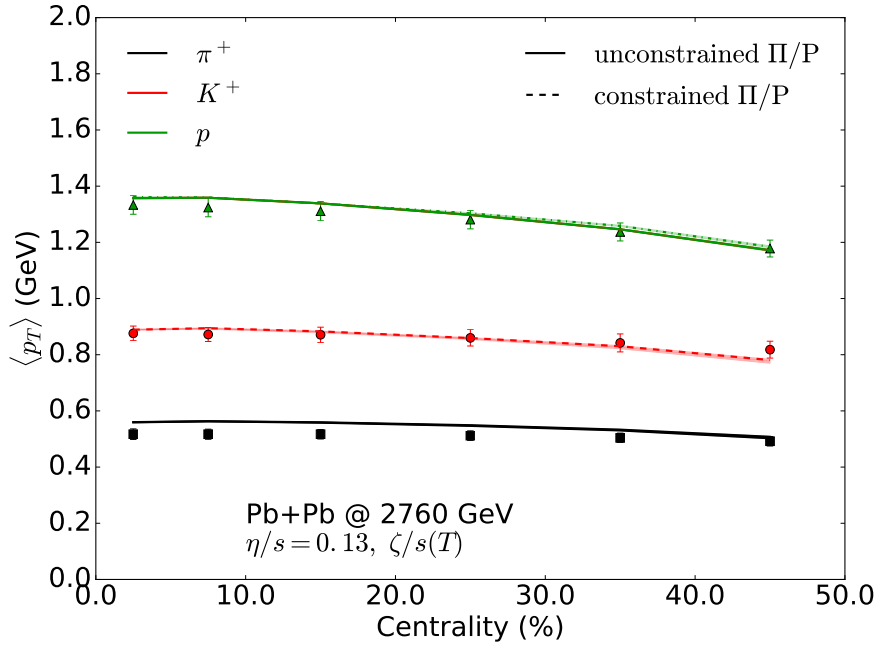


Figure 8.12: Identified particles' mean transverse momentum for Pb-Pb collisions at $\sqrt{s} = 2.76$ TeV with constrained Π . Data points are taken from the ALICE collaboration [161].

8.3.3 Effect of artificially demanding $|\Pi| < P_0$

Finally we look at the question what are the phenomenological consequences of P_{kin} actually going negative. Though not causing phase change, the situation is somewhat off-putting as what was initially assumed to be a correction has turned out to be larger than the zeroth order term. Though we would again like to point out that calling this as breakdown of hydrodynamics would be premature as hydrodynamics has proven to be remarkably resilient and has recently been shown to be valid in situations far from equilibrium [173] Nonetheless, we explore the effects of artificially demanding $|\Pi| < P_0$ in simulations without thermal fluctuations.

Fig. (8.11) shows the scatter plot of Π/P_0 and temperature. This should be looked in conjunction with fig. 8.3. We look at $\langle p_T \rangle$ in fig. 8.12. and find that the cells with $\Pi/P_0 < -1$ do not have any particular effect on the mean transverse momentum, which is the principal observable to detect the effects of bulk viscosity. We also explicitly checked other observables and they showed no effect either.

8.4 SUMMARY

In this chapter, we have explored the qualitative effects of bulk viscous fluctuations. We chose a recipe to implement a particular noise filter based on both the shear and the bulk relaxation times. We observe that as opposed to shear viscous fluctuations, the bulk viscous fluctuations explicitly lower the entropy production and lower the lifetime of the fireball. As a result, particle multiplicities are reduced and $\langle p_T \rangle$ is enhanced. We leave a more comprehensive study using different bulk viscosity profiles present in literature and exploring different noise filters to make a more quantitative conclusion for future work.

We also explored the situation where $P_{kin.}$ pressure turns negative. We argued that this does not imply hadron gas production or immediate fragmentation of the fireball, though it does contribute to the later through a mechanism which we elucidated.

Part III

HARD PARTONS IN QGP

JET MEDIUM RESPONSE

Sec. 2.2 describes the framework we use for light quark jet propagation to evaluate observables described in section 3.4. Most jet propagation models use hydrodynamic information to obtain local temperature. But they usually do not account for the energy lost by jets which is deposited into the soft medium. This is justified by the argument that the energy deposited is a small fraction of net energy in the bulk medium. However, other than the obvious issue of theoretical inconsistency, this can cause problems for observables like the jet-shape function (see section 3.4.2). Jet-shape function describes the momentum distribution in the jet-cone. As the deposited energy diffuses hydrodynamically in the medium, lot of it stays in the cone and cannot be subtracted by removing averaged backgrounds. In simulations, medium response needs to be included. Insightful discussion on this topic can be found in [188, 189].

Energy deposited or picked up by a jet shower can be included as a source term in the hydrodynamics equations in MUSIC (see section 2.1.2.2). This conserves the energy-momentum conservation locally. The source term in the hydrodynamics modifies the equations

$$\partial_\mu T^{\mu\nu} = J^\nu. \quad (9.1)$$

The source term J^ν is negative of the time-differential of the four-momentum density of jet

$$J^\nu = -\frac{dp_{jet}^\nu}{dt d^3x}. \quad (9.2)$$

Note that p_{jet}^ν is a jet parton's four-momentum and dp_{jet}^ν/d^3x is its spatial density. Since $dt d^3x$ is a Lorentz scalar, the whole expression is a Lorentz vector.

9.1 MACH CONES IN QGP

We start by observing the effects of the source terms on the medium evolution with smooth Optical Glauber initial conditions (see section 2.1.1). We initialize hydrodynamics using an ultra-central event with zero impact parameter. We propagate an artificial jet through this. We use the term artificial to signify that we have not used any particular energy loss model or that we have not sampled the jet from any realistic collision model.

This jet moves in a particular direction depositing energy-momentum at each time-step. This deposition is then fed to the hydrodynamics equations using the source term as given in eq. (9.1). We use an energy deposition proportional to the square of local QGP temperature. The artificial jet is moving in the $\pm x$ -direction. Crucially, we are using just a single jet and not a di-jet. The source term is

$$\begin{aligned} J^0 &= T^2/\text{fm}^3, \\ J^1 &= \pm T^2/\text{fm}^3, \\ J^2 &= 0, \\ J^3 &= 0. \end{aligned} \tag{9.3}$$

J^1 is positive when the jet is moving in the $+x$ -direction and negative when the jet is moving in the $(-x)$ -direction.

We use different values of shear viscosity in our events to study the effect of viscosity on the wave-front created by the jets. We are using the conformal fluid dynamics with bulk viscosity zero and ideal gas equation of state.

We expect the passing jet to form Mach cones. Formation of Mach cones is a very familiar process in fluid dynamics which happens when an energetic object moving at speed greater than the speed of sound forms conical wave fronts in the fluid. For the conformal fluid here, the angle of conical wavefront is given by

$$\theta = 2 \sin^{-1}(c_s/c) = 2 \sin^{-1}(1/\sqrt{3}) \equiv 70.5^\circ. \tag{9.4}$$

In figs. 9.1 to 9.3, we look at the energy density differences between events with and without the jets. These show the snapshots of the jet wave-fronts at different times after evolution, with different shear viscosities and with different jet orientations as compared to the underlying event. We unpack the information in these figures here.

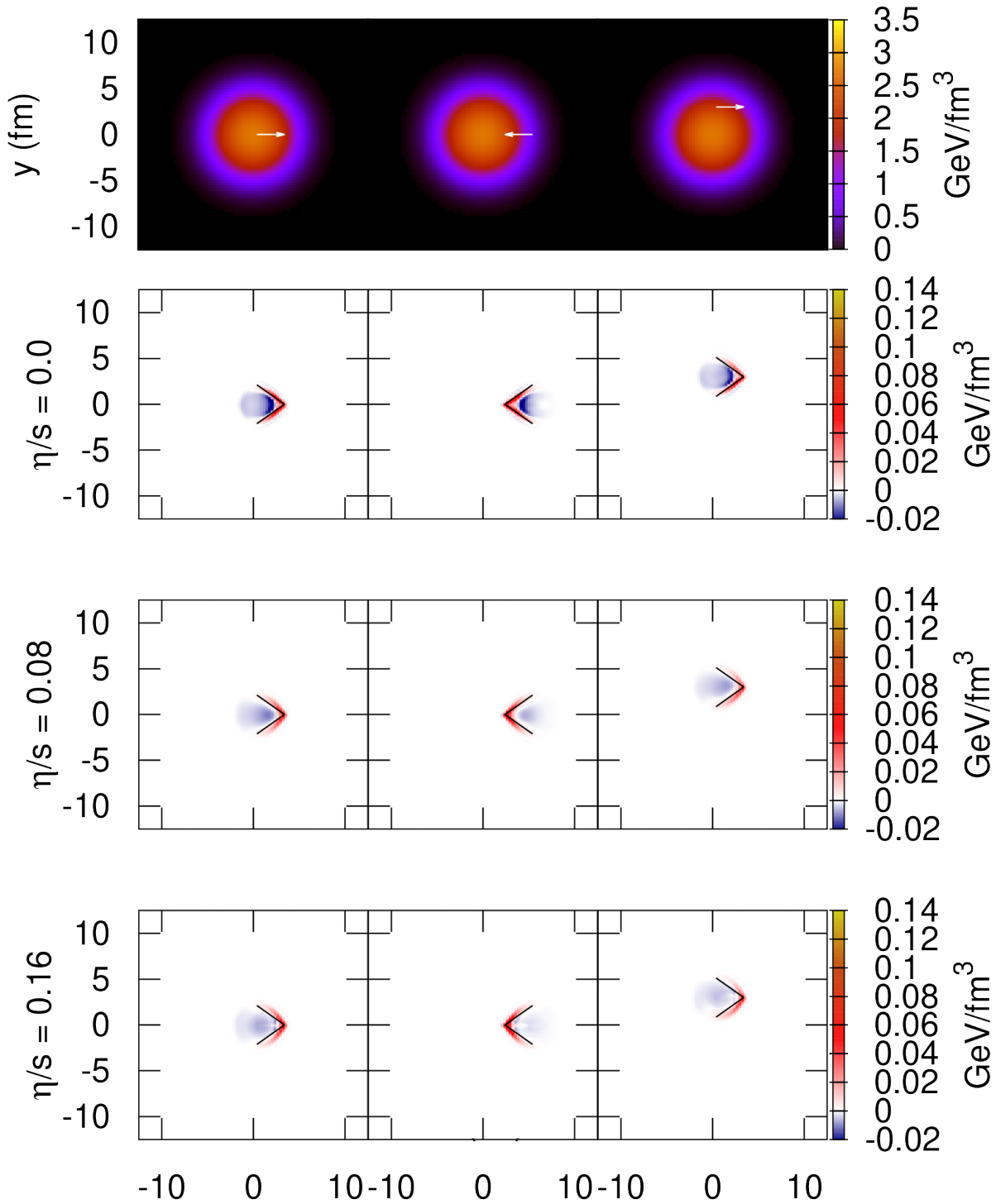


Figure 9.1: Top panel shows the energy density profile with white arrows showing the direction of jet-propagation. Bottom three panels show difference in energy density with and without jets 3 fm/c after the beginning of hydrodynamic evolution for different values of η/s . Black lines indicate the expected wavefront in a static fluid.

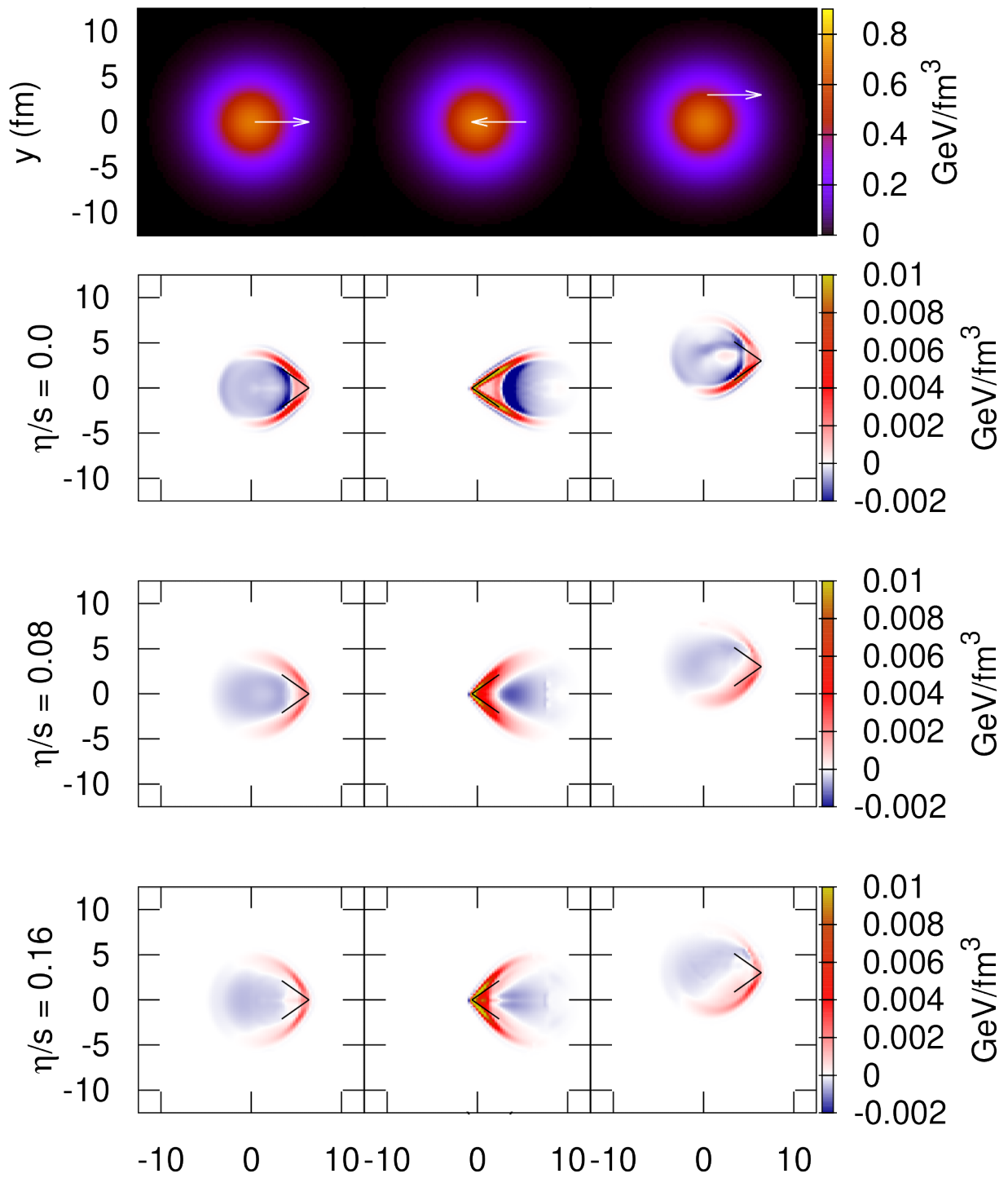


Figure 9.2: Same as fig. 9.1 but 6 fm/c after the beginning of hydrodynamic evolution

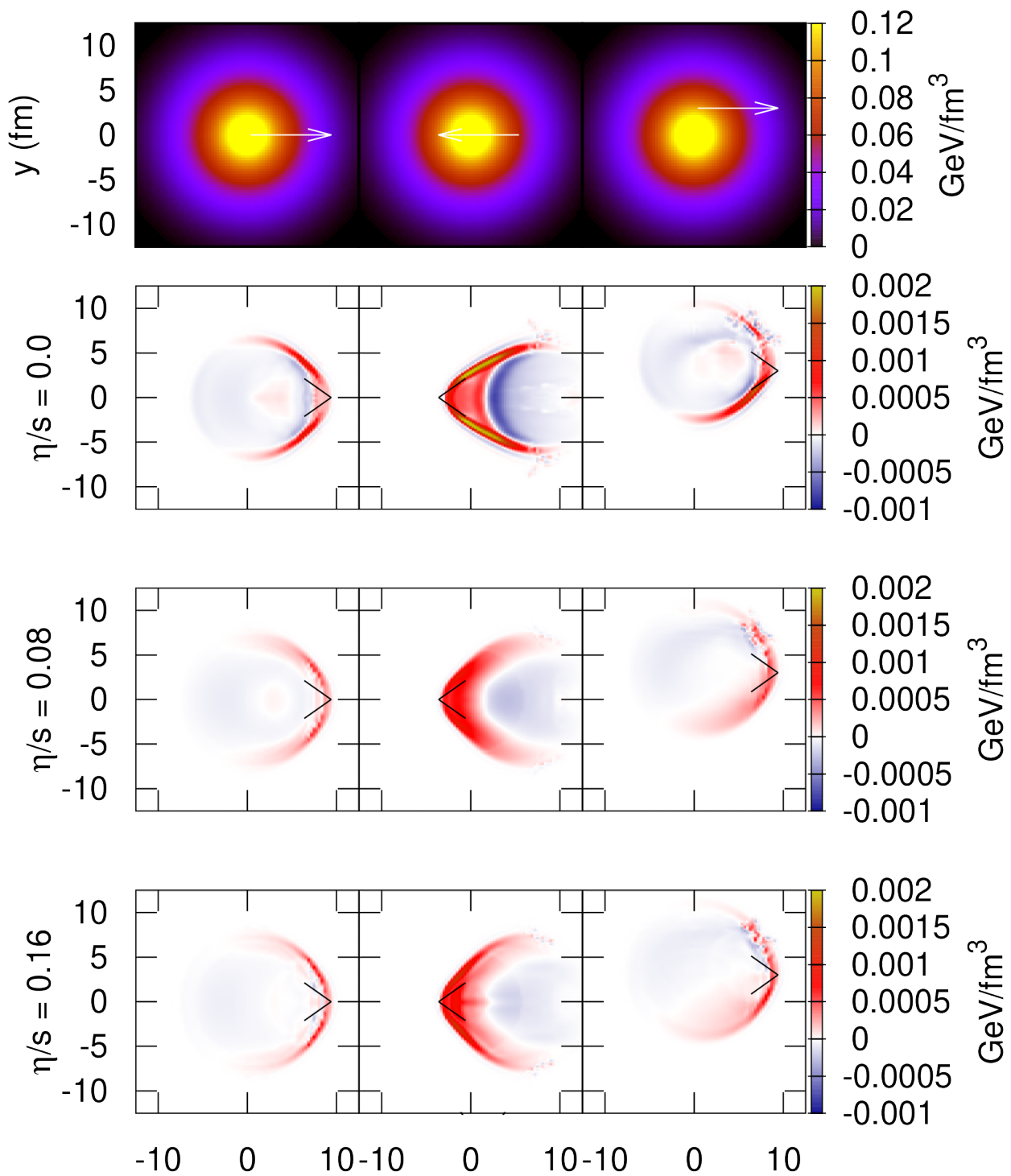


Figure 9.3: Same as fig. 9.1 but 9 fm/c after the beginning of hydrodynamic evolution

9.1.1 *Evolution with time*

We observe that with time, the wake fronts become larger. This is just because the energy deposited earlier gets more time to diffuse. For the same reason, the energy deficit behind region the wake (depicted in blue) becomes larger.

9.1.2 *Effect of jet orientation*

In a fluid at rest, the wakes will have the perfect angle of 70.5° as shown in section 9.1. These shapes are denoted by the black lines in the figure. We could observe that for the first column, where the jet is moving in the direction of underlying flow, the wakes have angle larger than 70.5° . This is because the underlying fluid flow aids the energy diffusion and the wake effectively travels at the speed faster than the speed of the sound.

For the second column, the jet is travelling opposite to the flow of fluid for majority of its evolution. You could notice that the wake angle is smaller than 70.5° for zero viscosity case for snapshots taken 3 and 6 fm/c after the beginning of the event. With viscosity, the wakes for even this orientation spill outside the black lines. This is discussed in section 9.1.3. In the snapshot taken 9 fm/c after the beginning of the evolution as shown in fig. 9.3, the jet has crossed the centre of the fireball and is now moving in the direction of the fluid flow. Hence, we see that even for the zero viscosity case, wake angle is now larger than 70.5° .

In the third columns, we see the jet is moving at an angle to the fluid flow direction. Here the wavefront itself is deformed. The leg of wake perpendicular to the flow direction gets aided by the flow and spreads faster.

9.1.3 *Effect of shear viscosity*

Shear viscosity smooths any sharp edges in the wavefronts and also disperses the energy making the wakes more diffused. Higher the shear viscosity, smoother the Mach cones we observe.

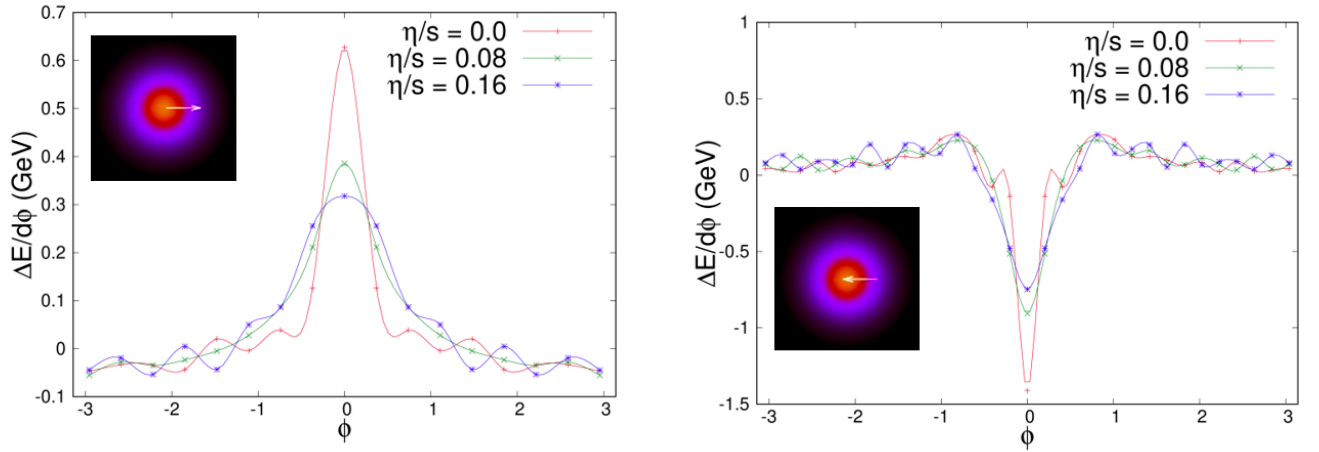


Figure 9.4: Difference in energy flux through the freezeout surface of events with and without jets. Inset denotes the orientation of the jet with respect to the underlying fireball.

9.2 ENERGY ENHANCEMENT AT THE FREEZEOUT SURFACE

While our analysis of the jet wakes helps us understand the dynamics of medium response of the jets, these wakes cannot be observed directly in experiments. They account for small enhancement of particle multiplicities in the immediate neighbourhood of identified jets. This enhancement is difficult to subtract, and is part of the reconstructed jets.

To explore how these wakes contribute to the enhancement in particle multiplicities, we study their constant temperature freezeout surfaces. Fig. 9.4 shows the enhancement in the energy flux through the isothermal freezeout surface.

The left panel in fig. 9.4 is for the outward jet. It shows enhancement in energy flux around $\phi = 0$ which directly translates to enhancement in multiplicity in that region. We observe that the enhancement is diffused for viscous systems with higher viscosity contributing to broader and shorter peaks. Also, there is an energy deficit around $\phi = \pi$ which is the consequence of fluid being dragged with the jet towards $\phi = 0$ direction.

For the inward jet shown in the right panel of fig. 9.4, there is a deficit around $\phi = 0$ which is self-explanatory. Similar to the outward jet, the deficit dip is more diffused for viscous systems.

Fig. 9.5 is more interesting. In a real event, the underlying flow is not smooth and symmetrical. Also, jets are randomly aligned and not correlated with the underlying

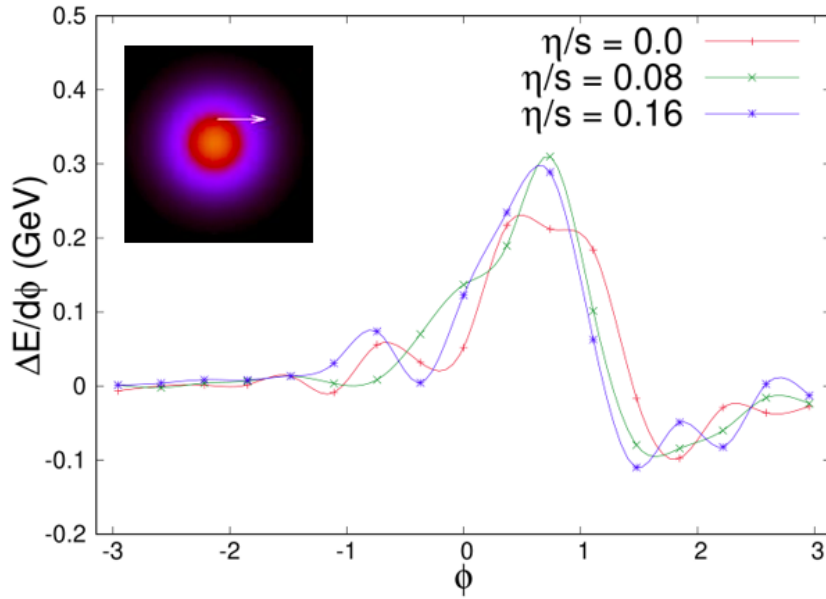


Figure 9.5: Same as fig. 9.4 for a different jet orientation.

flow. So, a jet at an angle with the fluid velocity is a more accurate representation of a real jet. Here, the relation between the final energy enhancement and the viscosity of the system is not very clear. So it will be very difficult to use medium response of jets to constrain the viscosity of QGP.

We now move to utilise our implementation of jet induced energy sources in hydrodynamics to study jet physics. But first, we need to check the accuracy of the energy momentum conservation in our framework.

9.3 TESTING ENERGY CONSERVATION

Energy deposited by hard particles is usually a very small fraction of the total energy of the fireball. Of course, it is still crucial to include this effect in a jet-medium interaction model as this energy is largely localized in a narrow cone around the jet as we saw in chapter 9.

We tracked the net energy deposited by a jet in the medium during the evolution. We also evaluated the net energy in the initial state. Finally, we compared the sum of these two numbers to the net energy-density flux through the freezeout surface.

We are able to recover the total energy to high precision ($\sim 0.1\%$), provided we used a very fine meshing during the freezeout procedure. Freezeout surface generation effectively consists of making patches of the constant temperature surface. If we make too large patches, the precision goes down. On the other hand, making very small patches is computationally expensive.

So, effectively we have to go to very fine meshing to recover the tiny amount of energy-momentum deposited by the jets. Using a coarse mesh (of the order that we typically use) makes it difficult to resolve this tiny amount of energy. But we argue that this should not be a problem for our calculations as most of the energy is concentrated around the jet and it is a much more significant effect in that local region. And our tests have shown that MUSIC does a good job of energy conservation even with the added sources.

9.4 SECOND PASS FRAMEWORK

Typically in jet-quenching calculations in heavy-ion collisions, the medium is evolved independent of jets. The entire space-time history of the medium is saved. Jets passing through the medium get local temperature information from this evolution history data.

One way to study the jet-medium response is to keep a record of energy momentum changes of the jets and simulate the medium again using this information for getting source terms using eq. (9.2). This is called the second-pass method.

This works for hard jets as they effectively move at the speed of light. Also, it is very unlikely to get more than one di-jet pair in a single event. Consequently, a jet never sees the effects of the energy it deposits in the medium. In other words, there is no feedback from the medium response to the jet.

Fig. 9.6 shows the evolution history of a second pass run. We used the hybrid model [76]. to simulate the energy loss. The figure shows the typical wake evolution as a consequence of a hard di-jet passing through the medium.

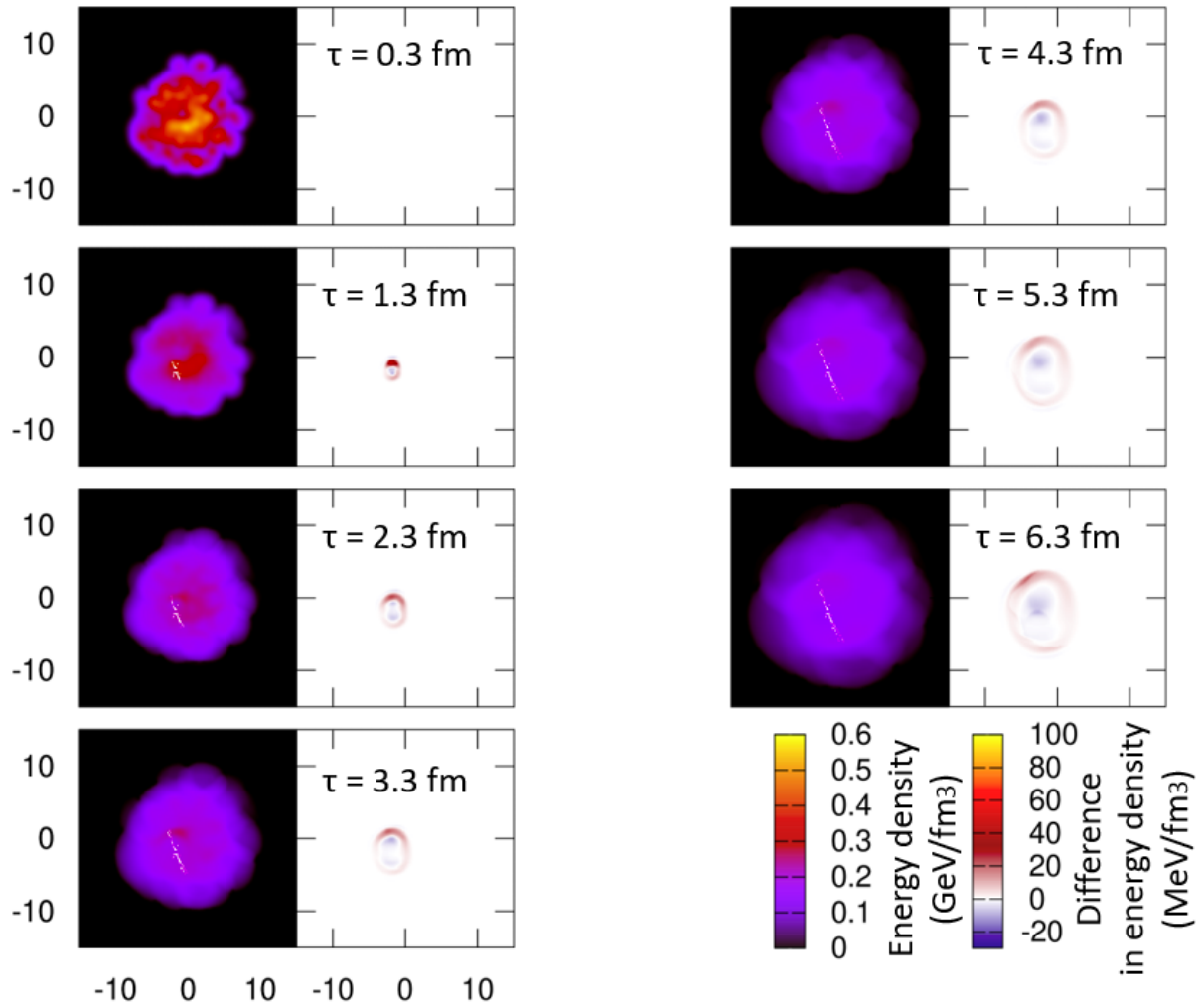


Figure 9.6: Energy density (left panels) and difference in energy density because of jets (right panels) in a Pb-Pb collision at $\sqrt{s} = 2.76$ TeV. Jet energy loss is modelled by the hybrid model [76]. White dots denote the location of energy deposition.

9.5 STANDARDIZING CONCURRENT FRAMEWORK

Moving beyond the second pass method, we have developed a joint hybrid-model-MUSIC framework where a jet is evolved simultaneously with the evolution of the underlying fluid.

For the hydro-sector, we initialize using IP-Glasma [40, 41]. The IP-Glasma to MUSIC switch is made at $\tau = 0.4$ fm. Lattice QCD based equation of state is used [15] which is matched with hadron resonance gas based equation of state [159]. A temperature dependent bulk viscosity used in [65] is used.

Jets are sampled at the binary collision hotspots. These are the same hotspots which gives rise to IP-Glasma initial conditions on an event-by-event basis. PYTHIA [190] is used to sample jets. Jets propagate in vacuum until $\tau = 0.4$ fm.

From $\tau = 0.4$ fm, jets and fluid evolve simultaneously using the hybrid model and MUSIC respectively. Hybrid model gets local hydrodynamic information from MUSIC while MUSIC gets information about the energy-momentum source terms from hybrid model. While both MUSIC and hybrid model have existed for some time (see chapter 2), their concurrent framework is implemented here for the first time.

At the end, when the jet particles leave the QGP medium and when the temperature throughout the medium drops below the freezeout temperature (145 MeV), partons are hadronized. Jet partons are hadronized using the Lund String Model [83] encoded in PYTHIA [190]. Soft partons are sampled from the freezeout surface for pairing. This negative energy contribution on the freezeout surface of AA collisions is negligible. A recent update to Lund model [84] gives the momentum and spatial information about the hadrons. We do not decay the hadrons in PYTHIA.

The freezeout surface from MUSIC is hadronized using the Cooper-Frye prescription using the publicly available code iSS [72].

Finally, the hadrons from PYTHIA and those from iSS are listed together and fed to UrQMD [74, 75] afterburner. UrQMD simulates resonance decays and hadronic rescatterings until the system reaches kinetic freezeout.

Particles at the end of kinetic freezeout, sourced from both the soft and hard sources, are analyzed for observables.

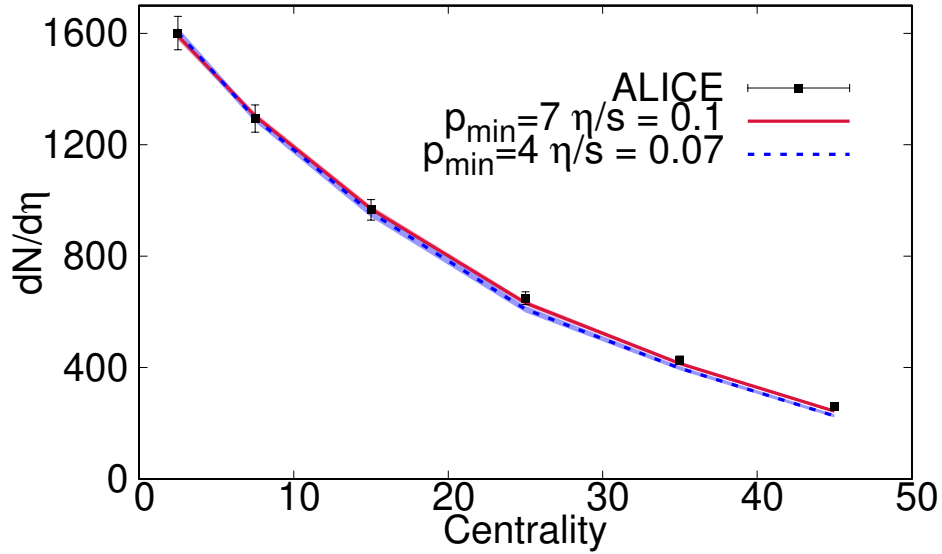


Figure 9.7: Charged hadron multiplicity for Pb-Pb collisions at $\sqrt{s} = 2.76$ TeV with different value of p_{min} . Data points are taken from the ALICE collaboration [91]. Both the parameter sets have different energy normalizations.

9.5.1 Choosing minimum jet momentum for minijets

We aim to evolve minijets along with QGP to approach the elusive intermediate p_T region. As such, it becomes critical as to what is our minimum allowed momentum for a minijet. This minimum jet momentum p_{min} is a parameter of our model.

We want to emphasize that a concurrent jet-medium framework is essential to study intermediate p_T physics. There are many intermediate p_T mini-jets in every event. They contribute significant amount of energy to the medium and hence medium response is crucial. Also, their responses affect one another and so second pass framework is not sufficient.

We observe that if we choose a very small value of p_{min} , we cannot fit the data in the soft sector with reasonable parameters. Fig. 9.7 shows the charged hadron multiplicities. The choice of η/s for different values of p_{min} will become clear momentarily. In fig. 9.7 we see that both the parameter sets have been appropriately normalized to match the multiplicity data.

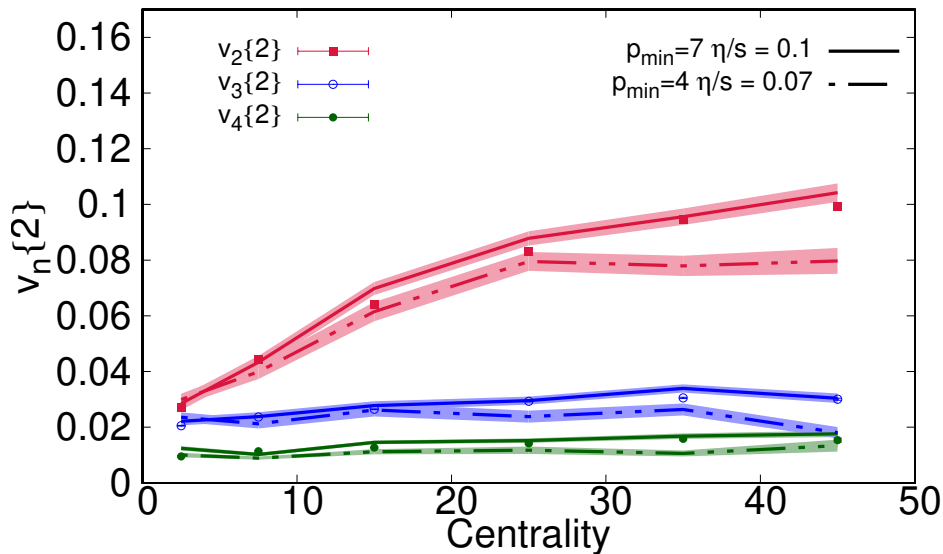


Figure 9.8: Charged hadron integrated v_n for Pb-Pb collisions at $\sqrt{s} = 2.76$ TeV with different value of p_{min} . Data points are taken from the ALICE collaboration [162].

In fig. 9.8, we observe that $\eta/s = 0.1$ for $p_{min} = 7$ GeV fits the integrated v_n data quite well while a lower value of $\eta/s = 0.07$ fails to fit the data for $p_{min} = 4$ GeV. A lower value of shear viscosity leads to higher value of v_n s. $\eta/s = 0.07$ is already below the lower KSS bound of $1/4\pi$ [153].

Our model is unable to explain the soft-sector data for $p_{min} = 4$ GeV while the optimum value of η/s for $p_{min} = 7$ GeV is 0.1.

9.6 SUMMARY

We added a source term to hydrodynamic evolution equation and qualitatively studied the dynamics of jet medium response. We observed how the Mach cones are generated. We also studied the characteristics of jet cones as functions of evolution time, jet orientation and shear viscosity of the fluid.

We see that the energy deposited to the fluid by jet leads to enhancement or suppression of energy flux which will lead to increased multiplicity in the jet cone. Finally, our

analysis shows that it would be very difficult to only use jet-shape function to extract QGP viscosity.

We have prepared the framework for simultaneous evolution of jets and medium. We have started with the simple hybrid model of jet-quenching, but this could be replaced by any desired model.

We have developed a procedure to set model parameter values for different values of p_{min} to match the soft-sector data. We observed that the QGP transport coefficients need to be recalibrated when we introduce minijets in simulations. Now the goal is to look at differential observables at intermediate p_T and see what parameter values best explain data for a given energy loss model. This will provide us insight into energy loss mechanisms. This is left for future work.

CHARM QUARKS IN QGP

In the last chapter, our focus was on light parton jets. In this chapter, we finally close by analysing a heavy-quark jet interaction with QGP. We will focus on the charm quarks though a similar analysis could be performed for bottom quarks as well.

Charm quark jets usually do not thermalize within the QGP and form heavy baryons and mesons upon hadronization [191–193]. These provide insights into the QGP phase by observables such as the nuclear modification factor R_{AA} and v_n . These are also responsible for the dilepton signals coming from the open charm decays. See section 3.5 for details.

As charm quarks are much heavier than the QGP temperature, we can treat charm quark dynamics in QGP as Brownian motion [194, 195]. This model was described in section 2.3. There we also described the framework to evaluate the drag and diffusion coefficients of HQ in QGP, which are fundamental properties of the system.

10.1 CHARM TRANSPORT COEFFICIENTS

Here we go ahead and complete the calculation done in [87] and extended in [196]. We go further ahead and calculate the non-equilibrium effects on HQ drag and diffusion. We also estimate the energy loss an HQ will undergo in QGP. This work has been published in [197].

From eqs. (2.44) to (2.46) we have

$$A = \langle\langle 1 \rangle\rangle - \langle\langle \mathbf{p} \cdot \mathbf{p}' \rangle\rangle / p^2, \quad (10.1)$$

$$B_0 = \frac{1}{4} \left[\langle\langle p'^2 \rangle\rangle - \langle\langle (\mathbf{p} \cdot \mathbf{p}')^2 \rangle\rangle / p^2 \right], \quad (10.2)$$

$$B_1 = \frac{1}{2} \left[\langle\langle (\mathbf{p} \cdot \mathbf{p}')^2 \rangle\rangle / p^2 - 2 \langle\langle \mathbf{p} \cdot \mathbf{p}' \rangle\rangle + p^2 \langle\langle 1 \rangle\rangle \right], \quad (10.3)$$

with the notation $\langle\langle \rangle\rangle$ defined in eqs. (2.40) and (2.41)

$$\begin{aligned} \langle\langle (\mathbf{p})_i \rangle\rangle &\equiv \frac{1}{\gamma_c} \frac{1}{2P^0} \int \frac{d^3 \mathbf{q}}{(2\pi)^3 2Q^0} \int \frac{d^3 \mathbf{p}'}{(2\pi)^3 2P'^0} \int \frac{d^3 \mathbf{q}'}{(2\pi)^3 2Q'^0} \\ &\times (2\pi)^4 \delta^4(P + Q - P' - Q') \sum |\mathcal{M}_{HQ,g/q}|^2 \\ &\times f_{g/q}(Q) \left(1 \pm f_{g/q}(Q')\right) (\mathbf{p})_i. \end{aligned} \quad (10.4)$$

Here A , B_0 and B_1 are the drag, transverse diffusion and longitudinal diffusion coefficients respectively. The interaction taking place is $HQ(p) + l(q) \rightarrow HQ(p') + l(q')$. Following the procedure in [196] we can simplify the integral by moving to the centre of momentum frame

$$\begin{aligned} \langle\langle F(p') \rangle\rangle &= \frac{1}{512\pi^4 \gamma_c} \frac{1}{E_p} \int_0^\infty \frac{q^2}{E_q} dq \int_{-1}^1 d \cos \chi \\ &\times f_{g/q}(E_q) \frac{\sqrt{(s + m_c^2 - m_{g/q}^2)^2 - 4sm_c^2}}{s} \int_{-1}^1 d \cos \theta_{cm} \\ &\times \sum |\mathcal{M}_{HQ,g/q}|^2 \int_0^{2\pi} d\phi_{cm} e^{\beta E_{q'}} f_{g/q}(E_{q'}) F(p'). \end{aligned} \quad (10.5)$$

Here $s = (E_p + E_q)^2 - (\mathbf{p} + \mathbf{q})^2$ and $E_{q'} = E_p + E_q - E_{p'}$. HQ momentum after scattering p' is represented in terms of p , q , θ_{cm} and ϕ_{cm} . m_c is the charm mass and $m_{g/q}$ is the thermal mass of the gluons/quarks. They are given as

$$m_g^2 = \left(1 + \frac{N_f}{6}\right) \frac{g^2 T^2}{3}, \quad (10.6)$$

$$m_q^2 = \frac{3}{2} \frac{g^2 T^2}{9} \quad (10.7)$$

where we have assumed chemically equilibrated quarks and gluons. N_f is the number of light flavors.

We have taken light flavor number $N_f = 2.5$, charm mass $m_c = 1.5$ GeV and strong coupling $\alpha_s = 0.3$. Finally Debye screening mass $\mu_D = \sqrt{4\pi\alpha_s}T$ is used in gluon propagators of the t-channel exchange diagrams in fig. 2.2.

10.2 SHEAR VISCOUS CORRECTION

Viscous correction to transport coefficients given in eqs. (10.1) to (10.3) appears at two places, the parton distribution functions and the Debye screening mass. Following the procedure used in [71], distribution function is given as

$$f_{g/q}(Q, X) = f_{g/q}^0(Q) + \delta f_{g/q}(Q, X). \quad (10.8)$$

Shear correction here is given as

$$\delta f_{g/q}(Q, X) = \pi_{\mu\nu} Q^\mu Q^\nu S_X(X) S_M(Q, T). \quad (10.9)$$

Here

$$S_X = \frac{1}{2(\varepsilon + P)}, \quad S_M = \frac{f_{g/q}^0(q)(1 \pm f_{g/q}^0(q))}{T^2}, \quad (10.10)$$

and ε and P are local hydrodynamic quantities. This shear correction is evaluated using the Grad's 14 moment method and is identical to the form given in eq. (2.34).

Linearizing eq. (2.40) in $\delta f_{g/q}$ we can write

$$A_i \simeq A_i^{(0)} + A_i^{\text{shear}}. \quad (10.11)$$

Shear viscous contribution A_i^{shear} is

$$\begin{aligned} A_i^{\text{shear}} &= \frac{1}{\gamma_c} \frac{1}{2P^0} \int \frac{d^3 \mathbf{q}}{(2\pi)^3 2Q^0} \int \frac{d^3 \mathbf{p}'}{(2\pi)^3 2P'^0} \int \frac{d^3 \mathbf{q}'}{(2\pi)^3 2Q'^0} (2\pi)^4 \delta^4(P + Q - P' - Q') \\ &\quad \times \sum |\mathcal{M}_{HQ,g/q}|^2 \left[\delta f_{g/q}(Q) (1 \pm f_{g/q}^0(Q')) \pm f_{g/q}^0(Q) \delta f_{g/q}(Q') \right] (\mathbf{p} - \mathbf{p}')_i, \end{aligned} \quad (10.12)$$

which can be written as

$$A_i^{\text{shear}} = \pi_{\mu\nu} P^\mu P^\nu \sum_j S_X^j(X) \bar{S}_M^j(P, T), \quad (10.13)$$

with

$$\begin{aligned}
\bar{S}_M^j(P, T) &= \frac{1}{2[(u.P)^2 - P^2]} \left[g^{\mu\nu} + \frac{P^2 + 2(u.P)^2}{[(u.P)^2 - P^2]} u_\mu u_\nu + 3 \frac{P^\mu P^\nu}{[(u.P)^2 - P^2]} \right. \\
&\quad \left. - 3 \frac{(u.P)}{[(u.P)^2 - P^2]} (P^\mu u^\nu + P^\nu u^\mu) \right] \frac{1}{\gamma_c} \frac{1}{2P^0} \int \frac{d^3 \mathbf{q}}{(2\pi)^3 2Q^0} \int \frac{d^3 \mathbf{p}'}{(2\pi)^3 2P'^0} \\
&\quad \times \int \frac{d^3 \mathbf{q}'}{(2\pi)^3 2Q'^0} (2\pi)^4 \delta^4(P + Q - P' - Q') (\mathbf{p} - \mathbf{p}')_i \sum | \mathcal{M}_{HQ,g/q} |^2 \\
&\quad \times \left[Q^\mu Q^\nu S_M^j(Q, T) \left(1 \pm f_{g/q}^0(Q') \right) \pm f_{g/q}^0(Q) Q'^\mu Q'^\nu S_M^j(Q', T) \right]. \quad (10.14)
\end{aligned}$$

$\bar{S}_M^j(P, T)$ is a scalar which depends only on HQ momentum and temperature and the shear contribution has been completely factored out in eq. (10.13). Using this simplification we finally obtain the shear correction to the integral in eq. (10.5)

$$\langle \langle F(p') \rangle \rangle^{\text{shear}} = \pi_{\mu\nu} P^\mu P^\nu \frac{1}{(\varepsilon + P)} \frac{1}{T^2} \frac{1}{512\pi^4 \gamma_c} \frac{1}{4E_p p^2} \left[\Gamma_1(p, T) \pm \Gamma_2(p, T) \right], \quad (10.15)$$

with

$$\begin{aligned}
\Gamma_1 &= \int_0^\infty \frac{q^2}{E_q} dq \int_{-1}^1 d \cos \chi \frac{\sqrt{(s + m_c^2 - m_{g/q}^2)^2 - 4sm_c^2}}{s} f_{g/q}^0(E_q) \left(1 \pm f_{g/q}^0(E_q) \right) \\
&\quad \times \left[m_{g/q}^2 + 3q^2 \cos^2 \chi - E_q^2 \right] \int_{-1}^1 d \cos \theta_{cm} \sum | \mathcal{M}_{HQ,g/q} |^2 \int_0^{2\pi} d\phi_{cm} e^{\beta E_{q'}} f_{g/q}(E_{q'}) F(p'), \quad (10.16)
\end{aligned}$$

and

$$\begin{aligned}
\Gamma_2 &= \int_0^\infty \frac{q^2}{E_q} dq \int_{-1}^1 d \cos \chi \frac{\sqrt{(s + m_c^2 - m_{g/q}^2)^2 - 4sm_c^2}}{s} f_{g/q}^0(E_q) \int_{-1}^1 d \cos \theta_{cm} \sum | \mathcal{M}_{HQ,g/q} |^2 \\
&\quad \times \int_0^{2\pi} d\phi_{cm} \left(1 \pm f_{g/q}(E_{q'}) \right) f_{g/q}(E_{q'}) \left[m_{g/q}^2 + \frac{3}{p^2} (p^2 + pq \cos \chi - (\mathbf{p} \cdot \mathbf{p}'))^2 - E_{q'}^2 \right] F(p'). \quad (10.17)
\end{aligned}$$

Shear tensor is traceless and ultimately does not contribute to Debye screening mass. The details can be seen in [197].

Finally, the shear contribution to drag and diffusion coefficients can be calculated from eqs. (10.1) to (10.3) with the integrals defined in eqs. (10.15) to (10.17).

10.3 BULK VISCOUS CORRECTIONS

Chapman-Enskog expansion within relaxation time approximation gives a bulk viscous correction to particle distribution function

$$\begin{aligned} \delta f_{g/q}(Q, X) &= -\beta f_{g/q}^0(Q) \left(1 \pm f_{g/q}^0(Q)\right) \left(E_q - \frac{m_{g/q}^2}{E_q}\right) \\ &\quad \times \left(c_s^2 - \frac{1}{3}\right) \frac{\Pi(X)}{(\zeta/\tau_R)}, \end{aligned} \quad (10.18)$$

where

$$\frac{\zeta}{\tau_R} \approx 15 \left(\frac{1}{3} - c_s^2\right)^2 (\varepsilon + P). \quad (10.19)$$

This bulk correction is slightly different from the expression given in eq. (2.35). Expression in eq. (2.35) was used for hadrons. Here we are in the QGP phase. Quarks and gluons in QGP acquire a thermal mass modifying the bulk correction. The derivation of this form can be seen in [71].

We follow the same procedure outlined in section 10.2 with this correction in distribution function. The detailed derivation can be seen in [197]. We quote the final result here. The bulk viscous correction to the integral is given as

$$\langle\langle F(p') \rangle\rangle^{\text{bulk}} = \frac{\Pi B_X(X)}{512\pi^4 \gamma_c} \frac{1}{E_p} \left[\Lambda_1(p, T) \pm \Lambda_2(p, T) \right], \quad (10.20)$$

where,

$$\begin{aligned} \Lambda_1 &= \int_0^\infty \frac{q^2}{E_q} dq \int_{-1}^1 d \cos \chi \frac{\sqrt{(s + m_c^2 - m_{g/q}^2)^2 - 4sm_c^2}}{s} B_M(Q, T) \int_{-1}^1 d \cos \theta_{cm} \sum | \mathcal{M}_{HQ,g/q} |^2 \\ &\quad \times \int_0^{2\pi} d\phi_{cm} e^{\beta E_{q'}} f_{g/q}(E_{q'}) F(p'), \end{aligned} \quad (10.21)$$

and

$$\begin{aligned} \Lambda_2 &= \int_0^\infty \frac{q^2}{E_q} dq \int_{-1}^1 d \cos \chi \frac{\sqrt{(s + m_c^2 - m_{g/q}^2)^2 - 4sm_c^2}}{s} f_{g/q}^0(E_q) \int_{-1}^1 d \cos \theta_{cm} \sum | \mathcal{M}_{HQ,g/q} |^2 \\ &\quad \times \int_0^{2\pi} d\phi_{cm} B_M(Q', T) F(p'). \end{aligned} \quad (10.22)$$

Unlike shear viscosity, bulk viscous corrections modify Debye screening mass. Debye mass comes from the gluon self energy and is given by

$$\mu^2 = 4\pi\alpha_s\beta \int \frac{d^3\mathbf{q}}{(2\pi)^3} \left[2N_c f_g(1 + f_g) + 2N_f f_q(1 - f_q) \right], \quad (10.23)$$

where N_c is the number of colors, and as before, N_f is the number of flavors. Consequently, correction to the Debye mass is given by

$$\delta\mu^2 = 4\pi\alpha_s\beta \int \frac{d^3\mathbf{q}}{(2\pi)^3} \left[2N_c\delta f_g(1 + 2f_g^0) + 2N_f\delta f_q(1 - 2f_q^0) \right]. \quad (10.24)$$

Now, Debye mass appears only in t-channel diagrams given as

$$|\mathcal{M}_{HQ,q}|^2 = 256N_f\pi^2\alpha_s^2 \frac{(m_c^2 - s)^2 + (m_c^2 - u)^2 + 2m_c^2t}{(t - \mu^2)^2}. \quad (10.25)$$

Here s , t and u are Mandelstam variables. Up to leading order in Debye mass corrections, we can expand the matrix element

$$|\bar{\mathcal{M}}_{HQ,q}|^2 = |\mathcal{M}_{HQ,q}|^2 + |\mathcal{M}_{HQ,q}|^{2(1)}, \quad (10.26)$$

with

$$|\mathcal{M}_{HQ,q}|^{2(1)} = 512N_f\pi^2\alpha_s^2 \delta\mu^2 \frac{(m_c^2 - s)^2 + (m_c^2 - u)^2 + 2m_c^2t}{(t - \mu^2)^3}. \quad (10.27)$$

This gives an additional term in bulk viscous correction. Following the same procedure as before as described in section 10.2, we finally get

$$\langle\langle F(p') \rangle\rangle^{\text{bulk}(2)} = \Pi B_X(X) \frac{1}{512\pi^4\gamma_c} \frac{1}{E_p} \Lambda_3(p, T), \quad (10.28)$$

with

$$\begin{aligned} \Lambda_3 = & \frac{2\alpha_s}{\pi T} \int_0^\infty \frac{q^2}{E_q} dq \int_{-1}^1 d\cos\chi \frac{\sqrt{(s + m_c^2 - m_q^2)^2 - 4sm_c^2}}{s} f_q^0(E_q) \int_{-1}^1 d\cos\theta_{cm} |\mathcal{M}_2|^2 \\ & \times \int_0^{2\pi} d\phi_{cm} e^{\beta E_{q'}} f_q(E_{q'}) F(p') \int_0^\infty r^2 dr \left[2N_{c/f} B_M(R, T) \left(1 \pm 2f_{g/q}^0(E_r) \right) \right]. \quad (10.29) \end{aligned}$$

Now we have everything we need to evaluate the bulk correction to HQ transport coefficients. The corrections are given by eqs. (10.1) to (10.3) with integral given by sum of two terms. Those two terms are given by eqs. (10.20) to (10.22) and eqs. (10.28) and (10.29).

10.4 RESULTS

We use MUSIC [32] to simulate a 0 – 5% centrality $Pb - Pb$ collision event with IP-Glasma initial conditions [40, 41] and hotQCD equation of state [15] matched to hadron

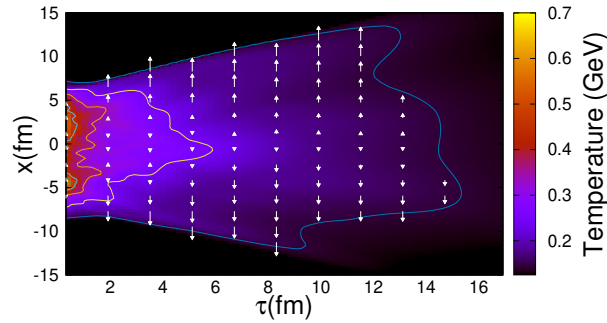


Figure 10.1: Temperature evolution along $y = 0$ axis at mid-rapidity. White arrows indicate local flow.

resonance gas equation of state [159] is used. In choosing fluctuating initial conditions, our goal here is not to get averaged observables from event-by-event simulations but to obtain insight into how HQ transport quantities look like in a realistic HIC event.

Fig. 10.1 shows temperature evolution history along the $y = 0$ line at midrapidity. The drag and diffusion coefficients given in eqs. (10.1) to (10.3) are solved numerically with the hydrodynamic information folded in. We used a Monte-Carlo integrator to evaluate these integrals.

We place a charm quark with momentum $p = 5$ GeV moving in positive x -direction on the $y = 0$ line at midrapidity. The momentum is defined such that charm four momentum is $p = (\sqrt{m_c^2 + p^2}, p, 0, 0)$ in lab frame. We are not dynamically evolving the charm but actually placing it with the exact same momentum at each (τ, x) depicted in fig. 10.1.

Fig. 10.2 shows the drag coefficient. Drag coefficient is larger when the temperature is higher. Charm faces less random kicks in its Brownian motion at lower temperatures. It is also higher on the lower half of the plane. HQ loses more energy by drag when it is travelling opposite to the direction of medium flow.

Fig. 10.3 shows the value of diffusion coefficients. As opposed to drag, there is more diffusion when charm moves in the direction of medium velocity.

Fig. 10.4 shows the ratio of viscous corrections to the equilibrium values. Shear corrections are prominent at early temperatures. Bulk correction is negative and could be up

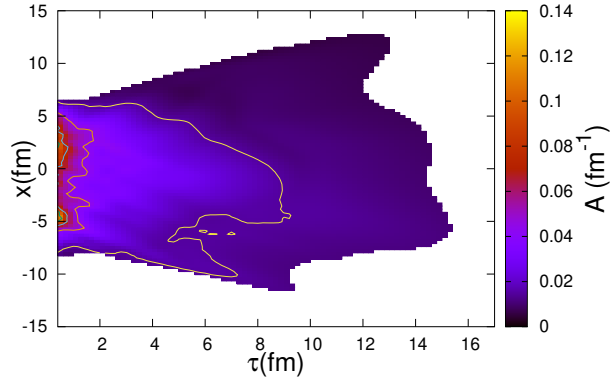


Figure 10.2: Drag coefficients of a charm with $p = (\sqrt{m_c^2 + p^2}, p, 0, 0)$ in lab frame at each space-time point. Curves indicate constant value contours.

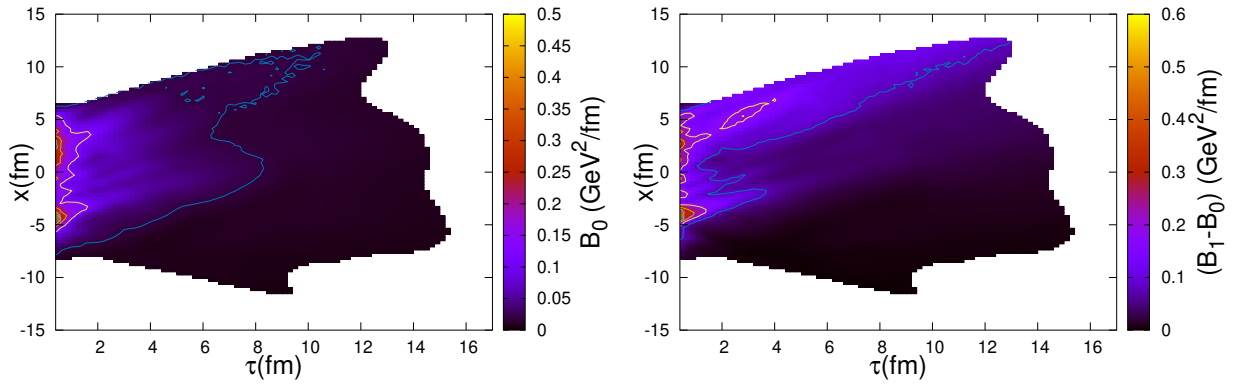


Figure 10.3: Diffusion coefficients B_0 (left) and $B_1 - B_0$ (right) of a charm with $p = (\sqrt{m_c^2 + p^2}, p, 0, 0)$ in lab frame at each space-time point. Curves indicate constant value contours.

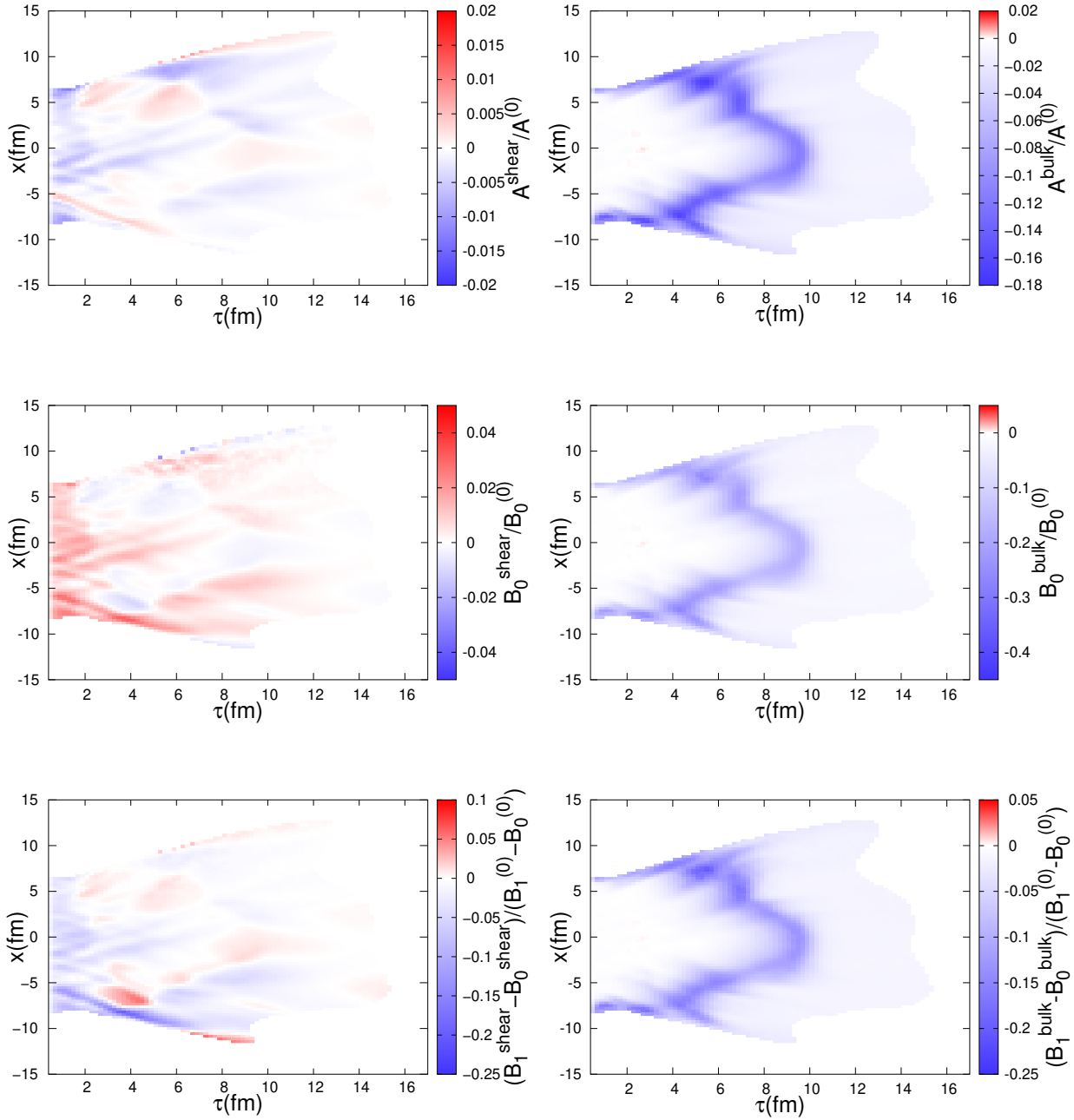


Figure 10.4: Ratio of shear (left) and bulk (right) viscous corrections to the equilibrium values for A (top), B_0 (middle) and $(B_1 - B_0)$ (bottom). Charm properties are same as in figs. 10.2 and 10.3.

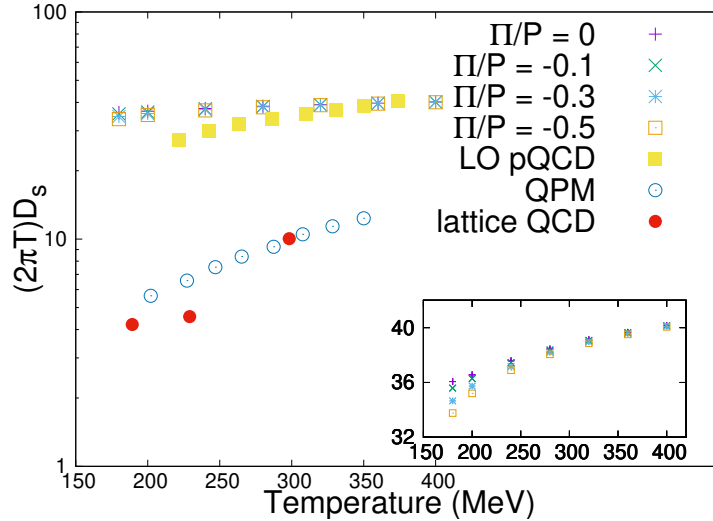


Figure 10.5: Spatial diffusion coefficient calculated in present work compared with estimations from LO pQCD [198], lattice QCD [199] and quasi-particle model (QPM) [200].

to 30% in a narrow band. This band corresponds to temperature regions where ζ/s is high as shown in fig. 8.1.

We also evaluate spatial diffusion coefficient which is defined as

$$D_s = \frac{T}{m_c A(p \rightarrow 0, T)}. \quad (10.30)$$

Fig. 10.5 shows our estimation of D_s for different strengths of bulk pressure along with the calculations from leading order (LO) pQCD, lattice QCD and quasi-particle model (QPM). Our results are in agreement with LO pQCD. Here we have only included $2 \rightarrow 2$ scatterings perturbatively. In the low p_T region, non-perturbative effects become dominant. These are captured by lattice QCD. Hence, our results in $p \rightarrow 0$ limit differ.

Finally, collisional energy loss in Brownian motion can be expressed in terms of drag coefficient as

$$\frac{dE}{dL} = -A(p^2, T)p. \quad (10.31)$$

Here dL is the incremental path length travelled by charm at each time step. We can propagate charm with different momentum and look at their trajectory in the (τ, x) plane. We can also estimate their energy loss and the viscous contribution to it.

We start with a charm quark at origin. We initialize it with momentum in the x -direction with values $\pm 2, \pm 5$ and ± 10 GeV. We allow it to move in the x -direction with its velocity which is calculated at each time step from its momentum. At each time-step the

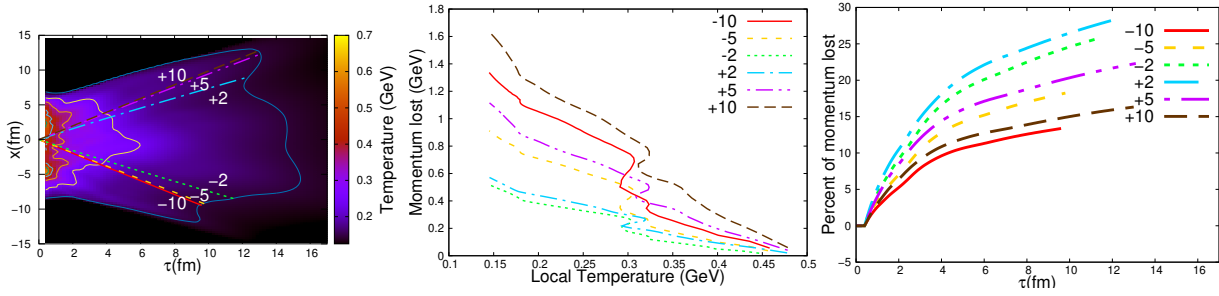


Figure 10.6: Trajectory of charm quarks with different initial momentum (left). Momentum lost by charm as a function of temperature along the trajectory (middle). Percentage momentum lost as a function of proper time (right). Numbers denote the initial momentum in the x -direction. Momentum in y and longitudinal directions is zero.

charm loses some energy based on eq. (10.31). A is calculated at each time step locally. Charm is propagated until it leaves the medium.

In fig. 10.6, we see that energy loss depends on the specific trajectory encountered by a charm. Charm loses energy more steeply at initial times when temperatures are higher and flattens as the system cools down. Charm quark with higher energy lose more momentum but it is a smaller percentage of their initial value.

Fig. 10.7 shows the momentum loss for the charm with initial momentum +5 GeV. Here we also show the momentum loss if we removed viscous corrections from the drag coefficient. Black and red lines overlap there indicating that the difference in final energy loss due to shear correction is negligible. Bottom panel shows the actual difference. With the inclusion of bulk correction (which is always negative for A , hence less energy loss) net momentum loss is reduced by about 2%

10.5 SUMMARY

In this chapter we calculated the shear and bulk corrections to collisional energy loss by charm quarks in QGP. We see that charm's transport properties could change by up to 30% in some restricted regions of QGP, but without much effect on net energy loss. However, all known transport properties should be included for theoretical consistency.

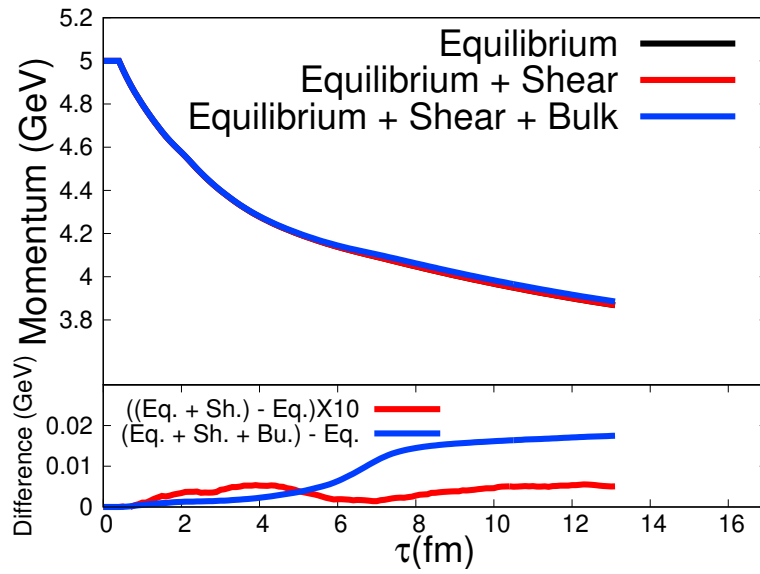


Figure 10.7: Momentum loss in a quark starting

This calculation could be used to evaluate collision rates for use in event-by-event simulations (like ones described for hard light quarks in section 2.2). Our next step would be to evaluate these rates along with radiation energy loss rates and calculate observables in an event by event simulation.

We would also like to use the energy feedback to hydro developed in chapter 9 along with our energy loss model to evaluate heavy-flavor observables.

Part IV

CONCLUSION

In this thesis, different aspects of soft and hard observables in heavy ion collisions were studied. We developed a novel mechanism to realistically simulate soft thermal fluctuations in QGP. We also studied the dynamics of Mach cones created by jets in QGP and introduced a new concurrent framework to simultaneously evolve the QGP and the jets. Further, we evaluated the out-of-equilibrium corrections to the heavy quark transport coefficients in QGP.

In chapter 6, we expanded the perturbative fluctuation technique. We evaluated experimental observables in simple settings to ascertain whether a more realistic study of thermal fluctuations is warranted. We observed that the thermal fluctuations significantly affected experimental observables; most notable the event plane correlators. We also found that the thermal fluctuations have the counter-intuitive effect of reducing photon v_2 , which could be understood in terms of decorrelation between photon and hadron planes.

A new mechanism to study thermal fluctuations in HIC was developed in chapter 7. We achieved this by using a low pass filter to remove high wavenumber noise modes from our simulations. High wavenumber noise modes decay very fast to their equilibrium values and operate on very small length scales. We examined the effect of low pass filter on noise modes in static and Bjorken flow and compared them to the known analytic results. We observed that in these simple flows, removal of high wavenumber modes does not affect the low wavenumber modes, as long as there is a separation in scale of high and low wavenumbers. We evaluated the experimental observables with shear thermal fluctuations and identified ones which are sensitive to them. As experimental observables are designed to be dependent on the long wavelength hydro modes, we did not expect them to be sensitive to removal of high wavenumber modes. We explicitly tested that by using different cutoff scales. Our results were cutoff independent up to statistical uncertainties.

In chapter 8, we extended our model to include bulk fluctuations and did an exploratory study with them. As opposed to shear fluctuations, bulk fluctuations explicitly lower the entropy production in the system and hence reduce final multiplicity. This happens as increased positive bulk viscous pressure rapidly cools the system while increased negative bulk fluctuations cannot heat it. This imbalance causes the system to

expand faster. We observed that apart from reducing multiplicity, it also enhances mean p_T . This calls for a more elaborate study of bulk fluctuations including recalibration of QGP transport coefficients.

We also commented on the situation when the magnitude of bulk viscous pressure becomes larger the thermodynamic pressure causing the net kinetic pressure to turn negative. We argued that negative kinematic pressure, though theoretically problematic, does not immediately imply hadron gas production or fireball fragmentation. We also demonstrated that the negative kinematic pressure region of the phase space does not really affect the experimental observables for Pb-Pb collisions.

In chapter 9 we studied jet medium interaction in QGP. Specifically, we added lost energy from jets as source terms in hydro equations for QGP evolution. We investigated the formation of Mach cones in QGP. We found that these source terms definitely cause an enhancement in multiplicity in the jet cone. We also found that while QGP viscosity will affect the jet shape function, it will be very difficult to extract it using this effect. We introduced a new framework to simultaneously evolve the jet and the medium. We have set model parameters from the soft sector data and our framework is now ready to explore intermediate and high p_T physics. We observed that QGP viscosity needs to be modified when one introduces minijets in simulations.

Finally, in chapter 10, we evaluated the viscous corrections to charm quark drag and diffusion coefficients in QGP. We observed that the transport coefficients of charm quark could change up to 30% in certain regions of QGP. However, net effect of viscous corrections on charm energy loss is negligible. The corrections calculated here could also be used in an event by event simulation to evaluate heavy quark observables.

We have investigated various aspects and consequences of QGP viscosity. It shows up everywhere ranging from the soft thermal fluctuations to the hard interactions. A proper extraction of QGP transport coefficients needs to take all these effects into account. While a complete self consistent model incorporating all these effects together is yet to be devised, we believe that this work is a step in that direction.

In future, a robust examination of bulk viscous fluctuations using different bulk viscosity profiles needs to be done. Our concurrent jet medium framework is ready to be utilised to explore intermediate and high p_T physics. Both the thermal fluctuations and

the medium response to jets will affect photon production, which can be evaluated. And we can do event by event simulations of HQ interactions in QGP including the viscous corrections evaluated in this work.

We hope that all these steps will lead us in the direction of a self consistent framework which includes all these physical effects. A systematic Bayesian analysis like the ones done in [168, 169] could then be employed to extract the transport properties of QGP.

BIBLIOGRAPHY

- [1] C. Young, J.I. Kapusta, C. Gale, S. Jeon, and B. Schenke. “Thermally Fluctuating Second-Order Viscous Hydrodynamics and Heavy-Ion Collisions.” In: *Phys. Rev. C* 91.4 (2015), p. 044901. DOI: [10.1103/PhysRevC.91.044901](https://doi.org/10.1103/PhysRevC.91.044901). arXiv: [1407.1077](https://arxiv.org/abs/1407.1077) [nucl-th].
- [2] Murray Gell-Mann. “A Schematic Model of Baryons and Mesons.” In: *Phys. Lett.* 8 (1964), pp. 214–215. DOI: [10.1016/S0031-9163\(64\)92001-3](https://doi.org/10.1016/S0031-9163(64)92001-3).
- [3] G. Zweig. “An SU(3) model for strong interaction symmetry and its breaking. Version 2.” In: *DEVELOPMENTS IN THE QUARK THEORY OF HADRONS. VOL. 1. 1964 - 1978*. Ed. by D.B. Lichtenberg and Simon Peter Rosen. Feb. 1964, pp. 22–101.
- [4] O.W. Greenberg. “Spin and Unitary Spin Independence in a Paraquark Model of Baryons and Mesons.” In: *Phys. Rev. Lett.* 13 (1964), pp. 598–602. DOI: [10.1103/PhysRevLett.13.598](https://doi.org/10.1103/PhysRevLett.13.598).
- [5] M.Y. Han and Yoichiro Nambu. “Three Triplet Model with Double SU(3) Symmetry.” In: *Phys. Rev.* 139 (1965). Ed. by T. Eguchi, B1006–B1010. DOI: [10.1103/PhysRev.139.B1006](https://doi.org/10.1103/PhysRev.139.B1006).
- [6] Martin Breidenbach, Jerome I. Friedman, Henry W. Kendall, Elliott D. Bloom, D.H. Coward, H.C. DeStaebler, J. Drees, Luke W. Mo, and Richard E. Taylor. “Observed behavior of highly inelastic electron-proton scattering.” In: *Phys. Rev. Lett.* 23 (1969), pp. 935–939. DOI: [10.1103/PhysRevLett.23.935](https://doi.org/10.1103/PhysRevLett.23.935).
- [7] David J. Gross and Frank Wilczek. “Ultraviolet Behavior of Nonabelian Gauge Theories.” In: *Phys. Rev. Lett.* 30 (1973). Ed. by J.C. Taylor, pp. 1343–1346. DOI: [10.1103/PhysRevLett.30.1343](https://doi.org/10.1103/PhysRevLett.30.1343).

- [8] H.David Politzer. "Reliable Perturbative Results for Strong Interactions?" In: *Phys. Rev. Lett.* 30 (1973). Ed. by J.C. Taylor, pp. 1346–1349. DOI: [10.1103/PhysRevLett.30.1346](https://doi.org/10.1103/PhysRevLett.30.1346).
- [9] Chen-Ning Yang and Robert L. Mills. "Conservation of Isotopic Spin and Isotopic Gauge Invariance." In: *Phys. Rev.* 96 (1954). Ed. by Jong-Ping Hsu and D. Fine, pp. 191–195. DOI: [10.1103/PhysRev.96.191](https://doi.org/10.1103/PhysRev.96.191).
- [10] Jr. Callan Curtis G. "Broken scale invariance in scalar field theory." In: *Phys. Rev. D* 2 (1970), pp. 1541–1547. DOI: [10.1103/PhysRevD.2.1541](https://doi.org/10.1103/PhysRevD.2.1541).
- [11] K. Symanzik. "Small distance behavior in field theory and power counting." In: *Commun. Math. Phys.* 18 (1970), pp. 227–246. DOI: [10.1007/BF01649434](https://doi.org/10.1007/BF01649434).
- [12] Michael E. Peskin and Daniel V. Schroeder. *An Introduction to quantum field theory*. Reading, USA: Addison-Wesley, 1995. ISBN: 978-0-201-50397-5.
- [13] P.A. Zyla et al. "Review of Particle Physics." In: *PTEP* 2020.8 (2020), p. 083C01. DOI: [10.1093/ptep/ptaa104](https://doi.org/10.1093/ptep/ptaa104).
- [14] Mattia Dalla Brida, Patrick Fritzsche, Tomasz Korzec, Alberto Ramos, Stefan Sint, and Rainer Sommer. "Determination of the QCD Λ -parameter and the accuracy of perturbation theory at high energies." In: *Phys. Rev. Lett.* 117.18 (2016), p. 182001. DOI: [10.1103/PhysRevLett.117.182001](https://doi.org/10.1103/PhysRevLett.117.182001). arXiv: [1604.06193](https://arxiv.org/abs/1604.06193) [hep-ph].
- [15] A. Bazavov et al. "Equation of state in (2+1)-flavor QCD." In: *Phys. Rev. D* 90 (2014), p. 094503. DOI: [10.1103/PhysRevD.90.094503](https://doi.org/10.1103/PhysRevD.90.094503). arXiv: [1407.6387](https://arxiv.org/abs/1407.6387) [hep-lat].
- [16] R.P. Feynman. "Space - time approach to quantum electrodynamics." In: *Phys. Rev.* 76 (1949). Ed. by L.M. Brown, pp. 769–789. DOI: [10.1103/PhysRev.76.769](https://doi.org/10.1103/PhysRev.76.769).
- [17] Kenneth G. Wilson. "Confinement of Quarks." In: (Feb. 1974). Ed. by J.C. Taylor, pp. 45–59. DOI: [10.1103/PhysRevD.10.2445](https://doi.org/10.1103/PhysRevD.10.2445).
- [18] R.P. Feynman. "Space-time approach to nonrelativistic quantum mechanics." In: *Rev. Mod. Phys.* 20 (1948), pp. 367–387. DOI: [10.1103/RevModPhys.20.367](https://doi.org/10.1103/RevModPhys.20.367).

- [19] J. Cleymans, R.V. Gavai, and E. Suhonen. “Quarks and Gluons at High Temperatures and Densities.” In: *Phys. Rept.* 130 (1986), p. 217. DOI: [10.1016/0370-1573\(86\)90169-9](https://doi.org/10.1016/0370-1573(86)90169-9).
- [20] Y. Aoki, G. Endrodi, Z. Fodor, S.D. Katz, and K.K. Szabo. “The Order of the quantum chromodynamics transition predicted by the standard model of particle physics.” In: *Nature* 443 (2006), pp. 675–678. DOI: [10.1038/nature05120](https://doi.org/10.1038/nature05120). arXiv: [hep-lat/0611014](https://arxiv.org/abs/hep-lat/0611014).
- [21] Bedangadas Mohanty. “Exploring the QCD phase diagram through high energy nuclear collisions: An overview.” In: *PoS CPOD2013* (2013), p. 001. DOI: [10.22323/1.185.0001](https://doi.org/10.22323/1.185.0001). arXiv: [1308.3328 \[nucl-ex\]](https://arxiv.org/abs/1308.3328).
- [22] Patrick Steinbrecher. “The QCD crossover at zero and non-zero baryon densities from Lattice QCD.” In: *Nucl. Phys. A* 982 (2019). Ed. by Federico Antinori, Andrea Dainese, Paolo Giubellino, Vincenzo Greco, Maria Paola Lombardo, and Enrico Scomparin, pp. 847–850. DOI: [10.1016/j.nuclphysa.2018.08.025](https://doi.org/10.1016/j.nuclphysa.2018.08.025). arXiv: [1807.05607 \[hep-lat\]](https://arxiv.org/abs/1807.05607).
- [23] Mark G. Alford, Krishna Rajagopal, and Frank Wilczek. “QCD at finite baryon density: Nucleon droplets and color superconductivity.” In: *Phys. Lett. B* 422 (1998), pp. 247–256. DOI: [10.1016/S0370-2693\(98\)00051-3](https://doi.org/10.1016/S0370-2693(98)00051-3). arXiv: [hep-ph/9711395](https://arxiv.org/abs/hep-ph/9711395).
- [24] R. Rapp, Thomas Schäfer, Edward V. Shuryak, and M. Velkovsky. “Diquark Bose condensates in high density matter and instantons.” In: *Phys. Rev. Lett.* 81 (1998), pp. 53–56. DOI: [10.1103/PhysRevLett.81.53](https://doi.org/10.1103/PhysRevLett.81.53). arXiv: [hep-ph/9711396](https://arxiv.org/abs/hep-ph/9711396).
- [25] Mark G. Alford, Krishna Rajagopal, and Frank Wilczek. “Color flavor locking and chiral symmetry breaking in high density QCD.” In: *Nucl. Phys. B* 537 (1999), pp. 443–458. DOI: [10.1016/S0550-3213\(98\)00668-3](https://doi.org/10.1016/S0550-3213(98)00668-3). arXiv: [hep-ph/9804403](https://arxiv.org/abs/hep-ph/9804403).
- [26] M. Asakawa and K. Yazaki. “Chiral Restoration at Finite Density and Temperature.” In: *Nucl. Phys. A* 504 (1989), pp. 668–684. DOI: [10.1016/0375-9474\(89\)90002-X](https://doi.org/10.1016/0375-9474(89)90002-X).

- [27] Gordon Baym, Tetsuo Hatsuda, Toru Kojo, Philip D. Powell, Yifan Song, and Tatsuyuki Takatsuka. “From hadrons to quarks in neutron stars: a review.” In: *Rept. Prog. Phys.* 81.5 (2018), p. 056902. DOI: [10.1088/1361-6633/aaae14](https://doi.org/10.1088/1361-6633/aaae14). arXiv: [1707.04966](https://arxiv.org/abs/1707.04966) [astro-ph.HE].
- [28] Ulrich W. Heinz. “The Quark gluon plasma at RHIC.” In: *Nucl. Phys. A* 721 (2003). Ed. by H. Toki, K. Imai, and T. Kishimoto, pp. 30–39. DOI: [10.1016/S0375-9474\(03\)01014-5](https://doi.org/10.1016/S0375-9474(03)01014-5). arXiv: [nuc1-th/0212004](https://arxiv.org/abs/nuc1-th/0212004).
- [29] Panagiota Foka and Małgorzata Anna Janik. “An overview of experimental results from ultra-relativistic heavy-ion collisions at the CERN LHC: Bulk properties and dynamical evolution.” In: *Rev. Phys.* 1 (2016), pp. 154–171. DOI: [10.1016/j.revip.2016.11.002](https://doi.org/10.1016/j.revip.2016.11.002). arXiv: [1702.07233](https://arxiv.org/abs/1702.07233) [hep-ex].
- [30] Ulrich W. Heinz and Peter F. Kolb. “Early thermalization at RHIC.” In: *Nucl. Phys. A* 702 (2002). Ed. by F. Karsch and H. Satz, pp. 269–280. DOI: [10.1016/S0375-9474\(02\)00714-5](https://doi.org/10.1016/S0375-9474(02)00714-5). arXiv: [hep-ph/0111075](https://arxiv.org/abs/hep-ph/0111075).
- [31] Matthew Luzum and Paul Romatschke. “Conformal Relativistic Viscous Hydrodynamics: Applications to RHIC results at $s(\text{NN})^{1/2} = 200\text{-GeV}$.” In: *Phys. Rev. C* 78 (2008). [Erratum: *Phys.Rev.C* 79, 039903 (2009)], p. 034915. DOI: [10.1103/PhysRevC.78.034915](https://doi.org/10.1103/PhysRevC.78.034915). arXiv: [0804.4015](https://arxiv.org/abs/0804.4015) [nucl-th].
- [32] Bjoern Schenke, Sangyong Jeon, and Charles Gale. “(3+1)D hydrodynamic simulation of relativistic heavy-ion collisions.” In: *Phys. Rev. C* 82 (2010), p. 014903. DOI: [10.1103/PhysRevC.82.014903](https://doi.org/10.1103/PhysRevC.82.014903). arXiv: [1004.1408](https://arxiv.org/abs/1004.1408) [hep-ph].
- [33] H. Niemi, K.J. Eskola, and R. Paatelainen. “Event-by-event fluctuations in a perturbative QCD + saturation + hydrodynamics model: Determining QCD matter shear viscosity in ultrarelativistic heavy-ion collisions.” In: *Phys. Rev. C* 93.2 (2016), p. 024907. DOI: [10.1103/PhysRevC.93.024907](https://doi.org/10.1103/PhysRevC.93.024907). arXiv: [1505.02677](https://arxiv.org/abs/1505.02677) [hep-ph].
- [34] Paul Romatschke. “Relativistic Fluid Dynamics Far From Local Equilibrium.” In: *Phys. Rev. Lett.* 120.1 (2018), p. 012301. DOI: [10.1103/PhysRevLett.120.012301](https://doi.org/10.1103/PhysRevLett.120.012301). arXiv: [1704.08699](https://arxiv.org/abs/1704.08699) [hep-th].

- [35] Michal P. Heller and Michal Spalinski. “Hydrodynamics Beyond the Gradient Expansion: Resurgence and Resummation.” In: *Phys. Rev. Lett.* 115.7 (2015), p. 072501. DOI: [10.1103/PhysRevLett.115.072501](https://doi.org/10.1103/PhysRevLett.115.072501). arXiv: [1503.07514 \[hep-th\]](https://arxiv.org/abs/1503.07514).
- [36] Paul Romatschke. “Relativistic Hydrodynamic Attractors with Broken Symmetries: Non-Conformal and Non-Homogeneous.” In: *JHEP* 12 (2017), p. 079. DOI: [10.1007/JHEP12\(2017\)079](https://doi.org/10.1007/JHEP12(2017)079). arXiv: [1710.03234 \[hep-th\]](https://arxiv.org/abs/1710.03234).
- [37] A. Bialas, M. Bleszynski, and W. Czyz. “Multiplicity Distributions in Nucleus-Nucleus Collisions at High-Energies.” In: *Nucl. Phys. B* 111 (1976), pp. 461–476. DOI: [10.1016/0550-3213\(76\)90329-1](https://doi.org/10.1016/0550-3213(76)90329-1).
- [38] Roy J. Glauber. “Quantum Optics and Heavy Ion Physics.” In: *Nucl. Phys. A* 774 (2006). Ed. by T. Csorgo, P. Levai, G. David, and G. Papp, pp. 3–13. DOI: [10.1016/j.nuclphysa.2006.06.009](https://doi.org/10.1016/j.nuclphysa.2006.06.009). arXiv: [nucl-th/0604021](https://arxiv.org/abs/nucl-th/0604021).
- [39] Roger D. Woods and David S. Saxon. “Diffuse Surface Optical Model for Nucleon-Nuclei Scattering.” In: *Phys. Rev.* 95 (1954), pp. 577–578. DOI: [10.1103/PhysRev.95.577](https://doi.org/10.1103/PhysRev.95.577).
- [40] Bjoern Schenke, Prithwish Tribedy, and Raju Venugopalan. “Fluctuating Glasma initial conditions and flow in heavy ion collisions.” In: *Phys. Rev. Lett.* 108 (2012), p. 252301. DOI: [10.1103/PhysRevLett.108.252301](https://doi.org/10.1103/PhysRevLett.108.252301). arXiv: [1202.6646 \[nucl-th\]](https://arxiv.org/abs/1202.6646).
- [41] Scott McDonald, Chun Shen, Francois Fillion-Gourdeau, Sangyong Jeon, and Charles Gale. “Hydrodynamic predictions for Pb+Pb collisions at 5.02 TeV.” In: *Phys. Rev. C* 95.6 (2017), p. 064913. DOI: [10.1103/PhysRevC.95.064913](https://doi.org/10.1103/PhysRevC.95.064913). arXiv: [1609.02958 \[hep-ph\]](https://arxiv.org/abs/1609.02958).
- [42] Larry D. McLerran and Raju Venugopalan. “Computing quark and gluon distribution functions for very large nuclei.” In: *Phys. Rev. D* 49 (1994), pp. 2233–2241. DOI: [10.1103/PhysRevD.49.2233](https://doi.org/10.1103/PhysRevD.49.2233). arXiv: [hep-ph/9309289](https://arxiv.org/abs/hep-ph/9309289).
- [43] Ernst Sichtermann. “Gluon Saturation and EIC.” In: *Nucl. Phys. A* 956 (2016). Ed. by Y. Akiba, S. Esumi, K. Fukushima, H. Hamagaki, T. Hatsuda, T. Hirano, and K. Shigaki, pp. 233–239. DOI: [10.1016/j.nuclphysa.2016.03.009](https://doi.org/10.1016/j.nuclphysa.2016.03.009).

- [44] Henri Kowalski and Derek Teaney. “An Impact parameter dipole saturation model.” In: *Phys. Rev. D* 68 (2003), p. 114005. DOI: [10.1103/PhysRevD.68.114005](https://doi.org/10.1103/PhysRevD.68.114005). arXiv: [hep-ph/0304189](https://arxiv.org/abs/hep-ph/0304189).
- [45] Aleksi Kurkela, Aleksas Mazeliauskas, Jean-François Paquet, Sören Schlichting, and Derek Teaney. “Matching the Nonequilibrium Initial Stage of Heavy Ion Collisions to Hydrodynamics with QCD Kinetic Theory.” In: *Phys. Rev. Lett.* 122.12 (2019), p. 122302. DOI: [10.1103/PhysRevLett.122.122302](https://doi.org/10.1103/PhysRevLett.122.122302). arXiv: [1805.01604](https://arxiv.org/abs/1805.01604) [hep-ph].
- [46] Dmitri Kharzeev and Marzia Nardi. “Hadron production in nuclear collisions at RHIC and high density QCD.” In: *Phys. Lett. B* 507 (2001), pp. 121–128. DOI: [10.1016/S0370-2693\(01\)00457-9](https://doi.org/10.1016/S0370-2693(01)00457-9). arXiv: [nucl-th/0012025](https://arxiv.org/abs/nucl-th/0012025).
- [47] Zi-Wei Lin, Che Ming Ko, Bao-An Li, Bin Zhang, and Subrata Pal. “A Multi-phase transport model for relativistic heavy ion collisions.” In: *Phys. Rev. C* 72 (2005), p. 064901. DOI: [10.1103/PhysRevC.72.064901](https://doi.org/10.1103/PhysRevC.72.064901). arXiv: [nucl-th/0411110](https://arxiv.org/abs/nucl-th/0411110).
- [48] Szabolcs Borsanyi, Zoltan Fodor, Christian Hoelbling, Sandor D. Katz, Stefan Krieg, and Kalman K. Szabo. “Full result for the QCD equation of state with 2+1 flavors.” In: *Phys. Lett. B* 730 (2014), pp. 99–104. DOI: [10.1016/j.physletb.2014.01.007](https://doi.org/10.1016/j.physletb.2014.01.007). arXiv: [1309.5258](https://arxiv.org/abs/1309.5258) [hep-lat].
- [49] Luciano Rezzolla and Olindo Zanotti. *Relativistic hydrodynamics*. Oxford University Press, 2013.
- [50] L.D. Landau and E.M. Lifshitz. “Chapter XV - Relativistic Fluid Dynamics.” In: *Fluid Mechanics*. Pergamon, 1959, pp. 499–506. ISBN: 978-0-08-029142-0. DOI: <https://doi.org/10.1016/B978-0-08-029142-0.50020-9>.
- [51] William A. Hiscock and Lee Lindblom. “Generic instabilities in first-order dissipative relativistic fluid theories.” In: *Phys. Rev. D* 31 (1985), pp. 725–733. DOI: [10.1103/PhysRevD.31.725](https://doi.org/10.1103/PhysRevD.31.725).
- [52] Pavel Kovtun. “First-order relativistic hydrodynamics is stable.” In: *JHEP* 10 (2019), p. 034. DOI: [10.1007/JHEP10\(2019\)034](https://doi.org/10.1007/JHEP10(2019)034). arXiv: [1907.08191](https://arxiv.org/abs/1907.08191) [hep-th].

- [53] Raphael E. Hoult and Pavel Kovtun. “Stable and causal relativistic Navier-Stokes equations.” In: *JHEP* 06 (2020), p. 067. DOI: [10.1007/JHEP06\(2020\)067](https://doi.org/10.1007/JHEP06(2020)067). arXiv: [2004.04102](https://arxiv.org/abs/2004.04102) [hep-th].
- [54] Arpan Das, Wojciech Florkowski, and Radoslaw Ryblewski. “Correspondence between Israel-Stewart and first-order casual and stable hydrodynamics for the boost-invariant massive case with zero baryon density.” In: *Phys. Rev. D* 102.3 (2020), p. 031501. DOI: [10.1103/PhysRevD.102.031501](https://doi.org/10.1103/PhysRevD.102.031501). arXiv: [2006.00536](https://arxiv.org/abs/2006.00536) [nucl-th].
- [55] Arpan Das, Wojciech Florkowski, and Radoslaw Ryblewski. “Correspondence between Israel-Stewart and first-order causal and stable hydrodynamics for Bjorken-expanding baryon-rich systems with vanishing particle masses.” In: (Oct. 2020). arXiv: [2010.02596](https://arxiv.org/abs/2010.02596) [nucl-th].
- [56] Ingo Muller. “Zum Paradoxon der Wärmeleitungstheorie.” In: *Z. Phys.* 198 (1967), pp. 329–344. DOI: [10.1007/BF01326412](https://doi.org/10.1007/BF01326412).
- [57] W. Israel and J.M. Stewart. “Transient relativistic thermodynamics and kinetic theory.” In: *Annals Phys.* 118 (1979), pp. 341–372. DOI: [10.1016/0003-4916\(79\)90130-1](https://doi.org/10.1016/0003-4916(79)90130-1).
- [58] G.S. Denicol, H. Niemi, E. Molnar, and D.H. Rischke. “Derivation of transient relativistic fluid dynamics from the Boltzmann equation.” In: *Phys. Rev. D* 85 (2012). [Erratum: *Phys.Rev.D* 91, 039902 (2015)], p. 114047. DOI: [10.1103/PhysRevD.85.114047](https://doi.org/10.1103/PhysRevD.85.114047). arXiv: [1202.4551](https://arxiv.org/abs/1202.4551) [nucl-th].
- [59] E. Molnár, H. Niemi, G.S. Denicol, and D.H. Rischke. “Relative importance of second-order terms in relativistic dissipative fluid dynamics.” In: *Phys. Rev. D* 89.7 (2014), p. 074010. DOI: [10.1103/PhysRevD.89.074010](https://doi.org/10.1103/PhysRevD.89.074010). arXiv: [1308.0785](https://arxiv.org/abs/1308.0785) [nucl-th].
- [60] G.S. Denicol, S. Jeon, and C. Gale. “Transport Coefficients of Bulk Viscous Pressure in the 14-moment approximation.” In: *Phys. Rev. C* 90.2 (2014), p. 024912. DOI: [10.1103/PhysRevC.90.024912](https://doi.org/10.1103/PhysRevC.90.024912). arXiv: [1403.0962](https://arxiv.org/abs/1403.0962) [nucl-th].
- [61] Paul Romatschke and Ulrike Romatschke. *Relativistic Fluid Dynamics In and Out of Equilibrium*. Cambridge Monographs on Mathematical Physics. Cambridge Uni-

- versity Press, May 2019. ISBN: 978-1-108-48368-1, 978-1-108-75002-8. DOI: [10.1017/9781108651998](https://doi.org/10.1017/9781108651998). arXiv: [1712.05815 \[nucl-th\]](https://arxiv.org/abs/1712.05815).
- [62] J.D. Bjorken. “Highly Relativistic Nucleus-Nucleus Collisions: The Central Rapidity Region.” In: *Phys. Rev. D* 27 (1983), pp. 140–151. DOI: [10.1103/PhysRevD.27.140](https://doi.org/10.1103/PhysRevD.27.140).
- [63] Alexander Kurganov and Eitan Tadmor. “New High-Resolution Central Schemes for Nonlinear Conservation Laws and Convection–Diffusion Equations.” In: *Journal of Computational Physics* 160.1 (2000), pp. 241–282. ISSN: 0021-9991. DOI: <https://doi.org/10.1006/jcph.2000.6459>.
- [64] Clint Young. “Numerical integration of thermal noise in relativistic hydrodynamics.” In: *Phys. Rev. C* 89.2 (2014), p. 024913. DOI: [10.1103/PhysRevC.89.024913](https://doi.org/10.1103/PhysRevC.89.024913). arXiv: [1306.0472 \[nucl-th\]](https://arxiv.org/abs/1306.0472).
- [65] S. Ryu, J. F. Paquet, C. Shen, G.S. Denicol, B. Schenke, S. Jeon, and C. Gale. “Importance of the Bulk Viscosity of QCD in Ultrarelativistic Heavy-Ion Collisions.” In: *Phys. Rev. Lett.* 115.13 (2015), p. 132301. DOI: [10.1103/PhysRevLett.115.132301](https://doi.org/10.1103/PhysRevLett.115.132301). arXiv: [1502.01675 \[nucl-th\]](https://arxiv.org/abs/1502.01675).
- [66] Fred Cooper and Graham Frye. “Comment on the Single Particle Distribution in the Hydrodynamic and Statistical Thermodynamic Models of Multiparticle Production.” In: *Phys. Rev. D* 10 (1974), p. 186. DOI: [10.1103/PhysRevD.10.186](https://doi.org/10.1103/PhysRevD.10.186).
- [67] S. Chapman, T.G. Cowling, D. Burnett, and C. Cercignani. *The Mathematical Theory of Non-uniform Gases: An Account of the Kinetic Theory of Viscosity, Thermal Conduction and Diffusion in Gases*. Cambridge Mathematical Library. Cambridge University Press, 1990. ISBN: 9780521408448.
- [68] Harold Grad. “On the kinetic theory of rarefied gases.” In: *Communications on Pure and Applied Mathematics* 2.4 (1949), pp. 331–407. DOI: <https://doi.org/10.1002/cpa.3160020403>. eprint: <https://onlinelibrary.wiley.com/doi/pdf/10.1002/cpa.3160020403>.
- [69] Derek Teaney. “The Effects of viscosity on spectra, elliptic flow, and HBT radii.” In: *Phys. Rev. C* 68 (2003), p. 034913. DOI: [10.1103/PhysRevC.68.034913](https://doi.org/10.1103/PhysRevC.68.034913). arXiv: [nuc1-th/0301099](https://arxiv.org/abs/nuc1-th/0301099).

- [70] Piotr Bozek. “Bulk and shear viscosities of matter created in relativistic heavy-ion collisions.” In: *Phys. Rev. C* 81 (2010), p. 034909. DOI: [10.1103/PhysRevC.81.034909](https://doi.org/10.1103/PhysRevC.81.034909). arXiv: [0911.2397](https://arxiv.org/abs/0911.2397) [nucl-th].
- [71] Jean-François Paquet, Chun Shen, Gabriel S. Denicol, Matthew Luzum, Björn Schenke, Sangyong Jeon, and Charles Gale. “Production of photons in relativistic heavy-ion collisions.” In: *Phys. Rev. C* 93.4 (2016), p. 044906. DOI: [10.1103/PhysRevC.93.044906](https://doi.org/10.1103/PhysRevC.93.044906). arXiv: [1509.06738](https://arxiv.org/abs/1509.06738) [hep-ph].
- [72] Chun Shen. *iSpectraSampler (iSS)*. <https://github.com/chunshen1987/iSS>.
- [73] Jan Steinheimer and Volker Koch. “Effect of finite particle number sampling on baryon number fluctuations.” In: *Phys. Rev. C* 96.3 (2017), p. 034907. DOI: [10.1103/PhysRevC.96.034907](https://doi.org/10.1103/PhysRevC.96.034907). arXiv: [1705.08538](https://arxiv.org/abs/1705.08538) [nucl-th].
- [74] S.A. Bass et al. “Microscopic models for ultrarelativistic heavy ion collisions.” In: *Prog. Part. Nucl. Phys.* 41 (1998), pp. 255–369. DOI: [10.1016/S0146-6410\(98\)00058-1](https://doi.org/10.1016/S0146-6410(98)00058-1). arXiv: [nuc1-th/9803035](https://arxiv.org/abs/nuc1-th/9803035).
- [75] M. Bleicher et al. “Relativistic hadron hadron collisions in the ultrarelativistic quantum molecular dynamics model.” In: *J. Phys. G* 25 (1999), pp. 1859–1896. DOI: [10.1088/0954-3899/25/9/308](https://doi.org/10.1088/0954-3899/25/9/308). arXiv: [hep-ph/9909407](https://arxiv.org/abs/hep-ph/9909407).
- [76] Jorge Casalderrey-Solana, Doga Can Gulhan, José Guilherme Milhano, Daniel Pablos, and Krishna Rajagopal. “A Hybrid Strong/Weak Coupling Approach to Jet Quenching.” In: *JHEP* 10 (2014). [Erratum: *JHEP* 09, 175 (2015)], p. 019. DOI: [10.1007/JHEP09\(2015\)175](https://doi.org/10.1007/JHEP09(2015)175). arXiv: [1405.3864](https://arxiv.org/abs/1405.3864) [hep-ph].
- [77] Torbjorn Sjostrand, Stephen Mrenna, and Peter Z. Skands. “A Brief Introduction to PYTHIA 8.1.” In: *Comput. Phys. Commun.* 178 (2008), pp. 852–867. DOI: [10.1016/j.cpc.2008.01.036](https://doi.org/10.1016/j.cpc.2008.01.036). arXiv: [0710.3820](https://arxiv.org/abs/0710.3820) [hep-ph].
- [78] V.N. Gribov and L.N. Lipatov. “Deep inelastic e p scattering in perturbation theory.” In: *Sov. J. Nucl. Phys.* 15 (1972), pp. 438–450.
- [79] Guido Altarelli and G. Parisi. “Asymptotic Freedom in Parton Language.” In: *Nucl. Phys. B* 126 (1977), pp. 298–318. DOI: [10.1016/0550-3213\(77\)90384-4](https://doi.org/10.1016/0550-3213(77)90384-4).

- [80] Yuri L. Dokshitzer. “Calculation of the Structure Functions for Deep Inelastic Scattering and $e^+ e^-$ Annihilation by Perturbation Theory in Quantum Chromodynamics.” In: *Sov. Phys. JETP* 46 (1977), pp. 641–653.
- [81] Paul M. Chesler and Krishna Rajagopal. “Jet quenching in strongly coupled plasma.” In: *Phys. Rev. D* 90.2 (2014), p. 025033. DOI: [10.1103/PhysRevD.90.025033](https://doi.org/10.1103/PhysRevD.90.025033). arXiv: [1402.6756](https://arxiv.org/abs/1402.6756) [hep-th].
- [82] Paul M. Chesler and Krishna Rajagopal. “On the Evolution of Jet Energy and Opening Angle in Strongly Coupled Plasma.” In: *JHEP* 05 (2016), p. 098. DOI: [10.1007/JHEP05\(2016\)098](https://doi.org/10.1007/JHEP05(2016)098). arXiv: [1511.07567](https://arxiv.org/abs/1511.07567) [hep-th].
- [83] Bo Andersson, G. Gustafson, G. Ingelman, and T. Sjostrand. “Parton Fragmentation and String Dynamics.” In: *Phys. Rept.* 97 (1983), pp. 31–145. DOI: [10.1016/0370-1573\(83\)90080-7](https://doi.org/10.1016/0370-1573(83)90080-7).
- [84] Silvia Ferreres-Solé and Torbjörn Sjöstrand. “The space–time structure of hadronization in the Lund model.” In: *Eur. Phys. J. C* 78.11 (2018), p. 983. DOI: [10.1140/epjc/s10052-018-6459-8](https://doi.org/10.1140/epjc/s10052-018-6459-8). arXiv: [1808.04619](https://arxiv.org/abs/1808.04619) [hep-ph].
- [85] Bjoern Schenke, Charles Gale, and Sangyong Jeon. “MARTINI: An Event generator for relativistic heavy-ion collisions.” In: *Phys. Rev. C* 80 (2009), p. 054913. DOI: [10.1103/PhysRevC.80.054913](https://doi.org/10.1103/PhysRevC.80.054913). arXiv: [0909.2037](https://arxiv.org/abs/0909.2037) [hep-ph].
- [86] Hanlin Li, Fuming Liu, Guo-liang Ma, Xin-Nian Wang, and Yan Zhu. “Mach cone induced by γ -triggered jets in high-energy heavy-ion collisions.” In: *Phys. Rev. Lett.* 106 (2011), p. 012301. DOI: [10.1103/PhysRevLett.106.012301](https://doi.org/10.1103/PhysRevLett.106.012301). arXiv: [1006.2893](https://arxiv.org/abs/1006.2893) [nucl-th].
- [87] B. Svetitsky. “Diffusion of charmed quarks in the quark-gluon plasma.” In: *Phys. Rev. D* 37 (1988), pp. 2484–2491. DOI: [10.1103/PhysRevD.37.2484](https://doi.org/10.1103/PhysRevD.37.2484).
- [88] Munshi G. Mustafa. “Energy loss of charm quarks in the quark-gluon plasma: Collisional versus radiative.” In: *Phys. Rev. C* 72 (2005), p. 014905. DOI: [10.1103/PhysRevC.72.014905](https://doi.org/10.1103/PhysRevC.72.014905). arXiv: [hep-ph/0412402](https://arxiv.org/abs/hep-ph/0412402).

- [89] Chun Shen, Ulrich W. Heinz, Jean-Francois Paquet, Igor Kozlov, and Charles Gale. “Anisotropic flow of thermal photons as a quark-gluon plasma viscometer.” In: *Phys. Rev. C* 91.2 (2015), p. 024908. DOI: [10.1103/PhysRevC.91.024908](https://doi.org/10.1103/PhysRevC.91.024908). arXiv: [1308.2111](https://arxiv.org/abs/1308.2111) [nucl-th].
- [90] Kevin Dusling. “Photons as a viscometer of heavy ion collisions.” In: *Nucl. Phys. A* 839 (2010), pp. 70–77. DOI: [10.1016/j.nuclphysa.2010.04.001](https://doi.org/10.1016/j.nuclphysa.2010.04.001). arXiv: [0903.1764](https://arxiv.org/abs/0903.1764) [nucl-th].
- [91] Kenneth Aamodt et al. “Centrality dependence of the charged-particle multiplicity density at mid-rapidity in Pb-Pb collisions at $\sqrt{s_{NN}} = 2.76$ TeV.” In: *Phys. Rev. Lett.* 106 (2011), p. 032301. DOI: [10.1103/PhysRevLett.106.032301](https://doi.org/10.1103/PhysRevLett.106.032301). arXiv: [1012.1657](https://arxiv.org/abs/1012.1657) [nucl-ex].
- [92] Ehab Abbas et al. “Centrality dependence of the pseudorapidity density distribution for charged particles in Pb-Pb collisions at $\sqrt{s_{NN}} = 2.76$ TeV.” In: *Phys. Lett. B* 726 (2013), pp. 610–622. DOI: [10.1016/j.physletb.2013.09.022](https://doi.org/10.1016/j.physletb.2013.09.022). arXiv: [1304.0347](https://arxiv.org/abs/1304.0347) [nucl-ex].
- [93] Betty Abelev et al. “Centrality Dependence of Charged Particle Production at Large Transverse Momentum in Pb–Pb Collisions at $\sqrt{s_{NN}} = 2.76$ TeV.” In: *Phys. Lett. B* 720 (2013), pp. 52–62. DOI: [10.1016/j.physletb.2013.01.051](https://doi.org/10.1016/j.physletb.2013.01.051). arXiv: [1208.2711](https://arxiv.org/abs/1208.2711) [hep-ex].
- [94] Kyong Chol Han, Rainer J. Fries, and Che Ming Ko. “Jet Fragmentation via Recombination of Parton Showers.” In: *Phys. Rev. C* 93.4 (2016), p. 045207. DOI: [10.1103/PhysRevC.93.045207](https://doi.org/10.1103/PhysRevC.93.045207). arXiv: [1601.00708](https://arxiv.org/abs/1601.00708) [nucl-th].
- [95] Arthur M. Poskanzer and S.A. Voloshin. “Methods for analyzing anisotropic flow in relativistic nuclear collisions.” In: *Phys. Rev. C* 58 (1998), pp. 1671–1678. DOI: [10.1103/PhysRevC.58.1671](https://doi.org/10.1103/PhysRevC.58.1671). arXiv: [nuc1-ex/9805001](https://arxiv.org/abs/nuc1-ex/9805001).
- [96] Jean-Yves Ollitrault. “Anisotropy as a signature of transverse collective flow.” In: *Phys. Rev. D* 46 (1992), pp. 229–245. DOI: [10.1103/PhysRevD.46.229](https://doi.org/10.1103/PhysRevD.46.229).
- [97] Zi-wei Lin and C. M. Ko. “Partonic effects on the elliptic flow at RHIC.” In: *Phys. Rev. C* 65 (2002), p. 034904. DOI: [10.1103/PhysRevC.65.034904](https://doi.org/10.1103/PhysRevC.65.034904). arXiv: [nuc1-th/0108039](https://arxiv.org/abs/nuc1-th/0108039).

- [98] Scott McDonald. private communication. 2020.
- [99] C. Adler et al. “Elliptic flow from two and four particle correlations in Au+Au collisions at $\sqrt{s_{NN}} = 130$ -GeV.” In: *Phys. Rev. C* 66 (2002), p. 034904. DOI: [10.1103/PhysRevC.66.034904](https://doi.org/10.1103/PhysRevC.66.034904). arXiv: [nucl-ex/0206001](https://arxiv.org/abs/nuclex/0206001).
- [100] S. Wang, Y.Z. Jiang, Y.M. Liu, D. Keane, D. Beavis, S.Y. Chu, S.Y. Fung, M. Vient, C. Hartnack, and Horst Stoecker. “Measurement of collective flow in heavy ion collisions using particle pair correlations.” In: *Phys. Rev. C* 44 (1991), pp. 1091–1095. DOI: [10.1103/PhysRevC.44.1091](https://doi.org/10.1103/PhysRevC.44.1091).
- [101] Nicolas Borghini, Phuong Mai Dinh, and Jean-Yves Ollitrault. “Flow analysis from multiparticle azimuthal correlations.” In: *Phys. Rev. C* 64 (2001), p. 054901. DOI: [10.1103/PhysRevC.64.054901](https://doi.org/10.1103/PhysRevC.64.054901). arXiv: [nucl-th/0105040](https://arxiv.org/abs/nucloth/0105040).
- [102] Rajeev S. Bhalerao, Matthew Luzum, and Jean-Yves Ollitrault. “Determining initial-state fluctuations from flow measurements in heavy-ion collisions.” In: *Phys. Rev. C* 84 (2011), p. 034910. DOI: [10.1103/PhysRevC.84.034910](https://doi.org/10.1103/PhysRevC.84.034910). arXiv: [1104.4740](https://arxiv.org/abs/1104.4740) [nucl-th].
- [103] Jiangyong Jia. “Event-shape fluctuations and flow correlations in ultra-relativistic heavy-ion collisions.” In: *J. Phys. G* 41.12 (2014), p. 124003. DOI: [10.1088/0954-3899/41/12/124003](https://doi.org/10.1088/0954-3899/41/12/124003). arXiv: [1407.6057](https://arxiv.org/abs/1407.6057) [nucl-ex].
- [104] Li Yan and Jean-Yves Ollitrault. “ v_4, v_5, v_6, v_7 : nonlinear hydrodynamic response versus LHC data.” In: *Phys. Lett. B* 744 (2015), pp. 82–87. DOI: [10.1016/j.physletb.2015.03.040](https://doi.org/10.1016/j.physletb.2015.03.040). arXiv: [1502.02502](https://arxiv.org/abs/1502.02502) [nucl-th].
- [105] Xin-Nian Wang. “Effect of jet quenching on high p_T hadron spectra in high-energy nuclear collisions.” In: *Phys. Rev. C* 58 (1998), p. 2321. DOI: [10.1103/PhysRevC.58.2321](https://doi.org/10.1103/PhysRevC.58.2321). arXiv: [hep-ph/9804357](https://arxiv.org/abs/hep-ph/9804357).
- [106] A. Kumar et al. “Jet quenching in a multi-stage Monte Carlo approach.” In: *28th International Conference on Ultrarelativistic Nucleus-Nucleus Collisions*. Feb. 2020. arXiv: [2002.07124](https://arxiv.org/abs/2002.07124) [nucl-th].
- [107] Serguei Chatrchyan et al. “Modification of Jet Shapes in PbPb Collisions at $\sqrt{s_{NN}} = 2.76$ TeV.” In: *Phys. Lett. B* 730 (2014), pp. 243–263. DOI: [10.1016/j.physletb.2014.01.042](https://doi.org/10.1016/j.physletb.2014.01.042). arXiv: [1310.0878](https://arxiv.org/abs/1310.0878) [nucl-ex].

- [108] Alexander L Fetter and John Dirk Walecka. *Quantum theory of many-particle systems*. Courier Corporation, 2012.
- [109] J.I. Kapusta and Charles Gale. *Finite-temperature field theory: Principles and applications*. Cambridge Monographs on Mathematical Physics. Cambridge University Press, 2011. ISBN: 978-0-521-17322-3, 978-0-521-82082-0, 978-0-511-22280-1. DOI: [10.1017/CB09780511535130](https://doi.org/10.1017/CB09780511535130).
- [110] Herbert B. Callen and Theodore A. Welton. “Irreversibility and Generalized Noise.” In: *Phys. Rev.* 83 (1 1951), pp. 34–40. DOI: [10.1103/PhysRev.83.34](https://doi.org/10.1103/PhysRev.83.34).
- [111] Ryogo Kubo. “Statistical-Mechanical Theory of Irreversible Processes. I. General Theory and Simple Applications to Magnetic and Conduction Problems.” In: *Journal of the Physical Society of Japan* 12.6 (1957), pp. 570–586. DOI: [10.1143/JPSJ.12.570](https://doi.org/10.1143/JPSJ.12.570).
- [112] A. Einstein. “Über die von der molekularkinetischen Theorie der Wärme geforderte Bewegung von in ruhenden Flüssigkeiten suspendierten Teilchen.” In: *Annalen der Physik* 322.8 (1905), pp. 549–560. DOI: [10.1002/andp.19053220806](https://doi.org/10.1002/andp.19053220806).
- [113] H. Nyquist. “Thermal Agitation of Electric Charge in Conductors.” In: *Phys. Rev.* 32 (1 1928), pp. 110–113. DOI: [10.1103/PhysRev.32.110](https://doi.org/10.1103/PhysRev.32.110).
- [114] Marcus Bluhm et al. “Dynamics of critical fluctuations: Theory – phenomenology – heavy-ion collisions.” In: *Nucl. Phys. A* 1003 (2020), p. 122016. DOI: [10.1016/j.nuclphysa.2020.122016](https://doi.org/10.1016/j.nuclphysa.2020.122016). arXiv: [2001.08831](https://arxiv.org/abs/2001.08831) [nucl-th].
- [115] Y Pomeau and P Résibois. “Time dependent correlation functions and mode-mode coupling theories.” In: *Physics Reports* 19.2 (1975), pp. 63–139. ISSN: 0370-1573. DOI: [https://doi.org/10.1016/0370-1573\(75\)90019-8](https://doi.org/10.1016/0370-1573(75)90019-8).
- [116] Pavel Kovtun, Guy D. Moore, and Paul Romatschke. “The stickiness of sound: An absolute lower limit on viscosity and the breakdown of second order relativistic hydrodynamics.” In: *Phys. Rev. D* 84 (2011), p. 025006. DOI: [10.1103/PhysRevD.84.025006](https://doi.org/10.1103/PhysRevD.84.025006). arXiv: [1104.1586](https://arxiv.org/abs/1104.1586) [hep-ph].

- [117] Yukinao Akamatsu, Aleksas Mazeliauskas, and Derek Teaney. “A kinetic regime of hydrodynamic fluctuations and long time tails for a Bjorken expansion.” In: *Phys. Rev. C* 95.1 (2017), p. 014909. DOI: [10.1103/PhysRevC.95.014909](https://doi.org/10.1103/PhysRevC.95.014909). arXiv: [1606.07742](https://arxiv.org/abs/1606.07742) [nucl-th].
- [118] Yukinao Akamatsu, Aleksas Mazeliauskas, and Derek Teaney. “Bulk viscosity from hydrodynamic fluctuations with relativistic hydrokinetic theory.” In: *Phys. Rev. C* 97.2 (2018), p. 024902. DOI: [10.1103/PhysRevC.97.024902](https://doi.org/10.1103/PhysRevC.97.024902). arXiv: [1708.05657](https://arxiv.org/abs/1708.05657) [nucl-th].
- [119] M. Martinez and Thomas Schäfer. “Stochastic hydrodynamics and long time tails of an expanding conformal charged fluid.” In: *Phys. Rev. C* 99.5 (2019), p. 054902. DOI: [10.1103/PhysRevC.99.054902](https://doi.org/10.1103/PhysRevC.99.054902). arXiv: [1812.05279](https://arxiv.org/abs/1812.05279) [hep-th].
- [120] Xin An, Gokce Basar, Mikhail Stephanov, and Ho-Ung Yee. “Relativistic Hydrodynamic Fluctuations.” In: *Phys. Rev. C* 100.2 (2019), p. 024910. DOI: [10.1103/PhysRevC.100.024910](https://doi.org/10.1103/PhysRevC.100.024910). arXiv: [1902.09517](https://arxiv.org/abs/1902.09517) [hep-th].
- [121] Xin An, Gökçe Başar, Mikhail Stephanov, and Ho-Ung Yee. “Fluctuation dynamics in a relativistic fluid with a critical point.” In: *Phys. Rev. C* 102.3 (2020), p. 034901. DOI: [10.1103/PhysRevC.102.034901](https://doi.org/10.1103/PhysRevC.102.034901). arXiv: [1912.13456](https://arxiv.org/abs/1912.13456) [hep-th].
- [122] M. Stephanov and Y. Yin. “Hydrodynamics with parametric slowing down and fluctuations near the critical point.” In: *Phys. Rev. D* 98.3 (2018), p. 036006. DOI: [10.1103/PhysRevD.98.036006](https://doi.org/10.1103/PhysRevD.98.036006). arXiv: [1712.10305](https://arxiv.org/abs/1712.10305) [nucl-th].
- [123] Krishna Rajagopal, Gregory Ridgway, Ryan Weller, and Yi Yin. “Hydro+ in Action: Understanding the Out-of-Equilibrium Dynamics Near a Critical Point in the QCD Phase Diagram.” In: (Aug. 2019). arXiv: [1908.08539](https://arxiv.org/abs/1908.08539) [hep-ph].
- [124] Lipei Du, Ulrich Heinz, Krishna Rajagopal, and Yi Yin. “Fluctuation dynamics near the QCD critical point.” In: (Apr. 2020). arXiv: [2004.02719](https://arxiv.org/abs/2004.02719) [nucl-th].
- [125] Pavel Kovtun and Laurence G. Yaffe. “Hydrodynamic fluctuations, long time tails, and supersymmetry.” In: *Phys. Rev. D* 68 (2003), p. 025007. DOI: [10.1103/PhysRevD.68.025007](https://doi.org/10.1103/PhysRevD.68.025007). arXiv: [hep-th/0303010](https://arxiv.org/abs/hep-th/0303010).

- [126] Mauricio Martinez and Thomas Schäfer. “Hydrodynamic tails and a fluctuation bound on the bulk viscosity.” In: *Phys. Rev. A* 96.6 (2017), p. 063607. DOI: [10.1103/PhysRevA.96.063607](https://doi.org/10.1103/PhysRevA.96.063607). arXiv: [1708.01548](https://arxiv.org/abs/1708.01548) [cond-mat.quant-gas].
- [127] Jingyi Chao and Thomas Schaefer. “Multiplicative noise and the diffusion of conserved densities.” In: (Aug. 2020). arXiv: [2008.01269](https://arxiv.org/abs/2008.01269) [hep-th].
- [128] Michael Crossley, Paolo Glorioso, and Hong Liu. “Effective field theory of dissipative fluids.” In: *JHEP* 09 (2017), p. 095. DOI: [10.1007/JHEP09\(2017\)095](https://doi.org/10.1007/JHEP09(2017)095). arXiv: [1511.03646](https://arxiv.org/abs/1511.03646) [hep-th].
- [129] Paolo Glorioso, Michael Crossley, and Hong Liu. “Effective field theory of dissipative fluids (II): classical limit, dynamical KMS symmetry and entropy current.” In: *JHEP* 09 (2017), p. 096. DOI: [10.1007/JHEP09\(2017\)096](https://doi.org/10.1007/JHEP09(2017)096). arXiv: [1701.07817](https://arxiv.org/abs/1701.07817) [hep-th].
- [130] Pak Hang Chris Lau, Hong Liu, and Yi Yin. “Characterizing hydrodynamical fluctuations in heavy-ion collisions from effective field theory approach.” In: *Nucl. Phys. A* 982 (2019). Ed. by Federico Antinori, Andrea Dainese, Paolo Giubellino, Vincenzo Greco, Maria Paola Lombardo, and Enrico Scapparini, pp. 923–926. DOI: [10.1016/j.nuclphysa.2018.10.056](https://doi.org/10.1016/j.nuclphysa.2018.10.056).
- [131] Xin An, Gökçe Başar, Mikhail Stephanov, and Ho-Ung Yee. “Evolution of Non-Gaussian Hydrodynamic Fluctuations.” In: (Sept. 2020). arXiv: [2009.10742](https://arxiv.org/abs/2009.10742) [hep-th].
- [132] J.I. Kapusta, B. Muller, and M. Stephanov. “Relativistic Theory of Hydrodynamic Fluctuations with Applications to Heavy Ion Collisions.” In: *Phys. Rev. C* 85 (2012), p. 054906. DOI: [10.1103/PhysRevC.85.054906](https://doi.org/10.1103/PhysRevC.85.054906). arXiv: [1112.6405](https://arxiv.org/abs/1112.6405) [nucl-th].
- [133] Kurt Jacobs. *Stochastic Processes for Physicists: Understanding Noisy Systems*. Cambridge University Press, 2010. DOI: [10.1017/CB09780511815980](https://doi.org/10.1017/CB09780511815980).
- [134] Pavel Kovtun. “Lectures on hydrodynamic fluctuations in relativistic theories.” In: *J. Phys. A* 45 (2012), p. 473001. DOI: [10.1088/1751-8113/45/47/473001](https://doi.org/10.1088/1751-8113/45/47/473001). arXiv: [1205.5040](https://arxiv.org/abs/1205.5040) [hep-th].
- [135] E.M. Lifshitz and L.P. Pitaevski. “Chapter IX - Hydrodynamic Fluctuations.” In: *Statistical Physics*. Oxford: Butterworth-Heinemann, 1980, pp. 360–383. ISBN: 978-0-08-050350-9. DOI: <https://doi.org/10.1016/B978-0-08-050350-9.50014-9>.

- [136] Avdhesh Kumar, Jitesh R. Bhatt, and Ananta P. Mishra. “Fluctuations in Relativistic Causal Hydrodynamics.” In: *Nucl. Phys. A* 925 (2014), pp. 199–217. DOI: [10.1016/j.nuclphysa.2014.02.012](https://doi.org/10.1016/j.nuclphysa.2014.02.012). arXiv: [1304.1873](https://arxiv.org/abs/1304.1873) [hep-ph].
- [137] Koichi Murase and Tetsufumi Hirano. “Relativistic fluctuating hydrodynamics with memory functions and colored noises.” In: (Apr. 2013). arXiv: [1304.3243](https://arxiv.org/abs/1304.3243) [nucl-th].
- [138] Chandrodoy Chattopadhyay, Rajeev S. Bhalerao, and Subrata Pal. “Thermal noise in a boost-invariant matter expansion in relativistic heavy-ion collisions.” In: *Phys. Rev. C* 97.5 (2018), p. 054902. DOI: [10.1103/PhysRevC.97.054902](https://doi.org/10.1103/PhysRevC.97.054902). arXiv: [1711.10759](https://arxiv.org/abs/1711.10759) [nucl-th].
- [139] Chandrodoy Chattopadhyay and Subrata Pal. “Thermal noise in non-boost-invariant dissipative hydrodynamics.” In: *Phys. Rev. C* 98.3 (2018), p. 034911. DOI: [10.1103/PhysRevC.98.034911](https://doi.org/10.1103/PhysRevC.98.034911). arXiv: [1807.03522](https://arxiv.org/abs/1807.03522) [nucl-th].
- [140] Li Yan and Hanna Grönqvist. “Hydrodynamical noise and Gubser flow.” In: *JHEP* 03 (2016), p. 121. DOI: [10.1007/JHEP03\(2016\)121](https://doi.org/10.1007/JHEP03(2016)121). arXiv: [1511.07198](https://arxiv.org/abs/1511.07198) [nucl-th].
- [141] J.I. Kapusta and C. Young. “Causal Baryon Diffusion and Colored Noise.” In: *Phys. Rev. C* 90.4 (2014), p. 044902. DOI: [10.1103/PhysRevC.90.044902](https://doi.org/10.1103/PhysRevC.90.044902). arXiv: [1404.4894](https://arxiv.org/abs/1404.4894) [nucl-th].
- [142] Marlene Nahrgang, Marcus Bluhm, Thomas Schäfer, and Steffen Bass. “Toward the description of fluid dynamical fluctuations in heavy-ion collisions.” In: *Acta Phys. Polon. Supp.* 10 (2017), p. 687. DOI: [10.5506/APhysPolBSupp.10.687](https://doi.org/10.5506/APhysPolBSupp.10.687). arXiv: [1704.03553](https://arxiv.org/abs/1704.03553) [nucl-th].
- [143] Christopher Plumberg and Joseph I. Kapusta. “Hydrodynamic fluctuations near a critical endpoint and Hanbury-Brown–Twiss interferometry.” In: *Phys. Rev. C* 95.4 (2017), p. 044910. DOI: [10.1103/PhysRevC.95.044910](https://doi.org/10.1103/PhysRevC.95.044910). arXiv: [1702.01368](https://arxiv.org/abs/1702.01368) [nucl-th].
- [144] Joseph I. Kapusta and Christopher Plumberg. “Causal Electric Charge Diffusion and Balance Functions in Relativistic Heavy Ion Collisions.” In: *Phys. Rev. C* 97.1 (2018). [Erratum: *Phys.Rev.C* 102, 019901 (2020)], p. 014906. DOI: [10.1103/PhysRevC.97.014906](https://doi.org/10.1103/PhysRevC.97.014906). arXiv: [1710.03329](https://arxiv.org/abs/1710.03329) [nucl-th].

- [145] Aritra De, Christopher Plumberg, and Joseph I. Kapusta. “Calculating Fluctuations and Self-Correlations Numerically for Causal Charge Diffusion in Relativistic Heavy-Ion Collisions.” In: *Phys. Rev. C* 102.2 (2020), p. 024905. DOI: [10.1103/PhysRevC.102.024905](https://doi.org/10.1103/PhysRevC.102.024905). arXiv: [2003.04878](https://arxiv.org/abs/2003.04878) [nucl-th].
- [146] Koichi Murase and Tetsufumi Hirano. “Hydrodynamic fluctuations and dissipation in an integrated dynamical model.” In: *Nucl. Phys. A* 956 (2016). Ed. by Y. Akiba, S. Esumi, K. Fukushima, H. Hamagaki, T. Hatsuda, T. Hirano, and K. Shigaki, pp. 276–279. DOI: [10.1016/j.nuclphysa.2016.01.011](https://doi.org/10.1016/j.nuclphysa.2016.01.011). arXiv: [1601.02260](https://arxiv.org/abs/1601.02260) [nucl-th].
- [147] Azumi Sakai, Koichi Murase, and Tetsufumi Hirano. “Rapidity decorrelation of anisotropic flow caused by hydrodynamic fluctuations.” In: (Mar. 2020). arXiv: [2003.13496](https://arxiv.org/abs/2003.13496) [nucl-th].
- [148] Richard Courant, Kurt Friedrichs, and Hans Lewy. “Über die partiellen Differenzgleichungen der mathematischen Physik.” In: *Mathematische annalen* 100.1 (1928), pp. 32–74.
- [149] R. Maccormack. “The effect of viscosity in hypervelocity impact cratering.” In: *4th Aerodynamic Testing Conference*. DOI: [10.2514/6.1969-354](https://doi.org/10.2514/6.1969-354). eprint: <https://arc.aiaa.org/doi/pdf/10.2514/6.1969-354>.
- [150] Pasi Huovinen and Pter Petreczky. “QCD Equation of State and Hadron Resonance Gas.” In: *Nucl. Phys. A* 837 (2010), pp. 26–53. DOI: [10.1016/j.nuclphysa.2010.02.015](https://doi.org/10.1016/j.nuclphysa.2010.02.015). arXiv: [0912.2541](https://arxiv.org/abs/0912.2541) [hep-ph].
- [151] Paul Romatschke and Ulrike Romatschke. “Viscosity Information from Relativistic Nuclear Collisions: How Perfect is the Fluid Observed at RHIC?” In: *Phys. Rev. Lett.* 99 (2007), p. 172301. DOI: [10.1103/PhysRevLett.99.172301](https://doi.org/10.1103/PhysRevLett.99.172301). arXiv: [0706.1522](https://arxiv.org/abs/0706.1522) [nucl-th].
- [152] Huichao Song and Ulrich W. Heinz. “Multiplicity scaling in ideal and viscous hydrodynamics.” In: *Phys. Rev. C* 78 (2008), p. 024902. DOI: [10.1103/PhysRevC.78.024902](https://doi.org/10.1103/PhysRevC.78.024902). arXiv: [0805.1756](https://arxiv.org/abs/0805.1756) [nucl-th].

- [153] P. Kovtun, Dan T. Son, and Andrei O. Starinets. “Viscosity in strongly interacting quantum field theories from black hole physics.” In: *Phys. Rev. Lett.* 94 (2005), p. 111601. DOI: [10.1103/PhysRevLett.94.111601](https://doi.org/10.1103/PhysRevLett.94.111601). arXiv: [hep-th/0405231](https://arxiv.org/abs/hep-th/0405231).
- [154] Betty Abelev et al. “Centrality determination of Pb-Pb collisions at $\sqrt{s_{NN}} = 2.76$ TeV with ALICE.” In: *Phys. Rev. C* 88.4 (2013), p. 044909. DOI: [10.1103/PhysRevC.88.044909](https://doi.org/10.1103/PhysRevC.88.044909). arXiv: [1301.4361 \[nucl-ex\]](https://arxiv.org/abs/1301.4361).
- [155] A. Adare et al. “Azimuthally anisotropic emission of low-momentum direct photons in Au+Au collisions at $\sqrt{s_{NN}} = 200$ GeV.” In: *Phys. Rev. C* 94.6 (2016), p. 064901. DOI: [10.1103/PhysRevC.94.064901](https://doi.org/10.1103/PhysRevC.94.064901). arXiv: [1509.07758 \[nucl-ex\]](https://arxiv.org/abs/1509.07758).
- [156] Mayank Singh, Chun Shen, Clint Young, Sangyong Jeon, and Charles Gale. “Poster: Effect of Thermal Fluctuations on Electromagnetic and Hadronic Observables.” In: *Quark Matter*. 2017. URL: <https://indico.cern.ch/event/433345/contributions/2373746/>.
- [157] Daniel Lohner. “Measurement of Direct-Photon Elliptic Flow in Pb-Pb Collisions at $\sqrt{s_{NN}} = 2.76$ TeV.” In: *J. Phys. Conf. Ser.* 446 (2013). Ed. by Markus Bleicher et al., p. 012028. DOI: [10.1088/1742-6596/446/1/012028](https://doi.org/10.1088/1742-6596/446/1/012028). arXiv: [1212.3995 \[hep-ex\]](https://arxiv.org/abs/1212.3995).
- [158] Matteo Frigo and Steven G. Johnson. “The Design and Implementation of FFTW3.” In: *Proceedings of the IEEE* 93.2 (2005). Special issue on “Program Generation, Optimization, and Platform Adaptation”, pp. 216–231.
- [159] J. Scott Moreland and Ron A. Soltz. “Hydrodynamic simulations of relativistic heavy-ion collisions with different lattice quantum chromodynamics calculations of the equation of state.” In: *Phys. Rev. C* 93.4 (2016), p. 044913. DOI: [10.1103/PhysRevC.93.044913](https://doi.org/10.1103/PhysRevC.93.044913). arXiv: [1512.02189 \[nucl-th\]](https://arxiv.org/abs/1512.02189).
- [160] G.S. Denicol, T. Kodama, T. Koide, and Ph. Mota. “Effect of bulk viscosity on Elliptic Flow near QCD phase transition.” In: *Phys. Rev. C* 80 (2009), p. 064901. DOI: [10.1103/PhysRevC.80.064901](https://doi.org/10.1103/PhysRevC.80.064901). arXiv: [0903.3595 \[hep-ph\]](https://arxiv.org/abs/0903.3595).
- [161] Betty Abelev et al. “Centrality dependence of π , K, p production in Pb-Pb collisions at $\sqrt{s_{NN}} = 2.76$ TeV.” In: *Phys. Rev. C* 88 (2013), p. 044910. DOI: [10.1103/PhysRevC.88.044910](https://doi.org/10.1103/PhysRevC.88.044910). arXiv: [1303.0737 \[hep-ex\]](https://arxiv.org/abs/1303.0737).

- [162] K. Aamodt et al. “Higher harmonic anisotropic flow measurements of charged particles in Pb-Pb collisions at $\sqrt{s_{NN}}=2.76$ TeV.” In: *Phys. Rev. Lett.* 107 (2011), p. 032301. DOI: [10.1103/PhysRevLett.107.032301](https://doi.org/10.1103/PhysRevLett.107.032301). arXiv: [1105.3865](https://arxiv.org/abs/1105.3865) [nucl-ex].
- [163] Georges Aad et al. “Measurement of event-plane correlations in $\sqrt{s_{NN}} = 2.76$ TeV lead-lead collisions with the ATLAS detector.” In: *Phys. Rev. C* 90.2 (2014), p. 024905. DOI: [10.1103/PhysRevC.90.024905](https://doi.org/10.1103/PhysRevC.90.024905). arXiv: [1403.0489](https://arxiv.org/abs/1403.0489) [hep-ex].
- [164] Shreyasi Acharya et al. “Linear and non-linear flow modes in Pb-Pb collisions at $\sqrt{s_{NN}} = 2.76$ TeV.” In: *Phys. Lett. B* 773 (2017), pp. 68–80. DOI: [10.1016/j.physletb.2017.07.060](https://doi.org/10.1016/j.physletb.2017.07.060). arXiv: [1705.04377](https://arxiv.org/abs/1705.04377) [nucl-ex].
- [165] Shreyasi Acharya et al. “Higher harmonic non-linear flow modes of charged hadrons in Pb-Pb collisions at $\sqrt{s_{NN}} = 5.02$ TeV.” In: *JHEP* 05 (2020), p. 085. DOI: [10.1007/JHEP05\(2020\)085](https://doi.org/10.1007/JHEP05(2020)085). arXiv: [2002.00633](https://arxiv.org/abs/2002.00633) [nucl-ex].
- [166] Björn Schenke, Chun Shen, and Prithwish Tribedy. “Multi-particle and charge-dependent azimuthal correlations in heavy-ion collisions at the Relativistic Heavy-Ion Collider.” In: *Phys. Rev. C* 99.4 (2019), p. 044908. DOI: [10.1103/PhysRevC.99.044908](https://doi.org/10.1103/PhysRevC.99.044908). arXiv: [1901.04378](https://arxiv.org/abs/1901.04378) [nucl-th].
- [167] Bjoern Schenke, Chun Shen, and Prithwish Tribedy. “Running the gamut of high energy nuclear collisions.” In: *Phys. Rev. C* 102.4 (2020), p. 044905. DOI: [10.1103/PhysRevC.102.044905](https://doi.org/10.1103/PhysRevC.102.044905). arXiv: [2005.14682](https://arxiv.org/abs/2005.14682) [nucl-th].
- [168] J. Scott Moreland, Jonah E. Bernhard, and Steffen A. Bass. “Bayesian calibration of a hybrid nuclear collision model using p-Pb and Pb-Pb data at energies available at the CERN Large Hadron Collider.” In: *Phys. Rev. C* 101.2 (2020), p. 024911. DOI: [10.1103/PhysRevC.101.024911](https://doi.org/10.1103/PhysRevC.101.024911). arXiv: [1808.02106](https://arxiv.org/abs/1808.02106) [nucl-th].
- [169] D. Everett et al. “Phenomenological constraints on the transport properties of QCD matter with data-driven model averaging.” In: (Oct. 2020). arXiv: [2010.03928](https://arxiv.org/abs/2010.03928) [hep-ph].
- [170] M. Byres, S. H. Lim, C. McGinn, J. Ouellette, and J. L. Nagle. “The Skinny on Bulk Viscosity and Cavitation in Heavy Ion Collisions.” In: (2019). arXiv: [1910.12930](https://arxiv.org/abs/1910.12930) [nucl-th].

- [171] Frithjof Karsch, Dmitri Kharzeev, and Kirill Tuchin. “Universal properties of bulk viscosity near the QCD phase transition.” In: *Phys. Lett. B* 663 (2008), pp. 217–221. DOI: [10.1016/j.physletb.2008.01.080](https://doi.org/10.1016/j.physletb.2008.01.080). arXiv: [0711.0914](https://arxiv.org/abs/0711.0914) [hep-ph].
- [172] Jacquelyn Noronha-Hostler, Jorge Noronha, and Carsten Greiner. “Transport Coefficients of Hadronic Matter near $T(c)$.” In: *Phys. Rev. Lett.* 103 (2009), p. 172302. DOI: [10.1103/PhysRevLett.103.172302](https://doi.org/10.1103/PhysRevLett.103.172302). arXiv: [0811.1571](https://arxiv.org/abs/0811.1571) [nucl-th].
- [173] Ryan D. Weller and Paul Romatschke. “One fluid to rule them all: viscous hydrodynamic description of event-by-event central p+p, p+Pb and Pb+Pb collisions at $\sqrt{s} = 5.02$ TeV.” In: *Phys. Lett. B* 774 (2017), pp. 351–356. DOI: [10.1016/j.physletb.2017.09.077](https://doi.org/10.1016/j.physletb.2017.09.077). arXiv: [1701.07145](https://arxiv.org/abs/1701.07145) [nucl-th].
- [174] Krishna Rajagopal and Nilesh Tripurani. “Bulk Viscosity and Cavitation in Boost-Invariant Hydrodynamic Expansion.” In: *JHEP* 03 (2010), p. 018. DOI: [10.1007/JHEP03\(2010\)018](https://doi.org/10.1007/JHEP03(2010)018). arXiv: [0908.1785](https://arxiv.org/abs/0908.1785) [hep-ph].
- [175] Jitesh R. Bhatt, Hiranmaya Mishra, and V. Sreekanth. “Cavitation and thermal photon production in relativistic heavy ion collisions.” In: (2010). arXiv: [1005.2756](https://arxiv.org/abs/1005.2756) [hep-ph].
- [176] M. Schulc and B. Tomasik. “Rapidity correlations of protons from a fragmented fireball.” In: *Eur. Phys. J. A* 45 (2010), pp. 91–97. DOI: [10.1140/epja/i2010-10984-0](https://doi.org/10.1140/epja/i2010-10984-0). arXiv: [1001.4678](https://arxiv.org/abs/1001.4678) [nucl-th].
- [177] Jitesh R. Bhatt, Hiranmaya Mishra, and V. Sreekanth. “Thermal photons in QGP and non-ideal effects.” In: *JHEP* 11 (2010), p. 106. DOI: [10.1007/JHEP11\(2010\)106](https://doi.org/10.1007/JHEP11(2010)106). arXiv: [1011.1969](https://arxiv.org/abs/1011.1969) [hep-ph].
- [178] Aleksandra Klimek, Louis Leblond, and Aninda Sinha. “Cavitation in holographic sQGP.” In: *Phys. Lett. B* 701 (2011), pp. 144–150. DOI: [10.1016/j.physletb.2011.05.045](https://doi.org/10.1016/j.physletb.2011.05.045). arXiv: [1103.3987](https://arxiv.org/abs/1103.3987) [hep-th].
- [179] David Mateos and Diego Trancanelli. “The anisotropic $N=4$ super Yang-Mills plasma and its instabilities.” In: *Phys. Rev. Lett.* 107 (2011), p. 101601. DOI: [10.1103/PhysRevLett.107.101601](https://doi.org/10.1103/PhysRevLett.107.101601). arXiv: [1105.3472](https://arxiv.org/abs/1105.3472) [hep-th].

- [180] David Mateos and Diego Trancanelli. “Thermodynamics and Instabilities of a Strongly Coupled Anisotropic Plasma.” In: *JHEP* 07 (2011), p. 054. DOI: [10.1007/JHEP07\(2011\)054](https://doi.org/10.1007/JHEP07(2011)054). arXiv: [1106.1637](https://arxiv.org/abs/1106.1637) [hep-th].
- [181] Alex Buchel, Xian O. Camanho, and Jose D. Edelstein. “Cavitation effects on the confinement/deconfinement transition.” In: *Phys. Lett.* B734 (2014), pp. 131–133. DOI: [10.1016/j.physletb.2014.05.047](https://doi.org/10.1016/j.physletb.2014.05.047). arXiv: [1303.6300](https://arxiv.org/abs/1303.6300) [hep-ph].
- [182] Mathis Habich and Paul Romatschke. “Onset of cavitation in the quark-gluon plasma.” In: *JHEP* 12 (2014), p. 054. DOI: [10.1007/JHEP12\(2014\)054](https://doi.org/10.1007/JHEP12(2014)054). arXiv: [1405.1978](https://arxiv.org/abs/1405.1978) [hep-ph].
- [183] Gabriel S. Denicol, Charles Gale, and Sangyong Jeon. “The domain of validity of fluid dynamics and the onset of cavitation in ultrarelativistic heavy ion collisions.” In: *PoS CPOD2014* (2015), p. 033. DOI: [10.22323/1.217.0033](https://doi.org/10.22323/1.217.0033). arXiv: [1503.00531](https://arxiv.org/abs/1503.00531) [nucl-th].
- [184] S. M. Sanches, D. A. Fogaça, F. S. Navarra, and H. Marrochio. “Cavitation in a quark gluon plasma with finite chemical potential and several transport coefficients.” In: *Phys. Rev.* C92.2 (2015), p. 025204. DOI: [10.1103/PhysRevC.92.025204](https://doi.org/10.1103/PhysRevC.92.025204). arXiv: [1505.06335](https://arxiv.org/abs/1505.06335) [hep-ph].
- [185] Akihiko Monnai, Swagato Mukherjee, and Yi Yin. “Phenomenological Consequences of Enhanced Bulk Viscosity Near the QCD Critical Point.” In: *Phys. Rev.* C95.3 (2017), p. 034902. DOI: [10.1103/PhysRevC.95.034902](https://doi.org/10.1103/PhysRevC.95.034902). arXiv: [1606.00771](https://arxiv.org/abs/1606.00771) [nucl-th].
- [186] Jes Madsen. “Cavitation from bulk viscosity in neutron stars and strange stars.” In: (2009). arXiv: [0909.3724](https://arxiv.org/abs/0909.3724) [astro-ph.SR].
- [187] Jean-Sebastien Gagnon and Julien Lesgourgues. “Dark goo: Bulk viscosity as an alternative to dark energy.” In: *JCAP* 1109 (2011), p. 026. DOI: [10.1088/1475-7516/2011/09/026](https://doi.org/10.1088/1475-7516/2011/09/026). arXiv: [1107.1503](https://arxiv.org/abs/1107.1503) [astro-ph.CO].
- [188] Y. Tachibana et al. “Hydrodynamic response to jets with a source based on causal diffusion.” In: *28th International Conference on Ultrarelativistic Nucleus-Nucleus Collisions*. Feb. 2020. arXiv: [2002.12250](https://arxiv.org/abs/2002.12250) [nucl-th].

- [189] Shanshan Cao and Xin-Nian Wang. “Jet quenching and medium response in high-energy heavy-ion collisions: a review.” In: (Feb. 2020). arXiv: [2002.04028 \[hep-ph\]](#).
- [190] Torbjörn Sjöstrand, Stefan Ask, Jesper R. Christiansen, Richard Corke, Nishita Desai, Philip Ilten, Stephen Mrenna, Stefan Prestel, Christine O. Rasmussen, and Peter Z. Skands. “An introduction to PYTHIA 8.2.” In: *Comput. Phys. Commun.* 191 (2015), pp. 159–177. DOI: [10.1016/j.cpc.2015.01.024](#). arXiv: [1410.3012 \[hep-ph\]](#).
- [191] Guy D. Moore and Derek Teaney. “How much do heavy quarks thermalize in a heavy ion collision?” In: *Phys. Rev. C* 71 (2005), p. 064904. DOI: [10.1103/PhysRevC.71.064904](#). arXiv: [hep-ph/0412346](#).
- [192] Hendrik van Hees, Vincenzo Greco, and Ralf Rapp. “Heavy-quark probes of the quark-gluon plasma at RHIC.” In: *Phys. Rev. C* 73 (2006), p. 034913. DOI: [10.1103/PhysRevC.73.034913](#). arXiv: [nucl-th/0508055](#).
- [193] Shanshan Cao and Steffen A. Bass. “Thermalization of charm quarks in infinite and finite QGP matter.” In: *Phys. Rev. C* 84 (2011), p. 064902. DOI: [10.1103/PhysRevC.84.064902](#). arXiv: [1108.5101 \[nucl-th\]](#).
- [194] Santosh K. Das, Francesco Scardina, Salvatore Plumari, and Vincenzo Greco. “Heavy-flavor in-medium momentum evolution: Langevin versus Boltzmann approach.” In: *Phys. Rev. C* 90 (4 2014), p. 044901. DOI: [10.1103/PhysRevC.90.044901](#).
- [195] Shuang Li, Chaowen Wang, Renzhuo Wan, and Jinfeng Liao. “Probing the transport properties of quark-gluon plasma via heavy-flavor Boltzmann and Langevin dynamics.” In: *Phys. Rev. C* 99 (5 2019), p. 054909. DOI: [10.1103/PhysRevC.99.054909](#).
- [196] Munshi Golam Mustafa, Dipali Pal, and Dinesh Kumar Srivastava. “Propagation of charm quarks in equilibrating quark - gluon plasma.” In: *Phys. Rev. C* 57 (1998). [Erratum: *Phys.Rev.C* 57, 3499–3499 (1998)], pp. 889–898. DOI: [10.1103/PhysRevC.57.3499](#). arXiv: [nucl-th/9706001](#).

- [197] Manu Kurian, Mayank Singh, Vinod Chandra, Sangyong Jeon, and Charles Gale. “A study of charm quark dynamics in quark-gluon plasma with 3+1 D viscous hydrodynamics.” In: *Phys. Rev. C* 102.4 (2020), p. 044907. DOI: [10.1103/PhysRevC.102.044907](https://doi.org/10.1103/PhysRevC.102.044907). arXiv: [2007.07705](https://arxiv.org/abs/2007.07705) [hep-ph].
- [198] Hendrik van Hees and Ralf Rapp. “Thermalization of heavy quarks in the quark-gluon plasma.” In: *Phys. Rev. C* 71 (2005), p. 034907. DOI: [10.1103/PhysRevC.71.034907](https://doi.org/10.1103/PhysRevC.71.034907). arXiv: [nucl-th/0412015](https://arxiv.org/abs/nuc1-th/0412015).
- [199] Debasish Banerjee, Saumen Datta, Rajiv Gavai, and Pushan Majumdar. “Heavy Quark Momentum Diffusion Coefficient from Lattice QCD.” In: *Phys. Rev. D* 85 (2012), p. 014510. DOI: [10.1103/PhysRevD.85.014510](https://doi.org/10.1103/PhysRevD.85.014510). arXiv: [1109.5738](https://arxiv.org/abs/1109.5738) [hep-lat].
- [200] Francesco Scardina, Santosh K. Das, Vincenzo Minissale, Salvatore Plumari, and Vincenzo Greco. “Estimating the charm quark diffusion coefficient and thermalization time from D meson spectra at energies available at the BNL Relativistic Heavy Ion Collider and the CERN Large Hadron Collider.” In: *Phys. Rev. C* 96.4 (2017), p. 044905. DOI: [10.1103/PhysRevC.96.044905](https://doi.org/10.1103/PhysRevC.96.044905). arXiv: [1707.05452](https://arxiv.org/abs/1707.05452) [nucl-th].